

**TEST OF DECAY RATE PARAMETER VARIATION  
DUE TO ANTINEUTRINO INTERACTIONS**

by

**Shih-Chieh Liu**

**A Dissertation**

*Submitted to the Faculty of Purdue University*

*In Partial Fulfillment of the Requirements for the degree of*

**Doctor of Philosophy**



Department of Physics & Astronomy

West Lafayette, Indiana

December 2018



**THE PURDUE UNIVERSITY GRADUATE SCHOOL**  
**STATEMENT OF DISSERTATION APPROVAL**

Dr. David S. Koltick, Chair

Department of Physics and Astronomy, Purdue University

Dr. Robert S. Bean

Department of Nuclear Engineering, Purdue University

Dr. Martin M. Kruczenski

Department of Physics and Astronomy, Purdue University

Dr. Wei Xie

Department of Physics and Astronomy, Purdue University

**Approved by:**

Dr. John P. Finley

Head of Department of Physics and Astronomy, Purdue University

This dissertation is dedicated to my wife who encouraged me to pursue my dreams  
and finish my dissertation.

## ACKNOWLEDGMENTS

I would like to express my special appreciation and thanks to my advisor Professor David S Koltick. I thank David wholeheartedly, not only for his tremendous academic support but also for giving me so many excellent opportunities.

I am grateful to all of those with whom I have had the pleasure to work during this and other related projects. Each of the members of my Committee has provided me professional guidance in this research. I would also especially like to thank Dr. Haoyu Wang, Dr. Jonathan Nistor, and Dr. Jordan Heim for theoretical and technical support in this project.

In addition, I would like to thank the Physics Department for fully financial support during my graduate studies at Purdue. Also, this work would not have been possible without the financial support from Dr. Tom Ward, TechSource Inc.

Finally, I would like to thank my families, whose love and guidance are with me in whatever I pursue. They are the ultimate role models. Most importantly, I am grateful to my loving and supportive wife, Joling, and my two wonderful children, Alex, and Aiden, who provide unending inspiration.

## TABLE OF CONTENTS

	Page
LIST OF TABLES . . . . .	viii
LIST OF FIGURES . . . . .	x
ABSTRACT . . . . .	xiii
1 Overview . . . . .	1
2 Neutrinos . . . . .	7
2.1 Standard Properties of Neutrinos . . . . .	7
2.2 Neutrino Oscillations . . . . .	9
2.3 Solar Neutrino Flux . . . . .	10
2.4 Parity Invariance Violation . . . . .	11
2.5 Reactor Anomaly, and LSND Experiment . . . . .	12
3 Reported Results, and Phenomena . . . . .	15
3.1 Historical: Variation of Radioactive Decay Rate Parameters . . . . .	15
3.2 Cross Section Sensitivity to Variations of Decay Rate Parameter . . . . .	23
4 Experimental Configuration at High Flux Isotope Reactor . . . . .	31
4.1 High Flux Isotope Reactor (HFIR) . . . . .	31
4.2 Reactor-Generated Antineutrinos . . . . .	32
4.3 Flux of Antineutrinos at High Flux Isotope Reactor . . . . .	34
4.4 Experiment Layout at HFIR . . . . .	35
4.5 High Purity Germanium Detector (HPGe) . . . . .	39
4.6 Shielding Performance, and Background Stability of the HPGe Detector . . . . .	41
5 Energy Calibration of the $^{54}\text{Mn}$ , and the Background Spectra at HFIR . . . . .	47
5.1 Energy Calibration of Background Spectra . . . . .	48
5.2 Energy Calibration of $^{54}\text{Mn}$ $\gamma$ -Spectra . . . . .	52
6 Corrections to the $^{54}\text{Mn}$ Source, and Background Spectra . . . . .	65
6.1 Electronic Dead Time Correction . . . . .	66
6.2 Background Spectrum Correction . . . . .	69
6.2.1 Technical Process for Dead Time Correction . . . . .	70
6.2.2 Background Spectrum Energy Rescaling . . . . .	71
6.2.3 Background Spectrum Amplitude Rescaling . . . . .	73
6.2.4 Background Spectrum Subtraction . . . . .	75
6.3 Pile-up Correction by De-convolution Algorithm . . . . .	77
6.4 Region of Interest (ROI) of $^{54}\text{Mn}$ Spectrum . . . . .	81

	Page
6.5 Region of Interest(ROI) Measurement Limit Estimation . . . . .	84
7 Data Analysis of Corrected $^{54}\text{Mn}$ spectral . . . . .	87
7.1 Single Parameter Fitting to the Region of Interest . . . . .	87
7.2 Side Band Ambient Temperature Corrections . . . . .	91
7.3 Results After All Corrections (ROI) . . . . .	99
8 Conclusion . . . . .	105
VITA . . . . .	114

## LIST OF TABLES

Table	Page
2.1 Three known types of neutrinos, electron neutrino, muon neutrino, and tau neutrino. . . . .	8
2.2 The full neutrino flux production from each fusion reaction in the Sun. . .	11
2.3 Individual predicted cross section per fission per fissile isotope $k$ , $\sigma_k$ in units of $10^{-43} \text{ cm}^2/\text{fission}$ , and the error is represented as a percentage of the cross section[52] . . . . .	13
3.1 Summary of the $^{32}\text{Si}$ , and $^{36}\text{Cl}$ results. . . . .	16
3.2 Summary of the $^{152}\text{Eu}$ , $^{154}\text{Eu}$ , and $^{155}\text{Eu}$ results. . . . .	17
3.3 Summary of the $^3\text{H}$ results. . . . .	19
3.4 Summary of the $^{54}\text{Mn}$ results. . . . .	20
3.5 Summary of the $^{137}\text{Cs}$ results. . . . .	21
3.6 Summary of the $^{226}\text{Ra}$ results. . . . .	22
3.7 Summary of experiments that conclude time-dependence of radioactive decay rate parameters. . . . .	29
3.8 Summary of experiments that conclude <b>Null</b> evidence for radioactive decay rate parameter variation. . . . .	30
4.1 Antineutrino characteristics from $^{235}\text{U}$ , $^{238}\text{U}$ , $^{239}\text{Pu}$ , and $^{241}\text{Pu}$ [59]. . . . .	35
4.2 The yearly cycling of the humidity relative to the experiments starting date	39
4.3 The average background rate, and associated error during the reactor-on or reactor-off periods at HFIR. . . . .	46
5.1 Spectral lines used in the calibration of the background energy calibration.	48
5.2 Calibration coefficients of background spectra with reactor-off for linear, and nonlinear calibration. $\chi^2$ per degree of freedom significantly improves with the nonlinear calibration. . . . .	50
5.3 Accepted energy, and uncertainty of the calibration lines for the $^{54}\text{Mn}$ spectrum . . . . .	55



Table	Page
5.4 The yearly cycling of the humidity, temperature for the HPGe source detector, and linear term $b$ values relative to the experiments starting date.	62
6.1 Proprieties of the full $^{54}\text{Mn}$ spectrum. . . . .	69
6.2 Error analysis, and estimation per day in Region of Interest (ROI) of $^{54}\text{Mn}$ daily spectrum. . . . .	84
7.1 Comparison of in-phase, and out-of-phase ROI oscillation. . . . .	89
7.2 The $\chi^2$ per degree of freedom from fitting equal width energy regions in Figure 7.4. . . . .	94
7.3 Average residuals, and uncertainty of each reactor-on, and reactor-off period.	101
7.4 Residuals, and uncertainty of each reactor-on, and reactor-off period for segment analysis. . . . .	102
7.5 Size of effect, and uncertainty from a single constant term. . . . .	103
7.6 68% confidence upper limit on antineutrino interaction on $^{54}\text{Mn}$ . . . . .	103
8.1 Summary of measurements at HFIR of $^{54}\text{Mn}$ decay rate variations measurement. . . . .	105
8.2 Coefficients from four type of curve fitting with previous experiments. . .	107

## LIST OF FIGURES

Figure	Page
1.1 The logarithm cross section sensitivity of time-dependent variation results, no evidence results, and this HFIR result as a function of the logarithm mean lifetime. . . . .	5
2.1 Helicity of a neutrino, and antineutrino. . . . .	12
3.1 Using the estimates in this section shown is the cross section limit divided by the measuring time in units of mean lifetime. . . . .	26
4.1 High Flux Isotope Reactor at Oak Ridge National Lab . . . . .	31
4.2 The power as a function of time of High Flux Isotope Reactor at Oak Ridge National Lab during this experiment. . . . .	32
4.3 Mass distribution of $^{235}\text{U}$ fission fragments. . . . .	33
4.4 (Left) Nitrogen gas atmosphere to reduce reactor produced $^{40}\text{Ar}$ in the housing, and eliminate humidity to the detector. (Right) HPGe detector spectrometer system in operation at HFIR . . . . .	36
4.5 Experimental Layout at HFIR. . . . .	37
4.6 Ambient pressure, temperature, and humidity as a function of time at HFIR.	38
4.7 Daily average humidity fitted with in phase periodic function (Eq. 4.8), fixed at 1 year, as a function of time. . . . .	39
4.8 Configuration of High Purity Germanium Detector (HPGe). . . . .	40
4.9 (Left) The HPGe detector measured the background spectrum at HFIR. (Right) The HPGe source detector measured the source spectrum. . . . .	41
4.10 HFIR background spectra with, and without shielding in the reactor on or off status. . . . .	42
4.11 Full background spectrum rate as a function of time which includes reactor-on, and reactor-off cycles with the $^{54}\text{Mn}$ source removed. . . . .	44
5.1 Background spectrum with 19 identified lines at HFIR . . . . .	49
5.2 Background spectral line residuals for reactor-off, and reactor-on status. . .	51
5.3 Logarithm scale of the $^{54}\text{Mn}$ $\gamma$ -spectrum at HFIR. . . . .	53

Figure	Page
5.4 Differential Backscattered, and Compton Edges peaks from $^{54}\text{Mn}$ daily spectra at HFIR. . . . .	56
5.5 Independent $^{54}\text{Mn}$ spectrum measured in the Physics Building at Purdue University used to study systematic shift. . . . .	57
5.6 Differential Backscattered, and Compton Edges peaks from an independent measurement of the $^{54}\text{Mn}$ daily spectrum made in the Physics Building at Purdue University to study the energy peak shift. . . . .	58
5.7 Nonlinear energy calibration parameters, $a_r$ , $b_r$ , and $c_r$ , determined for each of the daily $^{54}\text{Mn}$ spectra. . . . .	60
5.8 Daily averages for the humidity, temperature of the HPGe source detector, and the linear term $b_r$ . . . . .	61
5.9 Energy of the $^{54}\text{Mn}$ primary photopeak as a function of time. The average energy of $^{54}\text{Mn}$ is $834.849 \pm 0.001$ KeV which shows stability after the nonlinear calibration. . . . .	63
6.1 Correction procedure flow for obtaining the true $^{54}\text{Mn}$ ROI count rate. . .	66
6.2 Illustration of electronic dead time from the DSPEC-50 spectrometer. . . .	67
6.3 DSPEC-50's Minimum, and Maximum Protection Times[64]. . . . .	68
6.4 Logarithm scale of the $^{54}\text{Mn}$ $\gamma$ -spectrum before background spectrum subtraction, and the background spectrum . . . . .	76
6.5 Logarithm scale of the $^{54}\text{Mn}$ $\gamma$ -ray spectrum after background subtraction. .	78
6.6 De-convolution algorithm used to determine pileup events to be removed from the $^{54}\text{Mn}$ spectrum. . . . .	79
6.7 Calculated pileup spectrum (blue) with the starting spectrum (red) demonstrating the fit achieved by the de-convolution algorithm. . . . .	80
6.8 The Region of Interest, from 820 to 900 KeV, is selected from the corrected daily $^{54}\text{Mn}$ spectrum. . . . .	82
7.1 Daily decay rate from the integration between 820 to 900 KeV of the $^{54}\text{Mn}$ spectra. . . . .	87
7.2 Daily residual fitted with a revised exponential decay function (Eq 7.3) which includes a single periodic function. . . . .	88
7.3 The oscillation term found by subtraction of the exponential term from the data (Eq. 7.3), and its fit shown in Red data points . . . . .	90
7.4 Residuals of equal width energy regions from the corrected $^{54}\text{Mn}$ spectrum. .	92

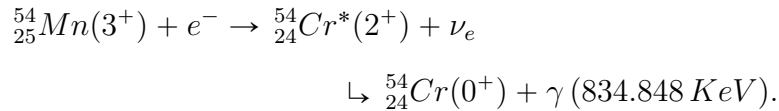
Figure	Page
7.5 Daily Decay rate of Region 740 KeV to 820 KeV of $^{54}\text{Mn}$ spectra . . . . .	95
7.6 (Upper) Daily residual of the side band energy region in the $^{54}\text{Mn}$ spectra. (Lower) Daily residual of the side band energy region of $^{54}\text{Mn}$ spectra after the exponential function correction. A significant fluctuations appear in Period, 1, 5, and 6. . . . .	96
7.7 (Upper)Daily residuals of the side band energy region as a function daily average Temperature.(Lower) Daily residual in Period 5, 6, and 7 dur- ing periods with stable temperature, of the side band energy region as a function of daily relative humidity. . . . .	97
7.8 Daily $\delta c_r$ , and corrected residual of Region 740 KeV to 820 KeV of $^{54}\text{Mn}$ spectra, and daily average Temperature. . . . .	99
7.9 Corrected ROI Residuals as a function of time. . . . .	100
8.1 The logarithm cross section sensitivity of time-dependent variation results, no evidence results, and this HFIR result as a function of the logarithm mean lifetime. . . . .	108

## ABSTRACT

Shih-Chieh Liu Ph.D., Purdue University, December 2018. Test of Decay Rate Parameter Variation due to Antineutrino Interactions. Major Professor: David S Koltick.

High precision measurements of a weak interaction decay were conducted to search for possible variation of the decay rate parameter caused by an antineutrino flux. The experiment searched for variation of the  $^{54}_{25}\text{Mn}$  electron capture decay rate parameter to a level of precision of 1 part in  $\sim 10^5$  by comparing the difference between the decay rate in the presence of an antineutrino flux  $\sim 3 \times 10^{12} \bar{\nu} \text{ cm}^{-2} \text{ sec}^{-1}$  and no flux measurements. The experiment is located 6.5 meters from the reactor core of the High Flux Isotope Reactor(HFIR) in Oak Ridge National Laboratory. The results show no effect during the antineutrino exposure. A measurement to this level of precision requires a detailed understanding of both systematic and statistical errors. Otherwise, systematic errors in the measurement may mimic fundamental interactions.

The  $\gamma$  spectrum has been collected from the electron capture decay of  $^{54}\text{Mn}$ ,



What differs in this experiment compared to previous experiments are, (1) a strong, uniform, highly controlled, and repeatable (Power  $\delta P/P \sim 10^{-3}$ ) source of antineutrino flux, using a reactor, nearly 50 times higher than the solar neutrino flux on the Earth, (2) the variation of the antineutrino flux from HFIR is 600 times higher than the variation in the solar neutrino flux on the Earth, (3) the extensive use of neutron and  $\gamma$ -ray shielding around the detectors, (4) a controlled environment for

the detector including a fixed temperature, a nitrogen atmosphere, and stable power supplies, (5) the use of precision High Purity Germanium (HPGe) detectors and finally, (6) accurate time stamping of all experimental runs. By using accurate detector energy calibrations, electronic dead time corrections, background corrections, and pile-up corrections, the measured variation in the decay rate parameter is found to be  $\delta\lambda/\lambda = (0.034 \pm 1.38) \times 10^{-5}$ . This measurement in the presence of the HFIR flux is equivalent to a cross section of  $\sigma = (0.097 \pm 1.24) \times 10^{-25} \text{ cm}^2$ . These results are consistent with no measurable decay rate parameter variation due to an antineutrino flux, yielding a 68% confidence level upper limit sensitivity in  $\delta\lambda/\lambda \leq 1.43 \times 10^{-5}$  or  $\sigma \leq 1.34 \times 10^{-25} \text{ cm}^2$  in cross section. The cross-section upper limit obtained in this null or no observable effect experiment is  $\sim 10^4$  times more sensitive than past experiments reporting positive results in  $^{54}\text{Mn}$ .

## 1. Overview

Unexplained periodic variation of the decay rate parameter measurement for weak interaction decays such as  $\beta^\pm$ -decay, and electron capture [1–18] as well as strong interaction  $\alpha$ -decay[5, 12] have been reported. Because the variation of the decay rate parameter has been presented by a number of groups, located at various locations, using various types of detectors, different isotopes, and over extended periods of time, some researchers have interpreted the source of these variations as not from ambient environmental factors such as temperature, pressure, and humidity but via an unexplained fundamental interaction. Some results show a correlation between an annual periodicity of the decay rate parameter variation, and the variable distance of the Earth from the Sun. The annual variation of the Earth-Sun distance causes a  $\sim 7\%$  variation of the total neutrino flux on the Earth. This flux variation as the source of the decay rate parameter variation is motivated by the large neutrino flux,  $6.5 \times 10^{10} \nu cm^{-2} sec^{-1}$ , on the Earth dominated by solar fusion. Also, some researchers suggest that decay rate parameters are affected by solar activity such as solar flares[19–22].

However, these conclusions are controversial. This research is focused on the possibilities that the reported variations are an extension of weak interactions. Conventional weak interaction neutrino-nucleon cross sections are 20 orders of magnitude smaller than the reported strong interaction level cross-sections being observed in

these experiments, if caused by neutrinos. The conventional neutrino interaction cross-section per nucleon ( $\nu + n \rightarrow p^+ + e^-$ ) is [23]

$$\begin{aligned}\sigma_{weak} &\sim \frac{4G_F^2 E_\nu^2 (\hbar c)^2}{\pi} \\ &\sim 9 \times 10^{-44} \text{ cm}^2 \left( \frac{E_\nu}{1 \text{ MeV}} \right)^2\end{aligned}\tag{1.1}$$

where  $G_F$  is the Fermi constant, and  $E_\nu$  is the neutrino energy. Because antineutrinos interact with protons ( $\bar{\nu} + p^+ \rightarrow n + e^+$ ), there is no significant difference between neutrino, and antineutrino interaction cross-section on target nuclei. That is neutron, and proton number are similar  $\sim A/2$ . If a typical neutrino or antineutrino energy is considered to be  $\sim 1 \text{ MeV}$ , Eq.1.1 leads to a nucleon cross section of

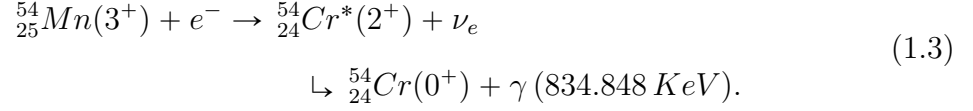
$$\sigma_{weak} \sim N^\beta \times 9 \times 10^{-44} \text{ cm}^2\tag{1.2}$$

where  $N \sim A/2$  is the number of neutrons or protons in the nucleus. The antineutrino cross section is proportional to  $N^\beta$ .  $\beta = 2$  if the antineutrino scattering is coherent from the nucleus, and  $\beta = 1$  if the scattering is incoherent. The largest possible conventional cross section occurs if the scattering is coherent.

The goal of this experiment is to maximize the sensitivity to the decay parameter variation caused by a possible extension to the weak interactions. The disadvantage of solar neutrinos as a test source is the low flux variation ( $\sim 10^9 \nu \text{ cm}^{-2} \text{ sec}^{-1}$ ) which demands long measurement time. Antineutrinos can be generated from a nuclear reactor having a stable antineutrino flux ( $\sim 3 \times 10^{12} \bar{\nu} \text{ cm}^{-2} \text{ sec}^{-1}$ ), and high flux variations due to the reactor off cycles ( $\sim 0 \nu \text{ cm}^{-2} \text{ sec}^{-1}$ ) [24]. For this reason, the experiment was performed at the High Flux Isotope Reactor (HFIR) at Oak Ridge National Laboratory (ORNL). The HFIR provides reactor-on, and reactor-off cycles



of similar duration. Specifically, the experiment recorded the  $\gamma$  spectra from  $^{54}_{25}\text{Mn}$  electron capture decay



Even though the maximum possible weak cross section, coherent, for  $^{54}\text{Mn}(Z = 25$  with  $\beta = 2)$  is expected to be at the level of

$$\sigma_{weak} \sim 6 \times 10^{-41} \text{ cm}^2, \quad (1.4)$$

the cross-section sensitivity to decay parameter variation obtainable at HFIR is  $10^3$  to  $10^4$  more sensitive than the reported positive results having strong interaction level cross-section. The use of antineutrinos in no way invalids comparison between this, and previous experimental effects based on neutrinos.  $^{54}\text{Mn}$  was specially selected because the basic interaction involves a proton ( $p^+ + e^- \rightarrow n + \nu$ ) matching the inverse  $\beta^-$ -decay reaction on neutrons caused by neutrinos.

The  $^{54}\text{Mn}$  spectra were collected using a High Purity Germanium Detector (HPGe) Spectrometer system with background neutron, and  $\gamma$  radiation shielding, and well-monitored environmental factors to obtain the results. The shielding was effective in suppressing the backgrounds by a factors  $1.8 \times 10^{-4}$  (reactor-on), and  $6.7 \times 10^{-4}$  (reactor-off). The  $^{54}\text{Mn}$  spectra required corrections including dead time corrections, non-linear energy calibrations, background spectra subtraction, as well as pile-up effects correction using a de-convolution algorithm. While the entire spectrum was used in order to calculate the corrections, a Region of Interest (ROI) around the photopeak of  $^{54}\text{Mn}$  was carefully selected for optimal stability over time. No effect has been observed in the decay parameter at the level of

$$\frac{\delta\lambda}{\lambda} = (0.034 \pm 1.38) \times 10^{-5} \quad (1.5)$$

in the presence of an antineutrino flux  $F_{\bar{\nu}} \sim 3 \times 10^{12} \bar{\nu} cm^{-2} sec^{-1}$ , this measurement yields an equivalent cross-section

$$\begin{aligned} \sigma &= \frac{\delta\lambda/\lambda}{\tau \times \Delta F_{\bar{\nu}}} \\ &= (0.097 \pm 1.24) \times 10^{-25} cm^2 \end{aligned} \tag{1.6}$$

where  $\tau$  is the mean lifetime of  $^{54}\text{Mn}$ . This results will be discussed in detail later in Chapters 7, and 8. The results are consistent with no measurable decay rate parameter variation due to an antineutrino flux yielding 68% confidence level upper limit of sensitivity  $\delta\lambda/\lambda \leq 1.43 \times 10^{-5}$  or  $\sigma \leq 1.34 \times 10^{-25} cm^2$  in cross section. The significance of this limit needs a comparison to previous results as interpreted being due to solar neutrinos. Figure 1.1 summarizes the comparison showing this experiment to be previous experiments. In this comparison Figure, curve (a) is the temporal cross-section fit  $\sigma = A\tau^P$  to those experiments reporting decay rate parameter variations shown as triangles. Curve (b) compares experiments by cross-section only. This experiment is more sensitive than all previous experiments reporting positive decay rate parameter variations. Curve (c) connects this experiment, and a solar neutrino experiment using  $^{40}\text{K}$ [19]. The connection between these two experiments maps out an exclusion zone in the temporal cross-section space excluding decay rate parameter variations at a level  $10^4$  times more sensitive than any previously reported positive results. Curve (d) displays the temporal cross exclusion zone  $\sigma \sim \sigma_{limit}\tau^{-1}$  if extrapolated using only this experiment.

If the decay rate parameter variations had been detected in this experiment, the exact form of the interaction would need theoretical underpinning as at present no theoretical motivation exists. Such positive results would represent entirely new physics.

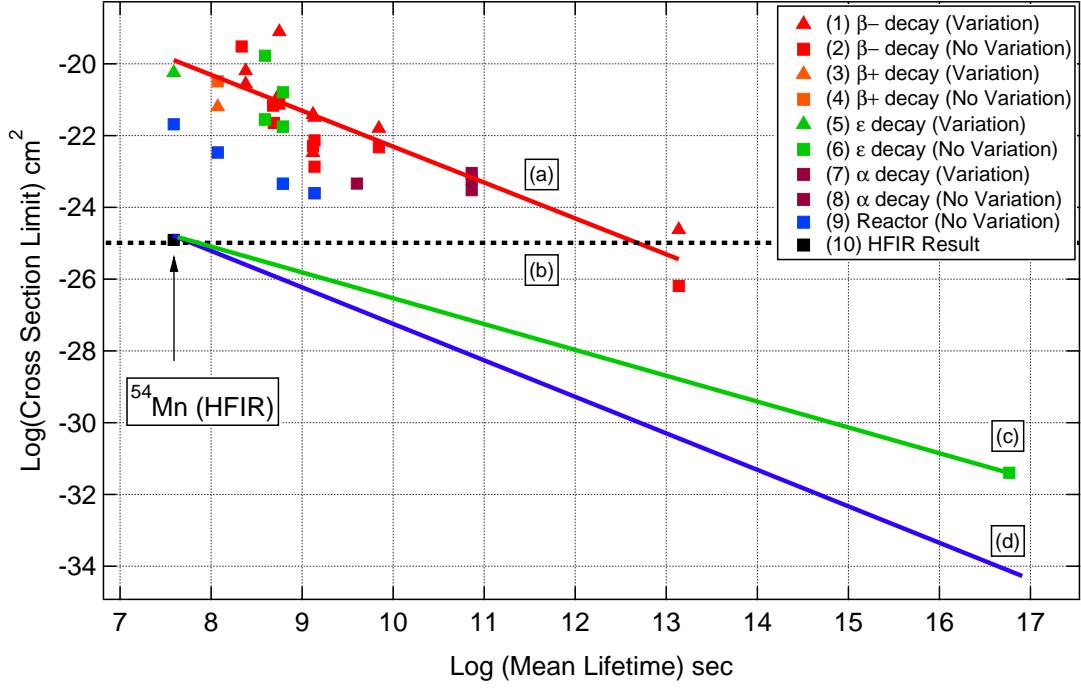


Figure 1.1. The logarithm cross section sensitivity of time-dependent variation results, no evidence results, and this HFIR result as a function of the logarithm mean lifetime. The data are based on Table 3.7, and 3.8. The data includes (1)  $\beta^-$  decay with variation results[1, 3, 6, 16, 18, 25–28], (2)  $\beta^-$  decay with no effect results[8, 12, 19, 29–32], (3)  $\beta^+$  decay with variation results[7], (4)  $\beta^+$  decay with no effect results[33], (5) Electron Capture decay with variation results[21], (6) Electron Capture decay with no effect results[8, 12, 19], (7)  $\alpha$  decay with with variation results[5], (8)  $\alpha$  decay with no effect results[12, 30, 34], and (9) reactor antineutrino as a test source with no effect results[35]. (10) The HFIR  $^{54}\text{Mn}$  experiment result. See the text for explanation of the curves (a), (b), (c), and (d).



## 2. Neutrinos

In this chapter, the fundamentals of neutrinos relevant to this research are introduced.

### 2.1 Standard Properties of Neutrinos

From the moment of the neutrino hypothesis to the present, properties of the neutrino continue to be surprising, and strange. The original hypothesis of the neutrino was required because of the observed continuous energy distribution of the  $\beta$ -decay electrons. If beta decay were a two-body reaction, the  $\beta^-$  should be emitted at a fixed energy. However, the emitted particles had a continuous energy distribution. To solve this missing energy problem, Pauli assumed a second particle emitted in the  $\beta$ -decay process in 1930. It was assumed, and later measured to be highly penetrating radiation. This "second particle" is now known as the *Neutrino*, named by Fermi. The beta decay reactions are now understood to be

$$\begin{aligned}
 n &\rightarrow p^+ + e^- + \bar{\nu}_e && \text{Negative beta decay } (\beta^-) \\
 p^+ &\rightarrow n + e^+ + \nu_e && \text{Positive beta decay } (\beta^+) \\
 p^+ + e^- &\rightarrow n + \nu_e && \text{Electron capture } (\epsilon)
 \end{aligned} \tag{2.1}$$

Some of the historical standard properties of neutrinos are as follows:

1. The neutrino is charge neutral, and its rest mass is near zero.
2. The neutrino was measured to have spin-1/2 making it a fermion.
3. The conservation of lepton number gives a rule to understand neutrino, and antineutrino interactions. Take  $\beta^-$ -decay as an example, the assignment of a lepton number of 1 to the electron, and -1 to the electron antineutrino explains the apparent lepton number conservation in weak interaction reactions.

4. Two different kind of neutrinos participate in  $\beta$  decay, *neutrinos*, and *antineutrinos*.
5. The neutrino is always observed to be a parity eigenstate. The helicity of an antineutrino is only observed parallel to its momentum while for the neutrino, it is anti-parallel to its momentum.
6. The neutrino discussed in  $\beta$ -decay is known as the "*Electron Neutrino*". In the Standard Model of particle physics, there are three kinds of charged leptons: electron, muon, and tau. The table below lists the known types of neutrinos.

Table 2.1.  
Three known types of neutrinos, electron neutrino, muon neutrino,  
and tau neutrino.

Neutrino	$\nu_e$	$\nu_\mu$	$\nu_\tau$
Generation	First	Second	Third
Charged Partner	electron( $e$ )	muon( $\mu$ )	tau( $\tau$ )
First Exp. Discovery	1956	1962	2000

7. The first discovery of a particle fitting the expected characteristics of the neutrino was announced by Cowan, and Reines[36, 37]. In 1962, experiments at Brookhaven National Laboratory, and CERN, the European Laboratory for Physics, made surprising discoveries: neutrinos produced in association with muons do not behave the same as those produced in association with electrons[38]. Likewise, the tau neutrino was introduced after the tau had been discovered at Stanford Linear Acceleration Center. The DONUT experiment at Fermi Lab was built to specifically detect the tau neutrino, and reported the first detection in 2000[39].

In this study, the word *neutrino*, and *antineutrino* indicate the *electron neutrino*, and *electron antineutrino*.

## 2.2 Neutrino Oscillations

In contrast, initial studies of neutrinos assumed each neutrino type, electron, muon, and tau had separately conserved lepton numbers, and each was massless. Now neutrino lepton flavor oscillation experiments have changed these concepts. The concept of neutrino oscillations have a long history when as early as 1958, Bruno Pontecorvo mused over the possibility of neutrino-antineutrino oscillation in analogy with neutral Kaon mixing[40].

If neutrinos have mass, the particle mass eigenstate, and lepton flavor eigenstate of the particles may not be the same, allowing mixing. In this case, the neutrino can oscillate from one flavor to another while traveling through space. The observation of oscillations implies the neutrino flavor states are not mass eigenstate but are the superposition of such states. The neutrino flavour states  $|\nu_\alpha\rangle$  ( $\alpha = e, \mu, \tau$ ) are related to the mass state  $|\nu_j\rangle$ , ( $j = 1, 2, 3$ ) linearly,

$$\begin{bmatrix} \nu_e \\ \nu_\mu \\ \nu_\tau \end{bmatrix} = \begin{bmatrix} U_{e1} & U_{e2} & U_{e3} \\ U_{\mu1} & U_{\mu2} & U_{\mu3} \\ U_{\tau1} & U_{\tau2} & U_{\tau3} \end{bmatrix} * \begin{bmatrix} \nu_1 \\ \nu_2 \\ \nu_3 \end{bmatrix} \quad (2.2)$$

where  $U_{\alpha j}$  is the  $3 \times 3$  Pontecorvo–Maki–Nakagawa–Sakata(PMNS) unitary matrix. The probability of the three neutrino case is difficult to express explicitly. However, the two flavor mixing fully illustrates the effect. In this case, the unitary matrix  $U$  is given by

$$U = \begin{bmatrix} U_{\alpha1} & U_{\alpha2} \\ U_{\beta1} & U_{\beta2} \end{bmatrix} = \begin{bmatrix} \cos \theta & \sin \theta \\ -\sin \theta & \cos \theta \end{bmatrix} \quad (2.3)$$

where  $\theta$  is the mixing angle. By imputing this U matrix, and the  $\Delta m_{12}^2$  mass difference between the states, the probability of 2 neutrino mixing is

$$P(\nu_\alpha \rightarrow \nu_\beta) = \sin^2(2\theta) \sin^2\left(\frac{\Delta m^2 L}{4E}\right) \quad (2.4)$$

The mixing acts as a quantum mechanical phase factor in the wave function. If the neutrinos were zero mass particles,  $\Delta m_{12}^2$  is zero, and then  $P(\nu_\alpha \rightarrow \nu_{\alpha'}) = 0$ . Neutrino oscillations have been observed by a number of experiments showing lepton number is not conserved[41–46]. The observations of the neutrino oscillations conclude that at least one neutrino flavor has non-zero mass. Again, these surprising results are in sharp counterpoint to the neutrinos historical properties.

There are four different experimental confirmations of neutrino oscillations, (1) solar neutrino oscillations first observed by Davis[41], (2) atmospheric neutrino oscillations first observed by Fukuda[42], (3) reactor neutrino oscillations first observed by An, and Anh[43, 44], and (4) neutrino beam oscillations[45, 46] have been observed. Notably, the existence of neutrino oscillations has resolved the long-standing solar neutrino problem. That is the missing solar neutrino flux predicted by the solar model. Davis’s observations of solar neutrino oscillation open the door to the possibility of oscillation to other unpredicted weakly interacting particles within in the solar flux on the Earth as well in other neutrino sources.

### 2.3 Solar Neutrino Flux

Amazingly, during the course of a human lifetime approximately,  $10^{20}$  solar neutrinos will pass through each  $cm^2$  of our bodies. The source of solar neutrino production is the fusion reaction of hydrogen into helium. The nuclear fusion in the Sun occurs in the core at a temperature of about 15M Kelvin. 99% of the power is generated within 24% of the Sun’s radius, and by 30% of the radius, fusion has stopped entirely. The Sun’s energy is produced by nuclear fusion in the core region through a series of steps called the p–p (proton–proton) chain which produces  $> 91\%$  of the solar neutrinos. Electron neutrinos are produced as steps in the fusion reaction from hydrogen to helium. For example, two protons fuse to produce  $^2D$  by jointly forming an unbound excited state of  $^2He^*$  which then  $\beta$  decays to  $^2D$ . This key step in the



Table 2.2.

The full neutrino flux production from each fusion reaction in the Sun. The average total solar flux on the Earth is  $6.5 \times 10^{10} \nu \text{ cm}^{-2} \text{ sec}^{-1}$ . Most of the solar neutrinos are from the pp(pronton–proton) chain(>91%). The  ${}^7\text{Be}$ , pep(proton-electron-proton), and  ${}^8\text{Be}$  chain are 7%, 0.2%, and 0.008%. The hep (helium3-electron-proton) chain can be neglected due to its relative small flux [47].

Reaction	Label	Flux ( $\text{cm}^{-2} \text{ sec}^{-1}$ )
$p + p \rightarrow {}^2\text{H} + e^+ + \nu_e$	<i>pp</i>	$5.95 \times 10^{10}$
$p + e^- + p \rightarrow {}^2\text{H} + \nu_e$	<i>pep</i>	$1.14 \times 10^8$
${}^3\text{He} + p \rightarrow {}^4\text{He} + e^+ + \nu_e$	<i>hep</i>	$9.30 \times 10^3$
${}^7\text{Be} + e^- \rightarrow {}^7\text{Li} + \nu_e$	${}^7\text{Be}$	$4.77 \times 10^9$
${}^8\text{Be} \rightarrow {}^8\text{Be} + e^+ + \nu_e$	${}^8\text{Be}$	$5.05 \times 10^6$

proton to helium fusion process has never been observed experimentally. On average, two  $\beta^+$  decays take place in the p–p chain to yield  ${}^4\text{He}$ . The total energy released by these reactions in turning 4 hydrogen atoms into 1 helium atom is 26.7 MeV.



The total solar neutrino flux on the Earth assuming no oscillations is  $6.5 \times 10^{10} \text{ cm}^{-2} \text{ sec}^{-1}$  [47]. Davis results indicates  $\sim 1/2$  these solar neutrino have oscillated before reaching the Earth[41].

## 2.4 Parity Invariance Violation

The mechanism, which generates neutrino oscillations is still under investigation, and the Standard Model may be changed due to this new physics reality. Because neutrinos always participate in weak interactions from a single parity eigenstate, the opposite non-participating state is called "sterile."

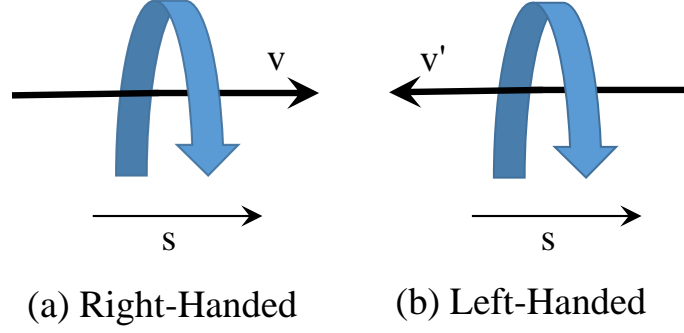


Figure 2.1. Helicity of Neutrino, and Antineutrino. (a) Right-handed (Antineutrino) the spin, and velocity are parallel. (b) Left-handed (Neutrino) represents the spin, and velocity are anti-parallel. The handedness (helicity) of the neutrino is consistent with the -1, and antineutrino is consistent with the +1.

Parity invariance had been considered a universal law of nature until the 1950s. Yang, and Lee proposed parity in  $\beta$ -decay (Weak Interactions) to be violated in 1956[48]. Wu's successful experiment soon confirmed their hypothesis by measuring  $^{60}\text{Co}$   $\beta$ -decay[49]. In the past, neutrinos were assumed to be produced in  $\pm 1$  helicity equally. However, Goldhaber's experiment proved all neutrinos to be left-handed, and all antineutrinos are right-handed[50]. The mirror images of neutrinos, and antineutrinos do not exist. Right-handed neutrinos, and left-handed antineutrinos have never been observed. If they were to exist, they would not interact via the weak interaction. Those hypothetical neutrinos are often referred to as "*sterile*" neutrinos. If sterile neutrinos do exist, they could explain not only the existence of neutrino masses but also the smallness of their mass scale[51]. Sterile neutrinos are also a candidate for dark matter.

## 2.5 Reactor Anomaly, and LSND Experiment

The three-neutrino framework has been extremely successful in explaining neutrino oscillation results in solar, atmospheric, accelerator, and reactor neutrino os-

cillation experiments. Their experiments are explained using only two oscillation frequencies. These frequencies correspond to two mass difference terms, each on the order of  $10^{-3}$  to  $10^{-5}$  eV. However, two experiments present results confronting this seemingly unified picture, the reactor anomaly experiment[52], and Liquid Scintillator Neutrino (LSND) experiment[41].

The reactor anomaly refers to the deficiency of observed antineutrinos from experiments performed at reactors compared with the theoretical predictions. The anomaly being that only about 94% of the expected antineutrinos are actually measured compared to the flux expected by theoretical models[52]. It is unknown whether this is due to new physics such as a fourth generation neutrino, a sterile neutrino, experimental error in the measurements, or errors in the theoretical flux calculations. Recently, some researchers have attempted to explain reactor anomalies as being caused by sterile neutrino production[52].

Table 2.3.

Individual predicted cross section per fission per fissile isotope  $k$ ,  $\sigma_k$  in units of  $10^{-43} \text{ cm}^2/\text{fission}$ , and the error is represented as a percentage of the cross section[52]. When the new cross-section estimates for the reactor fuel mix are compared to the experimentally measured flux, a significant 6% deficit is observed, possibility accounted for by production of new particles.

Predicted	Old(Bugey)[53]	New [52]
$\sigma(^{235}\text{U})$	$6.39 \pm 1.9\%$	$6.61 \pm 2.11\%$
$\sigma(^{239}\text{Pu})$	$4.19 \pm 2.4\%$	$4.34 \pm 2.45\%$
$\sigma(^{238}\text{U})$	$9.21 \pm 10\%$	$10.10 \pm 8.15\%$
$\sigma(^{241}\text{Pu})$	$5.73 \pm 2.1\%$	$5.97 \pm 2.15\%$
$\sigma(\text{Reactor Mix})$	$5.824 \pm 2.7\%$	$6.102 \pm 2.7\%$
$\sigma(\text{Exp})[53]$	$5.752 \pm 1.4\%$	
$\sigma(\text{Exp})/\sigma(\text{Reactor Mix})$	$0.987 \pm 1.4\% \pm 2.7\%$	$0.943 \pm 1.4\% \pm 2.7\%$

This view has also support from the LSND experiment started in the 1990s[41]. The LSND experiment reported an anomalous event excess in the  $\bar{\nu}_\mu \rightarrow \bar{\nu}_e$  appearance channel, which can be interpreted as an oscillation with  $\Delta m^2 \sim 1 \text{ eV}$ [54, 55]. This  $\Delta m^2$  mass scale is clearly incompatible with the three-neutrino framework. The LSND anomaly, if true, indicates the existence at least an additional fourth neutrino family with  $\Delta m^2 \sim 1 \text{ eV}$ . The antineutrino deficiency can be explained by a sterile neutrino with large  $\Delta m^2$ [52]. Therefore, resolving the question of the reactor anomaly's existence is an appropriate first step in determining whether sterile neutrinos exist.

### **What Are Neutrinos?**

In summary, with the above considerations, it is clear the "Story" of what is a neutrino is far from complete. The search for new, and novel neutrino interactions is worth pursuing.

### 3. Reported Results, and Phenomena

In this chapter, the experiments relevant to decay parameter variations are summarized. In addition, the observable effects of a decay parameter variation on the measuring sensitivity, and effective cross section are presented.

#### 3.1 Historical: Variation of Radioactive Decay Rate Parameters

Oscillation variations of the radioactive decay rate parameters have been investigated for several decades. A number of groups such as Alburger, Falkenberg, Veprev, and Jenkins *et. al.* observed time-dependent decay rate parameter variations[1–6, 21, 25]. Because the variation of the decay rate parameters has been reported (1) at various locations (2) with various type of detectors, (3) using different isotopes, and (4) over extend periods of time, these researchers believe the variations are not due to the ambient environmental factors such as temperature, pressure, and humidity. Some results show a correlation between an annual periodicity of the decay rate parameter variation, and the variable distance of the Earth from the Sun. These results motivate some researchers to conclude the solar neutrino flux variations cause the decay rate parameter variations[4–6, 21].

However, the correlation of the radioactive decay rate parameter variation, and solar neutrino flux has been challenged by Kossert, Semkow, Meijer, Bruhn, Schrader, and Bellotti *et. al.*[8, 9, 29–32, 35]. These "null evidence" experimental references attribute the decay rate parameter variation to ambient environmental factors or instrumental error, instead of the solar neutrino flux variation.

In this section, a summary of some key results will be discussed. The results are sorted by isotopes, and published date. A key comment, and a short summary table are presented at the beginning of each discussion. "Positive" represents those observation reporting time-dependent decay rate parameters, whereas "Negative" are those showing no variation results. The size of the observed effect or the experimental sensitivity( $\delta\lambda/\lambda$ ) in the case of null results are also displayed in the short summary table in each discussion. Where as Table 3.7, and Table 3.8 display the results of the full literature review, and cross-section sensitivities for each reported isotope.

- $^{32}\text{Si}$ , and  $^{36}\text{Cl}$

Table 3.1.  
Summary of the  $^{32}\text{Si}$ , and  $^{36}\text{Cl}$  results.

Source	Reference	Sensitivity (Size of Effect)	Variation
$^{32}\text{Si}/^{36}\text{Cl}$	Alburger <i>et. al.</i>	$5 \times 10^{-3}$	Positive
$^{36}\text{Cl}$	Kossert <i>et. al.</i>	$4 \times 10^{-4}$	Negative
$^{32}\text{Si}$	Semkow <i>et. al.</i>	$1 \times 10^{-3}$	Negative

- **Alburger** *et. al.* reported the first observation of decay rate parameter variations in 1986. Alburger worked on the half life measurement of  $^{32}\text{Si}$  with a gas proportional detector over the period 1982 through 1986 at Brookhaven National Lab(BNL)[1]. They unexpectedly observed small periodic annual deviations of the data points from an exponential decay. The authors reported that temperature, and humidity "*can not fully account*" for observed ratio  $^{32}\text{Si}/^{36}\text{Cl}$  decay rate variation during their measurement, as shown in Table 3.1. However, they do not have complete environment records, to backup these claims.
- **Kossert** *et. al.* reported no decay rate parameter variations of  $^{36}\text{Cl}$  measured using a custom-built triple-to-double coincident ratio detector (TDCR)

at Physikalisch-Technische Bundesanstalt (PTB)[31]. TDCR is an optical chamber with three photomultiplier tubes surrounding a liquid scintillation detector. The sample is placed in the center. A triple coincidence detector is much less sensitivity to ambient environmental factors. Kossert measured much smaller variation of  $^{36}\text{Cl}$  as shown in Table 3.1 than observed by Alburger but Kossert attributes the small variation to instrumental effects, instead of variations of the decay rate parameter. This conclusion is much more reliable than Alburger's because Alburger used a single gas proportional detector which is sensitive to environmental variations.

- **Semkow** has written a review concerning decay rate parameter variations of  $^{32}\text{Si}$  from Alburger's results[30]. Semkow explained the variations of  $^{32}\text{Si}$  by the change of temperature causing the air density in the space between the source, and the gas proportional detector to change reducing, and increasing the count rate. The higher temperature in the summer causes lower air density in the space between the source, and the detector, and resulting in less absorption of the lower energy  $\beta$  particles in the air. Thus, the gas proportional detector collects more  $\beta$  particles at a higher temperature, generating a higher counting rate. The resulting limit is given in Table 3.1.

- $^{152}\text{Eu}$ ,  $^{154}\text{Eu}$ , and  $^{155}\text{Eu}$

Table 3.2.  
Summary of the  $^{152}\text{Eu}$ ,  $^{154}\text{Eu}$ , and  $^{155}\text{Eu}$  results.

Source	Reference	Sensitivity	Variation
$^{152}\text{Eu}$ , $^{154}\text{Eu}$ , and $^{155}\text{Eu}$	Siegert <i>et. al.</i>	$5 \times 10^{-4}$	Negative
$^{152}\text{Eu}$	Meijer <i>et. al.</i>	$1.4 \times 10^{-4}$	Negative

- **Siegert *et. al.*** studied the multi  $\beta$ -decay modes of Eu isotopes. Siegert used the strong interaction  $\alpha$ -particle  $^{226}\text{Ra}$  decay as a reference to de-

termine the half life of the weak interaction  $\beta$  decays of  $^{152}\text{Eu}$ ,  $^{154}\text{Eu}$ , and  $^{155}\text{Eu}$ , measured using two different kinds of detector systems; an ion chamber, and a solid state detector(Ge, Li) at Physikalisch-Technische Bundesanstalt (PTB)[12].  $^{152}\text{Eu}$  decays to  $^{152}\text{Gd}$  by electron capture with 72.1% branching ratio, and to  $^{152}\text{Sm}$  by  $\beta^-$ -decay with branching ratio 27.9%. Siegert reported that the oscillations of  $^{226}\text{Ra}$  have a maximum positive deviation in February, and minimum deviation in August. Siegert observed oscillations in  $^{226}\text{Ra}$  as well as in the other isotopes but explains the effect as follows:

*"A discharge effect on the charge collecting capacitor, the cables, and the insulator to the ionization chamber electrode caused by background radioactivity such as radon, and daughter products which are known to show seasonal concentration changes.*

Siegert concludes the oscillations are proportional to the ionization current. If the oscillations were due to solar neutrinos interacting with isotopes via the weak interactions, the  $^{226}\text{Ra}$  strong interaction decay oscillations should not depend on the ionization current. With these considerations, Siegert's observation are considered to be upper limits, as shown in Table 3.2.

- **Meijer** *et. al.* used reactor antineutrinos as a source. Meijer reported null evidence for the decay rate variation of  $^{152}\text{Eu}$  using reactor antineutrinos[35], as shown in Table 3.2. If the solar neutrino variations cause the decay rate parameter variation, Meijer should have observed a stronger effect compared to Siegert due to the factor of 10 higher antineutrino flux variation from the reactor cycling. No effect was observed.

- **$^3\text{H}$**

- **Falkenberg** is the first one to put forward the hypothesis that the variations of the  $\beta$ -decay rate parameters are due to the solar neutrino flux variations. Falkenberg measured the radioactive  $\beta$ -decay rate parameter of



Table 3.3.  
Summary of the  $^3\text{H}$  results.

Source	Reference	Sensitivity (Size of Effect)	Variation
$^3\text{H}$	Falkenberg	$3.7 \times 10^{-3}$	Positive
$^3\text{H}$	Bruhn	$2 \times 10^{-3}$	Negative
$^3\text{H}$	Veprev <i>et. al.</i>	$2 \times 10^{-1}$	Positive

tritium by a photodiode detector from 1980 to 1982[2], as shown in Table 3.3. To determine the significance of the data's periodic deviation, the residuals were first fit to a single periodic function. Falkenberg calculated the residuals as the differences between an aperiodic exponential form, and the data. Then, he included a cosine function in the fit with a period of 365 days in order to account for the variation away from the aperiodic function. Falkenberg concluded:

*"There is a positive correlation between the periodically changing solar neutrino flux, and the  $\beta$ -decay of tritium"*

- **Bruhn** re-analyzed Falkenberg's data, and criticized Falkenberg for not making corrections for any background effects in his tritium decay rate measurements [29]. In addition, Bruhn concludes Falkenberg's results are not sufficient for deducing a correlation between the tritium decay rate, and the orbital motion of the Earth because neither the period nor amplitude of the deviation coincides with the orbital motion of the Earth. Bruhn concludes:

*"By taking the deviation of the measurement data with respect to the optimal solution instead of the true solution (in the fits) E.D. Falkenberg cannot separate any (hypothetical) additional background effects in his data from the true solution."*

Bruhn’s analysis of Falkenberg’s data can be used to estimate a limit on the decay parameter variations in  $^3\text{H}$ . Both results are included in this review, as shown in Table 3.3.

- **Veprev** *et. al.* measured the high-energy region of the tritium beta decay spectrum using a liquid scintillation detector system viewed by three photomultipliers[25]. Veprev reported decay rate parameter oscillations which coincide with the solar neutrino flux variation distance from the Earth to the Sun, as shown in Table 3.3. Veprev concludes that the periodicity of the tritium decay rate parameter variations is due to the interactions of the tritium nuclei with solar neutrinos.

- $^{54}\text{Mn}$

Table 3.4.  
Summary of the  $^{54}\text{Mn}$  results.

Source	Reference	Sensitivity (Size of Effect)	Variation
$^{54}\text{Mn}$	Jenkins <i>et. al.</i>	$1 \times 10^{-3}$	Positive
$^{54}\text{Mn}$	Meijer <i>et. al.</i>	$4 \times 10^{-4}$	Negative

- **Jenkins** *et. al.* was the first to conclude there is a decay rate parameter variation due to the variable distance of the Earth from the Sun. The results are shown in Table 3.4. In addition, Jenkins *et. al.* reported the detection of a significant decrease in the decay rate parameter of  $^{54}\text{Mn}$  during a strong solar flare at the end of 2006. Jenkins measured the count rate of  $^{54}\text{Mn}$ , and compared it with the Solar X-ray data. The deviation is clearly visible on 12/12/06, through 12/17/06, which was coincident with a severe solar storm. Jenkins attributed the annual oscillations observed in

the data to the variations in solar neutrino flux due to the annual variation in the distance between the Sun, and the Earth[6, 21].

- **Meijer** *et. al.* used reactor antineutrinos as a source. Meijer reported null evidence of the  $^{54}\text{Mn}$  electron capture decay rate parameter to vary due to an antineutrino flux with improved sensitivity relative to Jenkins'[6, 21, 35], as shown in Table 3.4. The experiments were conducted comparing the  $\gamma$ -ray count rate during reactor on, and off periods at an antineutrino flux of  $\sim 5 \times 10^{10} \bar{\nu} \text{ cm}^{-2} \text{ sec}^{-1}$ . The results showed no variations of the  $^{54}\text{Mn}$  decay rate parameter. This challenges Jenkin's conclusions because the solar neutrino causes only  $\sim 7\%$  ( $4.6 \times 10^9 \nu \text{ cm}^{-2} \text{ sec}^{-1}$ ) variations on the Earth. Hence, Meijer should have observed an effect more than 10 times larger than Jenkin's, if Jenkin's hypothesis, were correct.

- $^{137}\text{Cs}$

Table 3.5.  
Summary of the  $^{137}\text{Cs}$  results.

Source	Reference	Sensitivity	Variation
$^{137}\text{Cs}$	Schrader	$4.6 \times 10^{-4}$	Negative
$^{137}\text{Cs}$	Bellotti <i>et. al.</i>	$8.5 \times 10^{-5}$	Negative

- **Schrader** *et. al.* observed variations in the decay rate measurements of  $^{137}\text{Cs}$  using an ionization chamber at Physikalisch-Technische Bundesanstalt (PTB)[8]. Schrader concludes the small yearly variations are from the measuring electronics, instead of decay rate parameter variations. The results are shown in Table 3.5.
- **Bellotti** *et. al.* measured the decay rate of  $^{137}\text{Cs}$  radioactive source using a NaI scintillation detector, and a Ge semiconductor detector[19]. The results are shown in Table 3.5. No significant yearly deviation from the

expectations was measured. In addition, the data exhibited no decay rate parameter variations in the presence of the two solar flares of the year 2011, and 2012.

- $^{226}\text{Ra}$

Table 3.6.  
Summary of the  $^{226}\text{Ra}$  results.

Source	Reference	Sensitivity (Size of Effect)	Variation
$^{226}\text{Ra}$	Siegert <i>et. al.</i>	$1 \times 10^{-3}$	Negative
$^{226}\text{Ra}$	Jenkins <i>et. al.</i>	$2 \times 10^{-3}$	Positive

- **Siegert** *et. al.* used  $^{226}\text{Ra}$ , having a strong interaction  $\alpha$ -particle decay, to study decay parameter variations. Siegert measured  $^{226}\text{Ra}$  decay rate with an ionization chamber at the PTB[12]. Siegert reported that the oscillations of  $^{226}\text{Ra}$  have a maximum positive deviation in February, and minimum deviation in August. He accounted for these oscillations as due to seasonal environmental variations. This conclusion meets the expectation of a null result if extensions to weak interactions were the source of parameter variations. The results are shown in Table 3.6.
- **Jenkins** re-analyzed Siegert’s  $^{226}\text{Ra}$  decay rate data, and showed the observed variations have a correlation to the inverse squared distance between the Earth, and the Sun[5]. The results are shown in Table 3.6.

## In Summary

The literature does not report a consistent picture of decay rate parameter variations caused by neutrinos or antineutrinos. Moreover, most references do not discuss the cross section sensitivity in their reports. For this reason, the results are not di-

rectly comparable without such a framework. All authors except one report only the size of the effect relative to the decay rate. If the reported results claim interactions between the decay rate parameter variation, and a neutrino flux, they should show a meaningful cross-section sensitivity to account for the interaction. Therefore, this work places previous results into a unified framework expressed as an interaction cross section due to the neutrino flux. Furthermore, cross-section sensitivity provides an opportunity to examine further how to proceed in studies of possible decay rate parameter variations of radioactive isotopes.

### 3.2 Cross Section Sensitivity to Variations of Decay Rate Parameter

While the exact cause of decay rate parameter variation is not known, if the assumption is correct, the effect is proportional to the antineutrino flux from the reactor core or the neutrino flux in the case of the solar source. With this assumption, experimental cross section sensitivity represents the amount of exposure from the source.

To accomplish this the cross section needs to be framed in terms of the decay rate parameter variation. The standard decay rate is given by

$$\begin{aligned} R(t) &= N_0 \lambda \exp(-\lambda t) \\ &= \frac{N_0}{\tau} \exp\left(\frac{-t}{\tau}\right) \end{aligned} \tag{3.1}$$

where  $N_0$  is the constant of integration which gives the original number of nuclei present when exposure begins.  $\lambda$  is the decay constant, and  $\tau$  is the mean lifetime which also equals to  $1/\lambda$ . The variation of the radioactive decay rate parameter at time  $t$  results in

$$R'(t) = \frac{N_0}{\tau + \delta\tau} \exp\left(\frac{-t}{\tau + \delta\tau}\right) \tag{3.2}$$

where  $\delta\tau$  is the measured variation. The experimental cross-section expresses the reaction rate to the exposure from the source, and can be written as

$$\sigma = \frac{\text{Reaction Events per Unit Time per Nucleus}}{\text{Incident Flux of Neutrinos or Antineutrinos per Unit Area per Unit Time}} \quad (3.3)$$

This is equivalent to

$$\sigma = \left| \frac{\delta R(t)}{N(t)} \right| \times \frac{1}{\Delta F_{\nu \text{ or } \bar{\nu}}} \quad (3.4)$$

where  $\delta R(t)$  is the reaction events per unit time.  $N(t)$  is the number of nuclei at time  $t$ .  $\Delta F_{\nu \text{ or } \bar{\nu}}$  is the variation of the neutrino or antineutrino flux. Eq.3.4 can be written

$$\sigma = \frac{|\delta R(t)/R(t)|}{\tau \times \Delta F_{\nu \text{ or } \bar{\nu}}} \quad (3.5)$$

by definition  $N(t) = R(t)/\lambda$ .

To convert  $|\delta R(t)/N(t)|$  into the measuring limit  $\delta\lambda/\lambda$ , the reaction rate per unit time per nucleus is given by

$$\begin{aligned} \frac{\delta R(t)}{N(t)} &= \frac{R(t) - R'(t)}{N(t)} \\ &= \frac{N_0 [\tau^{-1} \exp(-t/\tau) - (\tau + \delta\tau)^{-1} \exp(-t/(\tau + \delta\tau))]}{N_0 \exp(-t/\tau)} \\ &= \frac{1}{\tau} - \frac{1}{(\tau + \delta\tau)} \exp\left(\frac{-t}{\tau + \delta\tau}\right) \exp\left(\frac{t}{\tau}\right) \end{aligned} \quad (3.6)$$

Because  $\delta\tau \ll \tau$ ,

$$\begin{aligned} \exp\left(\frac{-t}{\tau + \delta\tau}\right) &\sim \exp\left(-\frac{t}{\tau} \left(1 - \frac{\delta\tau}{\tau}\right)\right) \\ &= \exp\left(-\frac{t}{\tau}\right) \exp\left(\frac{\delta\tau t}{\tau^2}\right), \end{aligned} \quad (3.7)$$

and

$$\frac{1}{(\tau + \delta\tau)} \sim \frac{1}{\tau} \left(1 + \frac{\delta\tau}{\tau}\right)^{-1}. \quad (3.8)$$

Using these approximations in Eq 3.6 results in

$$\frac{\delta R(t)}{N(t)} = \frac{1}{\tau} \left[ 1 - \left( 1 + \frac{\delta\tau}{\tau} \right)^{-1} \exp \left( \frac{\delta\tau}{\tau} \frac{t}{\tau} \right) \right] \quad (3.9)$$

Even with significant decay ( $t \sim \tau$ ), the exponential term in Eq. 3.9 is still small because  $\delta\tau/\tau$  ranges from  $10^{-2}$  to  $10^{-5}$ . From this consideration

$$\begin{aligned} \frac{\delta R(t)}{N(t)} &= \frac{1}{\tau} \left[ 1 - \left( 1 - \frac{\delta\tau}{\tau} \right) \left( 1 + \frac{\delta\tau}{\tau} \frac{t}{\tau} \right) \right] \\ &= \frac{1}{\tau} \left[ \frac{\delta\tau}{\tau} \left( 1 - \frac{t}{\tau} + \frac{\delta\tau}{\tau} \frac{t}{\tau} \right) \right] \end{aligned} \quad (3.10)$$

In this experiment as well as all those reviewed the measurement time  $t \ll \tau$ , therefore,

$$\frac{\delta R(t)}{N(t)} \sim \frac{1}{\tau} \frac{\delta\tau}{\tau} \quad (3.11)$$

All the reviewed results as well as this experiment can be framed as a cross section for comparison by dividing by the neutrino flux variation. Inputting the variation decay rate, Eq. 3.11 into Eq. 3.4 yields,

$$\begin{aligned} \sigma &= \left| \frac{1}{\tau} \frac{\delta\tau}{\tau} \right| \times \frac{1}{\Delta F_{\nu or \bar{\nu}}} \\ &= \frac{|\delta\tau/\tau|}{\tau \times \Delta F_{\nu or \bar{\nu}}} \end{aligned} \quad (3.12)$$

where  $\Delta F_{\nu or \bar{\nu}}$  is the variation of the neutrino or antineutrino flux. With  $\delta\tau = -\delta\lambda/\lambda^2$ , and  $\tau = 1/\lambda$ , Eq. 3.12 can be written

$$\sigma = \frac{|\delta\lambda/\lambda|}{\tau \times \Delta F_{\nu or \bar{\nu}}} \quad (3.13)$$

From this it is observed there are two routes to improve the cross section sensitivity. The first method is to measure the isotope decay parameter as precisely as possible. The second is to get as close as possible to the reactor core to increase the antineutrino flux. This experiment has taken both approaches.

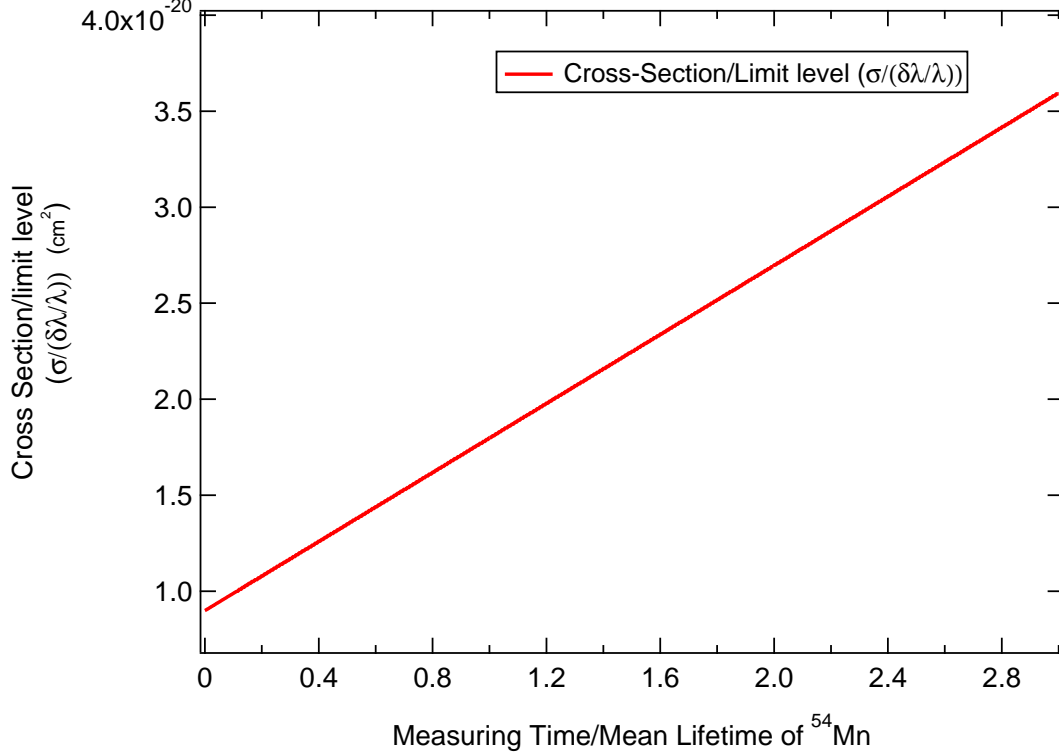


Figure 3.1. Using the estimates in this section shown is the cross section limit divided by the measuring time in units of mean lifetime. The cross section sensitivity is reduced as a function of experimental observation time due to the decay of the isotope.

### The HFIR Experiment Sensitivity Estimation

As will be shown, the flux ( $F_{\bar{\nu}}$ ) in HFIR is  $\sim 2.86 \times 10^{12} \bar{\nu} \text{ cm}^{-2} \text{ sec}^{-1}$  at 6.53 meters from the core. The reactor power is highly stable so the reactor-on antineutrino flux from HFIR is constant as a function of time in this experiment. A single reactor-on period is nearly 26 days compared to the  $^{54}\text{Mn}$  mean lifetime, 450.41 days, satisfying  $t \ll \tau$ , and as shown in Figure 3.1 no correction to Eq.3.13 is required. The cross section limit is effectively set by averaging individual reactor-on, and reactor-off measurements.



Eq.3.13 shows that the cross-section sensitivity is related to the measuring error, is inversely related to the mean isotope lifetime, and the antineutrino flux. By using the  $^{54}\text{Mn}$  mean lifetime,  $\tau = 450.41$  days, setting the measuring error to  $\delta\lambda/\lambda \sim 10^{-5}$ , and using the neutrino flux at 6.53 meters away from the core, the expected cross-section sensitivity for this experiment is found using Eq. 3.13 to be

$$\sigma \sim 9.0 \times 10^{-26} \text{ cm}^2. \quad (3.14)$$

### Solar Neutrino Variation Estimation

Most of the references have used the Sun as a neutrino source. The total solar neutrino flux on the Earth is  $6.5 \times 10^{10} \nu \text{ cm}^{-2} \text{ s}^{-1}$ . The variation of the neutrino flux depends on the distance between the Earth, and the Sun. The Earth has an elliptical orbit with perihelion at 147.1M km, and aphelion at 152.1M km. The semi-major axis is 149.6M km. The solar neutrino flux is proportional to the inverse squared distance, thus

$$\frac{1/r_{\text{perihelion}}^2 - 1/r_{\text{aphelion}}^2}{1/r_{\text{semi-major}}^2} = \frac{(1/147.1)^2 - (1/152.1)^2}{(1/149.6)^2} \quad (3.15)$$

$$\sim 7\%$$

The result of the above equation yields a solar neutrino flux variation of nearly 7%. The amplitude of the variation of the solar neutrino flux is then  $\sim 4.6 \times 10^9 \nu \text{ cm}^{-2} \text{ sec}^{-1}$  on the Earth.

### Branching Ratio Cross-section Sensitivity

If an isotope has more than one decay mode, the branching fraction of the decay mode must be taken into consideration. The effective decay rate can be modified by multiplying with the branching fraction  $f$

$$\sigma_{effective} = \left| \frac{\delta R(t)}{N(t)} \right| \times \frac{1}{\Delta F_{\nu or \bar{\nu}}} \times f \quad (3.16)$$

The cross-section sensitivity defined by Eq.3.13 can then be modified to be

$$\sigma_{effective} = \frac{|\delta\lambda/\lambda|}{\tau \times \Delta F_{\nu or \bar{\nu}}} \times f \quad (3.17)$$

where  $\tau$  is the mean lifetime of the isotopes,  $\Delta F_{\bar{\nu} or \nu}$  is the flux variation of the neutrino or antineutrino source. Hence, the cross section sensitivity is improved by a factor of  $f$ , the branching fraction.

In conclusion, the cross-section sensitivity is obtained from the measuring error of the decay rate parameter, mean lifetime of the isotope, the variation in the neutrino or antineutrino flux. The cross-section sensitivity obtainable at HFIR is at the level of approximately  $10^3$  to  $10^4$  times more sensitive than past published results. If a decay parameter variation were detected due to antineutrino interactions, the neutrino-nucleus interaction would occur at the level of strong interaction nuclear cross sections. The cross-section sensitivity from all references in the literature has been calculated based on Eq.3.13. The references in Table 3.7, Table 3.8 provide a complete review of the literature. These cross-section limits are also displayed in Figure 8.1.

Table 3.7.

Summary of experiments that conclude time-dependence of radioactive decay rate parameters. Estimation of the interaction cross section is based on Eq. 3.13 by inputting the associated size of effect, mean lifetime as well as neutrino or antineutrino flux from each reference. The variation of the solar neutrino flux is taken to be  $4.6 \times 10^9 \text{ } \nu \text{ cm}^{-2} \text{ sec}^{-1}$  on the Earth.

References That Conclude Time-dependence of Radioactive Decay Parameters							
Source	Reference	Mode	Detector Type	Measured Radiation	Size of Effect	$\nu$ or $\bar{\nu}$ Variations ( $cm^{-2}sec^{-1}$ )	Cross Section Sensitivity ( $cm^2$ )
$^3\text{H}$	Falkenberg (2001)[3]	$\beta^-$	Photodiodes	$\beta^-$	3.7E-03	4.6E+9	1.4E-21
$^3\text{H}$	Veprev(2012)[25]	$\beta^-$	Liq. Scintillation	$\beta^-$	2.0E-01	4.6E+9	7.8E-20
$^{22}\text{Na}/^{44}\text{Ti}$	O'Keefe(2013)[7]	$\beta^+, \epsilon$	Solid State (Ge)	$\gamma$	3.4E-04	4.6E+9	6.3E-22
$^{32}\text{Si}/^{36}\text{Cl}$	Alburger(1986)[1]	$\beta^-$	Gas proportional	$\beta^-$	5.0E-03	4.6E+9	1.6E-22
$^{36}\text{Cl}$	Jenkins(2012)[6]	$\beta^-$	Geiger-Muller	$\beta^-$	1.5E-02	4.6E+9	2.4E-25
$^{54}\text{Mn}$	Jenkins(2009)[21]	$\epsilon$	Scintillation	$\gamma$	1.0E-03	4.6E+9	5.6E-21
$^{60}\text{Co}$	Parkhomov (2005)[26]	$\beta^-$	Geiger-Muller	$\beta^-, \gamma$	3.0E-03	4.6E+9	2.7E-21
$^{60}\text{Co}$	Baurov(2007)[27]	$\beta^-$	Scintillation	$\gamma$	7.0E-03	4.6E+9	6.4E-21
$^{90}\text{Sr}/^{90}\text{Y}$	Parkhomov (2011)[28]	$\beta^-$	Geiger-Muller	$\beta^-$	2.3E-03	4.6E+9	3.8E-22
$^{90}\text{Sr}/^{90}\text{Y}$	Sturrock(2012) [16]	$\beta^-$	Geiger-Muller	$\beta^-$	2.3E-03	4.6E+9	3.8E-22
$^{90}\text{Sr}/^{90}\text{Y}$	Sturrock(2016)[18]	$\beta^-$	Liq.,Scintillation(TDCR)	$\beta^-$	2.0E-04	4.6E+9	3.3E-23
$^{137}\text{Cs}$	Baurov(2007)[27]	$\beta^-$	Scintillation	$\gamma$	2.0E-03	4.6E+9	3.2E-22
$^{226}\text{Ra}$	Jenkins(2009)[5]	$\alpha$	Ion Chamber	$\alpha$	2.0E-03	4.6E+9	6.0E-24

Table 3.8.

Summary of experiments that conclude **Null** evidence for radioactive decay rate parameter variation. Estimation of the interaction cross section is based on Eq. 3.13 by inputting the associated size of the effect, mean lifetime as well as neutrino or antineutrino flux from each reference. The variation of the solar neutrino flux is taken to be  $4.6 \times 10^9 \nu \text{ cm}^{-2} \text{ sec}^{-1}$  on the Earth. \* indicates the reactor antineutrino flux at various locations.

References That Conclude <b>Null</b> Evidence of Radioactive Decay Rate Parameters Variation						
Source	Reference	Mode	Detector Type	Measured Radiation	Sensitivity Variations ( $\text{cm}^{-2} \text{ sec}^{-1}$ )	Cross Section Sensitivity ( $\text{cm}^2$ )
$^3\text{H}$	Bruhn(2002)[29]	$\beta^-$	Photodiode	$\beta^-$	4.6E+9	7.8E-22
$^{22}\text{Na}/^{44}\text{Ti}$	Norman(2009)[33]	$\beta^+, \epsilon$	Solid State (Ge)	$\gamma$	4.6E+9	3.2E-21
$^{22}\text{Na}$	Meijer(2011)[35]	$\beta^+$	Solid State (Ge)	$\gamma$	5.0E+10*	3.4E-23
$^{22}\text{Na}$	Meijer(2014)[56]	$\beta^+$	Solid State (Ge)	$\gamma$	1.6E+13*	2.7E-26
$^{32}\text{Si}/^{36}\text{Cl}$	Semkow(2009)[30]	$\beta^-$	Gas proportional	$\beta^-$	4.6E+9	4.7E-23
$^{36}\text{Cl}$	Kossert(2014)[31]	$\beta^-$	Liq. Scintillation(TDCR)	$\beta^-$	4.6E+9	6.4E-27
$^{40}\text{K}$	Bellotti(2013)[19]	$\epsilon$	Scintillation(NaI)	$\gamma$	4.6E+9	4.0E-32
$^{54}\text{Mn}$	Meijer(2011)[35]	$\epsilon$	Solid State (Ge)	$\gamma$	5.0E+10*	2.1E-22
$^{90}\text{Sr}/^{90}\text{Y}$	Kossert(2015)[32]	$\beta^-$	Liq. Scintillation(TDCR)	$\beta^-$	4.6E+9	5.0E-23
$^{85}\text{Kr}$	Schrader (2010)[8]	$\beta^-$	Ion Chamber	$\gamma$	4.6E+9	2.2E-22
$^{108m}\text{Ag}$	Schrader (2010)[8]	$\epsilon$	Ion Chamber	$\gamma$	4.6E+9	9.9E-23
$^{133}\text{Ba}$	Schrader (2010)[8]	$\beta^-$	Ion Chamber	$\gamma$	4.6E+9	6.9E-22
$^{137}\text{Cs}$	Bellotti(2013)[19]	$\beta^-$	Scintillation	$\gamma$	4.6E+9	1.4E-23
$^{137}\text{Cs}$	Schrader (2010)[8]	$\beta^-$	Ion Chamber	$\gamma$	4.6E+9	7.4E-23
$^{137}\text{Cs}$	Meijer(2011)[35]	$\beta^-$	Solid State (Ge)	$\gamma$	5.0E+10*	2.5E-24
$^{152}\text{Eu}$	Meijer(2011)[35]	$\beta^-, \epsilon$	Sol. St. (Ge)	$\gamma$	5.0E+10*	4.5E-24
$^{152}\text{Eu}$	Siebert(1998)[12]	$\beta^-, \epsilon$	Ion Chamber	$\gamma$	4.6E+9	1.8E-22
$^{152}\text{Eu}$	Siebert(1998)[12]	$\beta^-, \epsilon$	Sol. St. (Ge)	$\gamma$	4.6E+9	1.6E-21
$^{152}\text{Eu}$	Schrader (2010)[8]	$\beta^-, \epsilon$	Ion Chamber	$\gamma$	4.6E+9	1.8E-22
$^{154}\text{Eu}$	Siebert(1998)[12]	$\beta^-, \epsilon$	Ion Chamber	$\gamma$	4.6E+9	2.8E-22
$^{154}\text{Eu}$	Siebert(1998)[12]	$\beta^-, \epsilon$	Sol. St. (Ge)	$\gamma$	4.6E+9	1.7E-20
$^{154}\text{Eu}$	Schrader (2010)[8]	$\beta^-, \epsilon$	Ion Chamber	$\gamma$	4.6E+9	2.8E-22
$^{155}\text{Eu}$	Siebert(1998)[12]	$\beta^-$	Sol. St. (Ge)	$\gamma$	4.6E+9	3.0E-20
$^{226}\text{Ra}$	Siebert(1998)[12]	$\alpha$	Ion Chamber	$\alpha$	4.6E+9	3.0E-24
$^{226}\text{Ra}$	Semkow(2009)[30]	$\alpha$	Ion Chamber	$\alpha$	4.6E+9	9.1E-24
$^{238}\text{Pu}$	Cooper(2009)[34]	$\alpha$	Radioisotope Thermoelectric	$\alpha$	4.6E+9	4.6E-24

## 4. Experimental Configuration at High Flux Isotope Reactor

The experiment used a 60% High Purity Germanium Detector Spectrometer (HPGe) system to test the variation of the decay rate parameter of  $^{54}\text{Mn}$ . The HPGe has an energy resolution  $\delta E/E \sim 1.67 \times 10^{-3}$  at  $E_\gamma = 1.33$  MeV measured using a  $^{60}\text{Co}$  button source placed at the center of the HPGe detectors face. The antineutrino source for the experiment is the High Flux Isotope Reactor (HFIR) located at Oak Ridge National Lab at Tennessee, USA. The HPGe system, and shielding house were designed, built, and tested at Purdue, and then shipped to HFIR for the experiment.

### 4.1 High Flux Isotope Reactor (HFIR)

High Flux Isotope Reactor (HFIR) is a light-water-cooled, and moderated, beryllium-reflected, and flux-trap type reactor[57]. The original purpose of HFIR is for the production of transuranic isotopes. The goal of HFIR includes materials irradiation,



Figure 4.1. High Flux Isotope Reactor at Oak Ridge National Lab

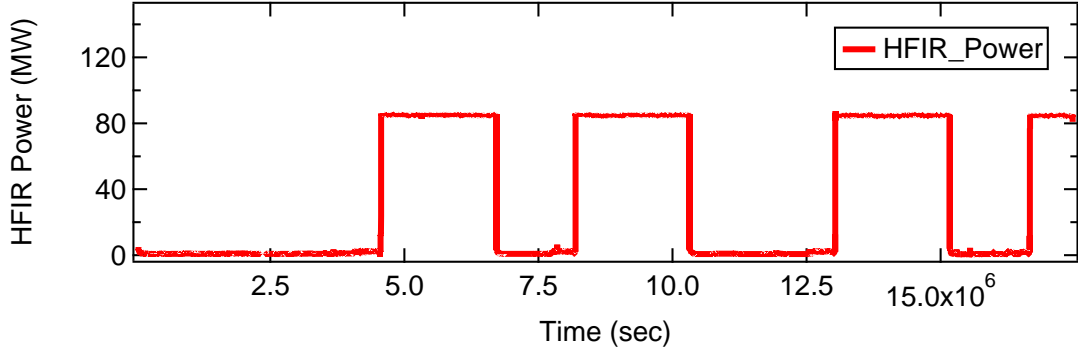


Figure 4.2. The power as a function of time of High Flux Isotope Reactor at Oak Ridge National Lab during this experiment. Three independent detectors are used to verify the stability of the reactor power. The average power was measured to be  $86.007 \pm 0.22$  MW.

neutron activation, and neutron scattering. It has a peak thermal neutron (25 meV) fluence of  $2.5 \times 10^{15} \text{ n cm}^{-2} \text{ sec}^{-1}$ . The thermal neutron flux of the HFIR core is  $\sim 100$  times higher than cores of commercial nuclear power plants ( $\sim 10^{13} \text{ n cm}^{-2} \text{ sec}^{-1}$ ). HFIR uses highly enriched  $^{235}\text{U}$  (HEU) as the fuel. The operating cycle normally consists of full-power operation for approximately 23-27 days at  $\sim 86$  MW. Figure 4.2 is the HFIR reactor power as a function of time during this experiment. The average operating power was calculated from the recorded reactor power data taken every second, and is  $86.007 \pm 0.22$  MW. The reactor power is very stable with a variance of  $\delta p / p_{\text{mean}} \sim 2.6 \times 10^{-3}$ , where  $\delta p$  is the standard deviation of the average power, and  $p_{\text{mean}}$  is the average power of HFIR in operation.

## 4.2 Reactor-Generated Antineutrinos

Nuclear power reactors are the brightest antineutrino sources. Antineutrinos are produced from the unstable fission fragments decay. The excess neutrons undergo  $\beta^-$

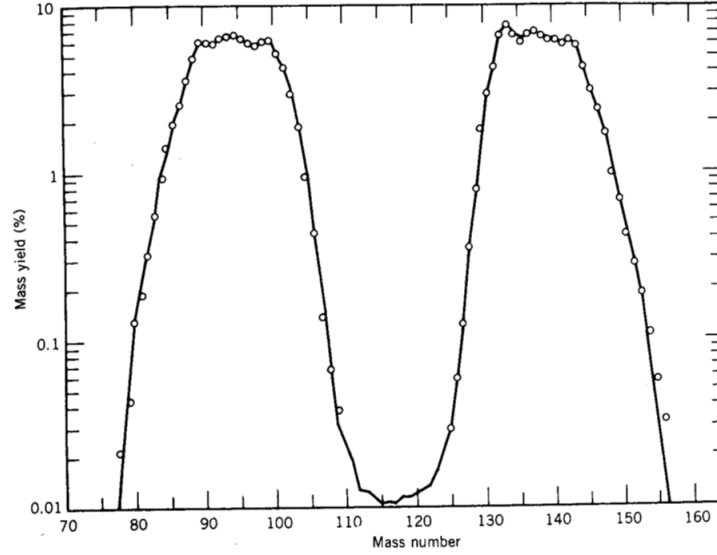
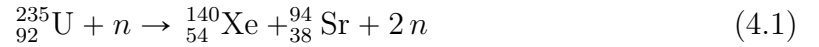
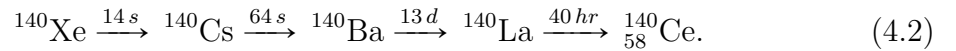


Figure 4.3. Mass distribution of  $^{235}\text{U}$  fission fragments[58]. The possible fission fragments are centered around  $A \sim 95$ , and  $A \sim 137$  which must share the original 92 protons. A typical pair of fragments from  $^{235}\text{U}$  fission are Xenon( $A=140$ ), and Strontium( $A=94$ ).

decay which produces protons, electrons, and antineutrinos as the fragments move towards stability. While the fission fragments are not unique, a possible reaction is



which illustrates the asymmetric mass distribution of the produced fragments shown in Figure 4.3. Most of these fission fragments are highly unstable (radioactive), and undergo further radioactive decays to stabilize. For example,  $^{140}_{54}\text{Xe}$  will decay to  $^{140}_{58}\text{Ce}$  via  $\beta^-$  decay, generating the possible decay chain



Likewise,  $^{94}_{38}\text{Sr}$  will decay to  $^{94}_{40}\text{Zr}$  via  $\beta^-$  decay, and follow the possible chain to stabilize,



In this example, the stable end chain nuclei have a total of 98 protons, and 136 neutrons. The fission fragments (parent nuclei) have together 92 protons, and 142 neutrons. Thus, 6 neutrons have  $\beta$ -decayed to protons. Similarly, for each  $^{235}\text{U}$  fission, the fission fragments have on average six negative beta decays (6 neutrons must decay to 6 protons) which results in six antineutrinos produced per each fission.

### 4.3 Flux of Antineutrinos at High Flux Isotope Reactor

The average antineutrino flux can be estimated by the fissile fuel composition,  $^{235}\text{U}$ , in the HFIR core, and the reactor's thermal power. Because the antineutrino flux is related to the reactor thermal power, the reactor antineutrino flux impinging on a detector can be accurately calculated. The antineutrino flux at HFIR is

$$\frac{dN_{\bar{\nu}}}{dt} = n_{\bar{\nu}} \times \frac{P_H}{E_F} \quad (4.4)$$

where  $P_H$  is the average thermal power output,  $E_F$  is average released thermal energy per fission, and  $n_{\bar{\nu}}$  is the average number of antineutrino generated per fission.

Table 4.1 displays the parameters needed to find the antineutrino flux for the most common reactor fuels. The thermal energy released per each fission of  $^{235}\text{U}$  is

$$\begin{aligned} E_f &= E_F - \langle E_{\bar{\nu}} \rangle \times n_{\bar{\nu}} \\ &= 201.7 - 1.46 \times 5.58 \\ &= 193.6 \text{ MeV} \end{aligned} \quad (4.5)$$



Table 4.1.  
Antineutrino characteristics from  $^{235}\text{U}$ ,  $^{238}\text{U}$ ,  $^{239}\text{Pu}$ , and  $^{241}\text{Pu}$ [59].

Type of Fuel	$^{235}\text{U}$	$^{238}\text{U}$	$^{239}\text{Pu}$	$^{241}\text{Pu}$
Released energy per fission ( $E_F$ )(MeV)	201.7	205	210	212.4
Mean energy of $\bar{\nu}$ ( $\langle E_{\bar{\nu}} \rangle$ )(MeV)	1.46	1.56	1.32	1.44
Number of $\bar{\nu}$ per fission ( $n_{\bar{\nu}}$ )( $E > 1.8$ MeV)	5.58	6.69	5.09	5.89

where  $E_F$  is the released energy per fission, and  $\langle E_{\bar{\nu}} \rangle$  is the mean energy of the antineutrinos. Hence, the typical rate of  $\dot{N}_{\bar{\nu}}$  from the HFIR reactor core is given by

$$\begin{aligned}\dot{N}_{\bar{\nu}} &= 5.58 \times \frac{86.007 \text{ MW}}{193.6 \text{ MeV}} \\ &= 1.53 \times 10^{19} \bar{\nu} \text{ sec}^{-1}.\end{aligned}\tag{4.6}$$

At a distance,  $d = 6.53 \text{ m}$  from the core, the antineutrino flux at the HPGe detector, assuming the core is a point source, is estimated to be

$$\begin{aligned}F_{\bar{\nu}(\text{HFIR})} &= \frac{1.53 \times 10^{19} \bar{\nu} \text{ sec}^{-1}}{4\pi(653)^2 \text{ cm}^2} \\ &= 2.86 \times 10^{12} \bar{\nu} \text{ cm}^{-2} \text{ sec}^{-1}\end{aligned}\tag{4.7}$$

which is nearly 50 times higher than the solar neutrino flux on the Earth, and more than 600 times higher than the variation in the solar neutrino flux on the Earth.

#### 4.4 Experiment Layout at HFIR

The HPGe spectrometer layout at HFIR is shown in Figure 4.5. The use of 5.5 tons of lead, as well as copper, aluminum, and borated poly shielding, reduced the background radiation activity by a factor of one thousand to the level of a few counts per second full spectrum (3 KeV to 3 MeV). Two ORTEC HPGe detectors are used for collecting the source, and background spectrum. The detectors are cooled by X-Cooler-3 mechanical Liquid-Nitrogen-Free chillers, and the signal processing is per-

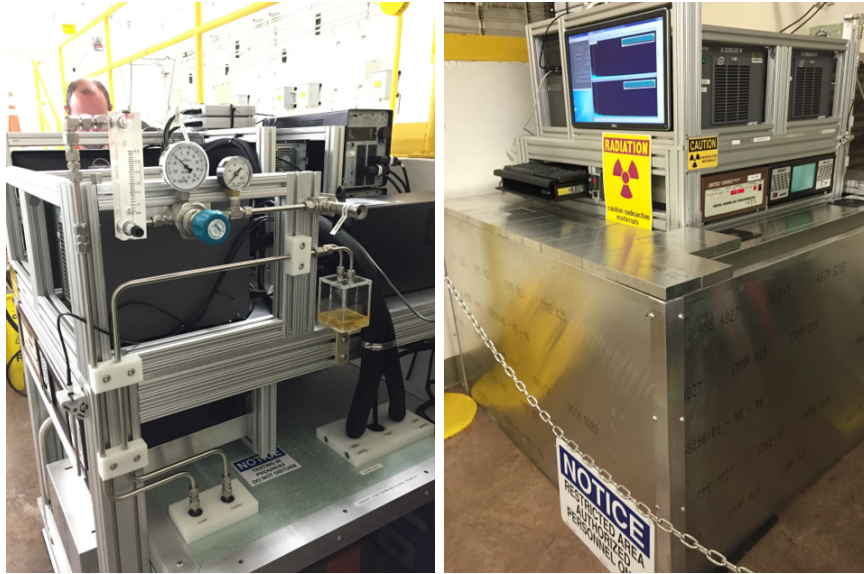


Figure 4.4. (Left) Nitrogen gas atmosphere to reduce reactor produced  $^{40}\text{Ar}$  in the housing, and eliminate humidity to the detector. (Right) HPGGe detector spectrometer system in operation at HFIR

formed by a Digital Spectrometer (DSPEC-50) multichannel analyzers. The detectors are housed in a temperature controlled enclosure, which is continuously flushed with high purity nitrogen to eliminate condensation, and to isolate the detector from the reactor produced  $^{40}\text{Ar}$  radioactive background. The daily spectrum was saved into a computer which can be remotely controlled from off-site. The data was uploaded to an online storage service for further processing. The output spectra have been corrected, and produced by a 320 cores Intel Xeon E5450 cluster with MATLAB programming.

A well-known source for systematic error in counting experiments is a detector's response to ambient environmental factors such as temperature, pressure, and relative humidity. Variations in the ambient environmental factors can produce effects that mimic fundamental interactions if not accounted for. Figure 4.6 shows the ambient

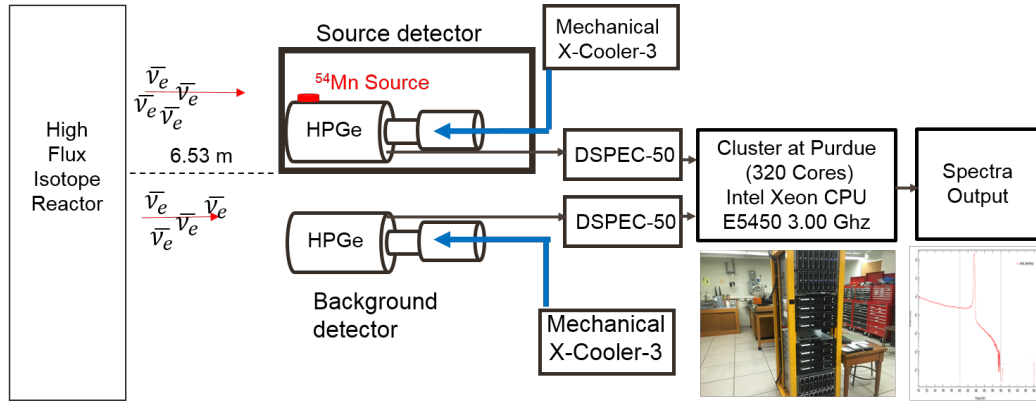


Figure 4.5. Experimental Layout at HFIR, The HPGe detector system is located 6.53 meter from the reactor core. The flux is  $2.86 \times 10^{12} \bar{\nu} \text{ cm}^{-2} \text{ sec}^{-1}$  when the reactor is in operation. One HPGe detector is to measure the  $^{54}\text{Mn}$  Source spectrum. The other HPGe detector is to monitor the background rate. A DSPEC collects, and analyzes the voltage pulses from the HPGe detector. Two mechanical cooler keep the HPGe detectors near liquid nitrogen temperature. Data Processing used a 320 cores Intel Xeon E5450 based cluster with MATLAB programming.

temperature, pressure, and relative humidity as a function of time.

The ambient pressure oscillations are limited to  $\delta P/P \sim 0.6\%$ , and behaves randomly as shown in Figure 4.6.

The ambient temperature shown in Figure 4.6 shows a  $\sim 27\%$  oscillation during the reactor-off Period 1. The ambient temperature also has some small  $\sim 10\%$  variation in Period 2, Period 3, and Period 4. The ambient temperature displays a significant  $\sim 20\%$  drop in the reactor-off Period 5, and reactor-on Period 6, caused by an outage of the air conditioning in the HFIR facility lasting about one month. These ambient temperatures variations are addressed as corrections by the study of variations in the relation between the ambient temperature, and the daily decay rate

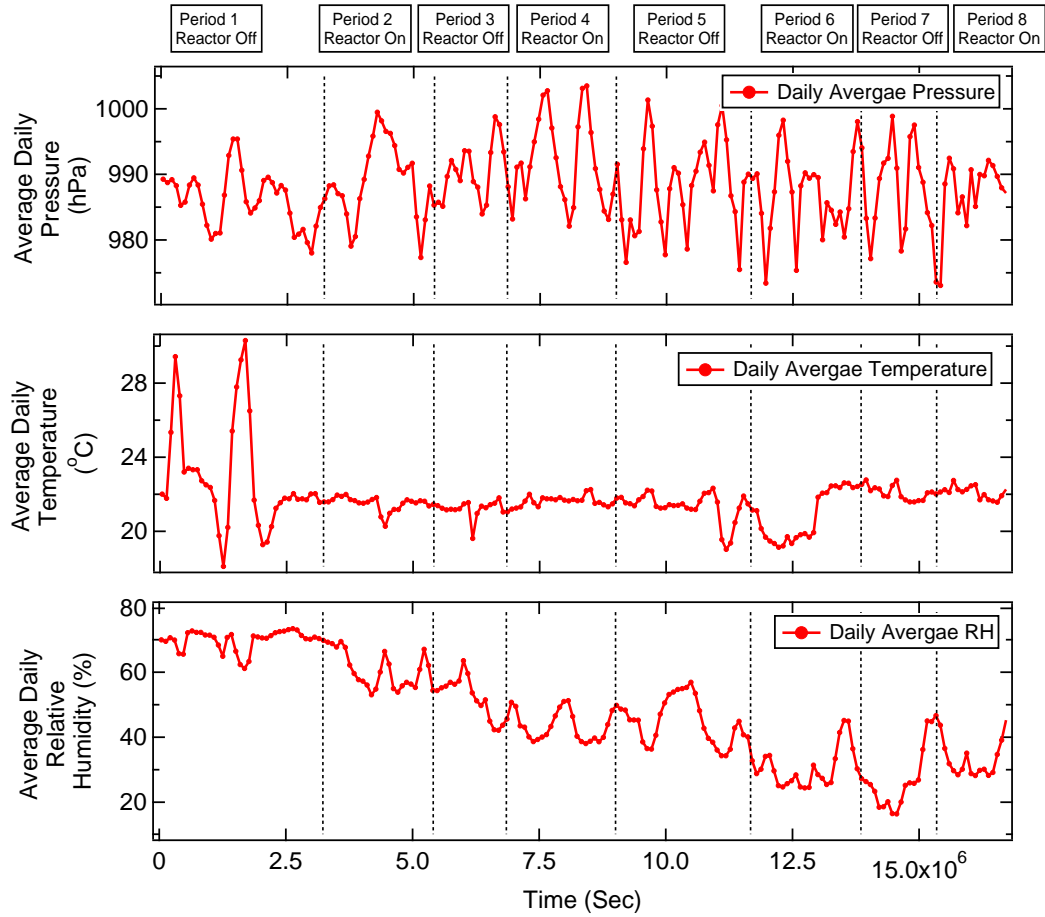


Figure 4.6. Ambient pressure, temperature, and humidity as a function of time at HFIR.

fitting residuals, using a side band method.

The relative humidity shown in Figure 4.6 has a decreasing trend due to the seasons; starting high at the start of the experiment in August, and decreasing towards spring at the experiment's end. The humidity has been fit to

$$h(t) = h_0 + A \sin(\omega t + \phi) \quad (4.8)$$

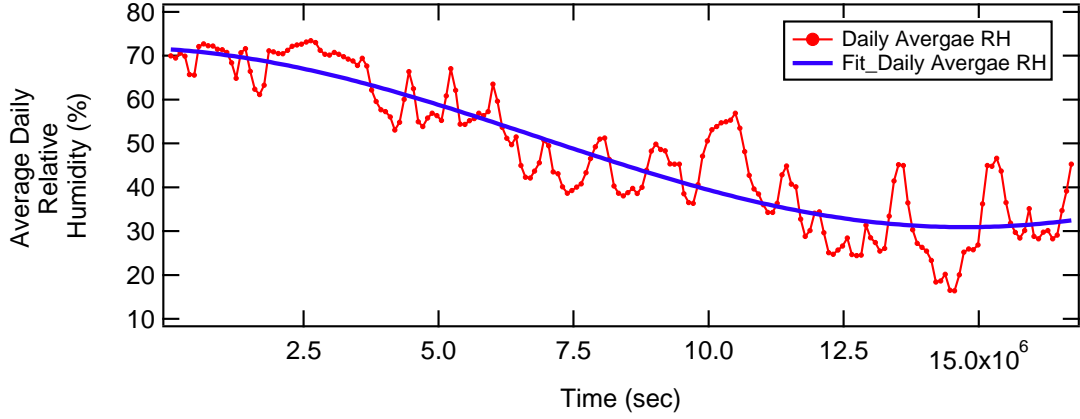


Figure 4.7. Daily average humidity fitted with in phase periodic function (Eq. 4.8), fixed at 1 year, as a function of time.

Table 4.2.

The yearly cycling of the humidity relative to the experiments starting date

Fixed $\omega=1$ year	Phase ( $\phi$ )
In Phase	$-79 \pm 1$ day
Out of Phase	$103 \pm 1$ day

and is shown in Figure 4.7, for the case,  $\omega$  is fixed at one year to match the cycling of the seasons. Two cases are fit, the data, and the negative of the data in order to compare with other in phase, and out of phase distributions. The results are shown in Table 4.2.

#### 4.5 High Purity Germanium Detector (HPGe)

An HPGe detector behaves in a way similar to a semiconducting diode detector. The incoming  $\gamma$  ray is absorbed by the crystal creating electron, and hole charge carriers generated proportional to the ratio  $E_\gamma/E_{Gap}(0.72eV)$ . The charge carriers are drawn to the inner, and outer contacts by the bias voltage. HPGe detectors are

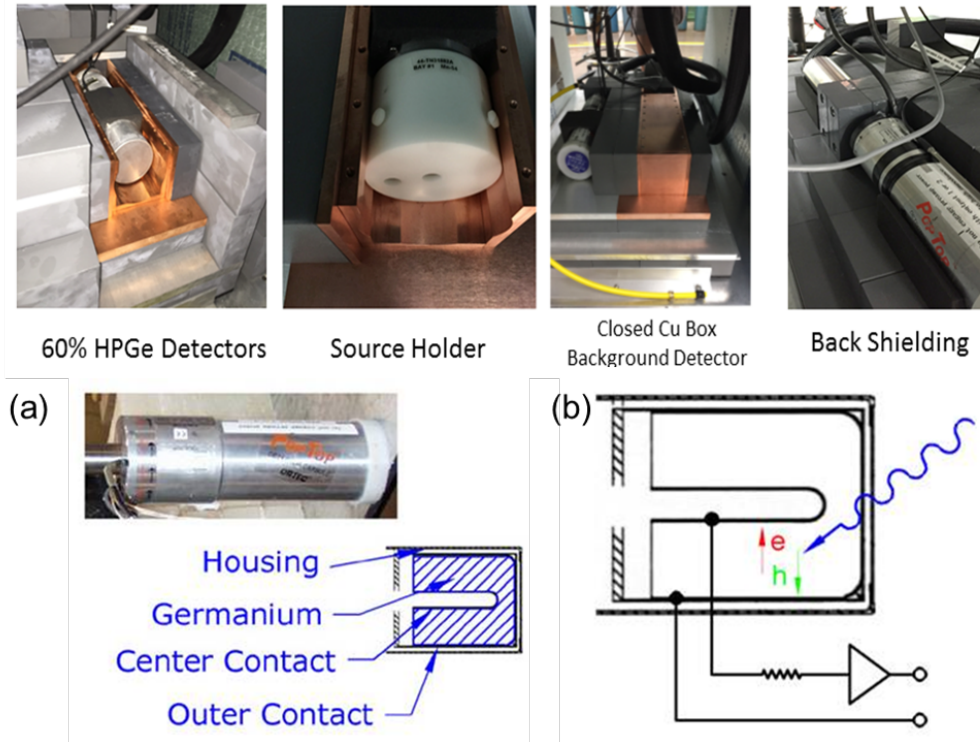


Figure 4.8. Configuration of High Purity Germanium Detector (HPGe). (a) The HPGe detector is encased in a vacuum housing. (b) The incoming gamma ray is absorbed by the crystal, and a proportional number of electron-hole charge carrier are generated. The current is sensed 1st by a cold pre-amplifier, and converted to an electric pulse.

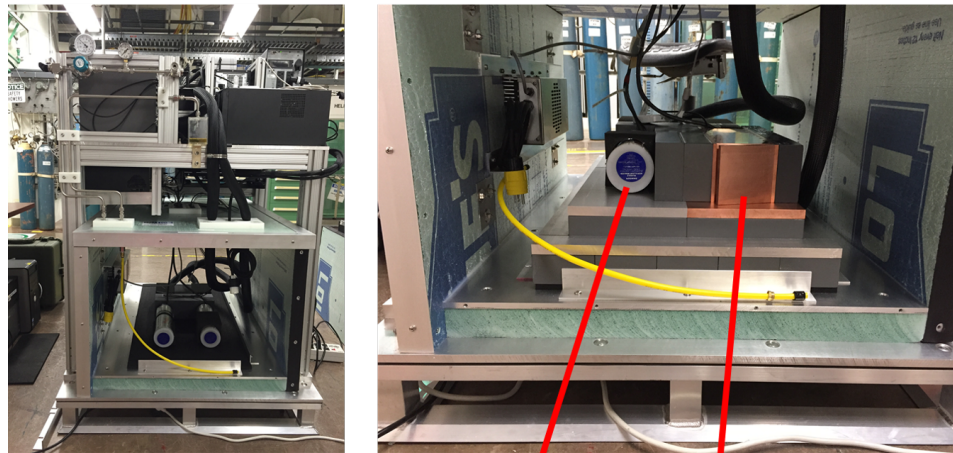
unable to operate at room temperature due to a large number of electrons able to cross the band gap of the Ge crystal. For this reason, the operational temperature of HPGe detectors was  $\sim 84^\circ\text{K}$  eliminating the probability of thermally excited electrons crossing the band gap into the conduction band of the crystal.

Charge carrier can be trapped on radiation-induced defects in the Ge crystal. This has the effect of broadening the line shape. For this reason, the line shape is not Gaussian, and in fact, no model can properly describe the trapping effects to the  $10^{-5}$  accuracy required in this experiment. Nonetheless, HPGe detectors have excellent

linearity as they are a gain-one device. An HPGe detector is to first order insensitive to low levels of external electric fields, magnetic fields, and ambient temperature variations.

#### 4.6 Shielding Performance, and Background Stability of the HPGe Detector

Background radiation is any radiation present in the environment which is not from the radiation source of interest. The background radiation in HFIR is due to (1) the neutrons, and gamma rays directly produced from the reactor operation, (2) cosmic radiation, (3) HPGe detector itself, (4) neutron activated building components, (5) scattered radiation from the nearby beamline operations, (6) shielding materials, (7) decay radiation from the nearby source storage room, and (8) natural



Two HPGe detectors, for **Background** and **Source** Radiations

Figure 4.9. (Left) The HPGe detector measured the background spectrum at HFIR. (Right) The HPGe source detector measured the source spectrum. Various material such as lead, aluminum, copper, and borated poly shielding have been utilized to reduce the background radiation. The complete shielding is not shown in these pictures.



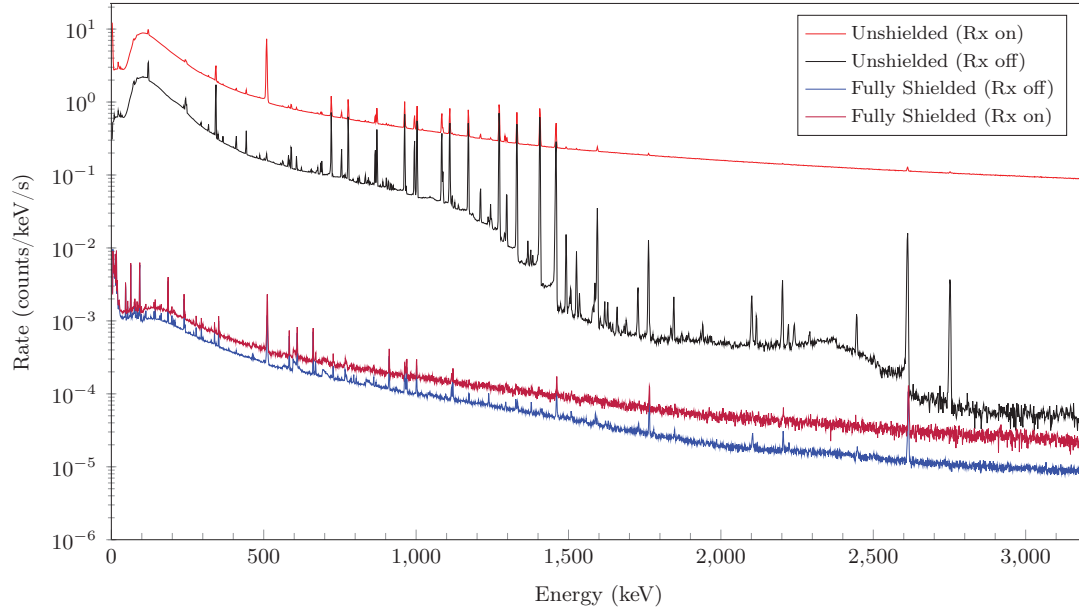


Figure 4.10. HFIR background spectra with, and without shielding in the reactor on or off status. The spectra show that the shielding was effective in suppressing the backgrounds by a factor greater than  $1.8 \times 10^{-4}$  (reactor-on), and  $6.7 \times 10^{-4}$  (reactor-off).

radioactivity within the building. As the detector is 6.53 meter from the HFIR core, the gamma rays, and neutrons produced during reactor operations are significant, and indeed become the dominant background source in the HPGe spectrometer. Various materials have been used to reduce the background based on absorption cross sections. Lead, copper, and aluminum are utilized for the  $\gamma$ -ray shielding. Borated-poly is for neutron shielding. The copper is to eliminate the fluorescence from lead, and the aluminum to eliminate the fluorescence from the copper. Figure 4.10 shows the background radiation with, and without shielding during reactor-on, and reactor-off periods. The spectra show that the shielding is effective in suppressing the backgrounds by a factor greater than  $1.8 \times 10^{-4}$  (reactor-on), and  $6.7 \times 10^{-4}$  (reactor-off).

The background spectra were collected in order to subtract the background from the  $^{54}\text{Mn}$  source spectra. The background data were collected for nearly 90 days con-



sisting of hourly, daily, and 10 days background runs after the  $^{54}\text{Mn}$  was removed on 03/09/2016. The full background measurement includes two reactor-on periods, and one reactor-off period. Before background subtraction, the time-dependence stability of the background rate is checked.

The total error in the channel by channel rate calculation in a single spectrum is given by

$$\sigma_i^2 = \frac{N_i}{(\Delta t)^2} + \frac{N_i^2}{(\Delta t)^2} \times \frac{(\delta t)^2}{(\Delta t)^2} \quad (4.9)$$

where  $N_i$  is the count for each channel of the background spectrum, and  $\Delta t$  is the live time of that background spectrum. The 1st term is the Poisson distributed statistical error, and the 2nd term is the timing error from the DSPEC-50. The DSPEC-50 reports out the live-times to an accuracy of 0.1 sec. The uncertainty due to the timing error in a uniform distribution is  $\delta t = 0.1\text{sec}/\sqrt{12} \sim 0.029$  sec.

Figure 4.11 shows the full background spectrum rate as a function of time after removing of the  $^{54}\text{Mn}$  source. Table 4.3 summarizes all the information during the background collection periods. Timing errors from the DSPEC-50 are below  $8.13 \times 10^{-7}\text{cps}$  which are negligible but tracked throughout the analysis. The rate distributions for the runs taken in Period 1, Period 2, and Period 3 are Gaussian (Figure 4.11). The width of the distributions are in agreement with the estimate found using the averaged error of the mean found for each run. As shown in Table 4.3, the statistical mean run error, and the width of the run rate distribution are in agreement. This means the calculated errors are correct as proven by the distributions.

The means of three reactor-off Periods 2, 3, and 4 are in excellent agreement with their individual variation from the averaged mean shown in the standard deviation row in Table 4.3. These results prove the background is exceptionally stable over the 74-days reactor-off period. All the reactor-off data are used for the background subtraction. The two reactor-on Period 1, and 5 are in disagreement at the level of

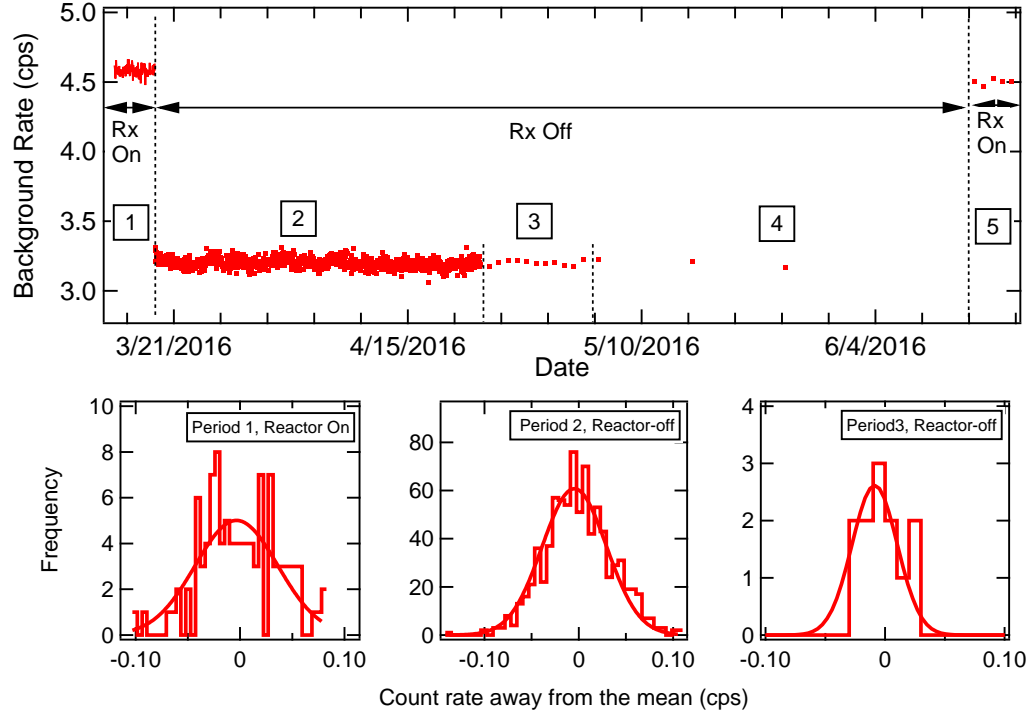


Figure 4.11. (Top) Full background spectrum rate as a function of time which includes reactor-on, and reactor-off cycles with the  $^{54}\text{Mn}$  source removed. (Left Lower) The distribution away from the mean in count rate for 1-hour runs in reactor-on Period 1. (Center Lower) The distribution away from the mean in count rate for 1-hour runs in reactor-off Period 2. (Right Lower) The distribution away from the mean in count rate for 1-day runs in reactor-off Period 3.

$0.04 \pm 0.005\text{cps}$  from the mean. While the disagreement is small, it is significant. The Period 1 data was discarded since Period 1 started just after removing the  $^{54}\text{Mn}$  source by deconstruction of the shielding, and reconstruction over a period of about a week. The 5-day Period 1 data is considered unstable as the detector system needed time to reach equilibrium. For this reason, the reactor-on background used for corrections only included Period 5, consisting of the average of 5 1-day runs.

The average full spectrum rate for the reactor-on background is  $4.502 \pm 0.003\text{cps}$  from Period 5. The average rate for the reactor-off background is  $3.2003 \pm 0.0007\text{cps}$

using Period 2, Period 3, and Period 4, that is the average of the 74 days of runs.

The average rate of  $^{54}\text{Mn}$  full spectrum is  $\sim 6500\text{cps}$ . From this, the estimated error level for the reactor-on background spectrum is  $\sim 6 \times 10^{-7}$ , and the reactor-off background error is  $\sim 1 \times 10^{-7}$ . Both are small enough to be neglected but are tracked throughout the analysis.

Table 4.3.

The average background rate, and associated error during the reactor-on or reactor-off periods at HFIR. The distribution error is not available in Period 4, and 5 due to lack of data points. S.D. means the standard deviation. The S.D from the mean is not available for reactor-on Period 1, and 5 because Period 1 data was dropped from the analysis (see text)

	Period 1	Period 2	Period 3	Period 4	Period 5
Reactor status	on	off	off	off	on
Duration (Days)	5	32	12	30	5
Single run time	1-hour	1-hour	1-day	10-day	1-day
Timing error(cps)	8.13E-07	6.77E-07	2.65E-08	2.66E-09	3.00E-08
Statistical mean run error(cps)	3.57E-02	2.99E-02	6.09E-03	1.93E-03	7.32E-03
Distribution error(cps)	3.95E-02	3.34E-02	1.80E-2	N/A	N/A
Mean rate(cps)	4.581 $\pm$ 0.004	3.2001 $\pm$ 0.001	3.199 $\pm$ 0.002	3.201 $\pm$ 0.001	4.501 $\pm$ 0.003
Reactor-off S.D. from the mean	N/A	0.28	0.63	0.74	N/A
The average rate in all reactor-off periods : 3.2003 $\pm$ 0.0007 cps					
The average rate in all reactor-on periods : 4.502 $\pm$ 0.003 cps					

## 5. Energy Calibration of the $^{54}\text{Mn}$ , and the Background Spectra at HFIR

High Purity Germanium (HPGe) detector gamma-ray spectroscopy has wide-ranging applications. HPGe detector must be calibrated before proceeding with data correction, and analysis. That is, the relationship must be known between the energy deposited in the detector by a gamma ray, and the amplitude of the corresponding amplifier output pulse. The energy range sensitivity of commercial spectrometer systems ranges from 3 KeV to over 12 MeV. Because the Ge crystal is a gain-1 device, it is standard practice to use a linear relationship between the channel scale, and the energy scale. However, in this experiment, the electronics introduced a nonlinear term into the calibration.

To measure the calibration accurately, spectral lines are measured over the full energy range. For background spectra, 13 lines between 3 KeV, and 3 MeV were used in the calibration. These lines are produced by neutrons, neutron-induced ambient background, beta decay transitions induced by neutrons, atomic fluorescence, and natural environmental backgrounds. Because the  $^{54}\text{Mn}$  source overwhelms these background calibration lines, the  $^{54}\text{Mn}$  spectra have been calibrated using the Indium X-ray K-edge peak, the Compton edge, and back-scattered peak, the  $^{54}\text{Mn}$  photopeak, and a  $^{208}\text{Tl}$  gamma line. Both spectra type used a two-step calibration process. First, fitting the line shape for its centroid, and, second, combining all the fitting information into the non-linear detector calibration.

## 5.1 Energy Calibration of Background Spectra

Background spectra were collected in the HPGe detector with the source removed while the reactor was both in on, and off status. The background reactor-on data set was collected, from June 14, 2016, to June 19, 2016, consisting of approximately 120 hours of data. The data set consisted of 5 independent 24-hour spectra. Additional reactor-on data, consisting of 5 days of 1-hour runs, were discarded as discussed in Chapter 4. The reactor-off data set was collected from March 19, 2016, to June 04, 2016, consisting of 833 independent 1-hour spectra, 12 independent 1-day spectra, and 3 independent 10-days spectra. Figure 5.1, and Table 5.1 show the 13 spectral lines used in this calibration. The background data calibration process involves fitting the line shape for the centroid, and second combining all the fitted information into the detector calibration. The line shape was assumed to be a Gaussian distribution

Table 5.1.

Spectral lines used in the calibration of the background energy calibration. Accepted energies are from the National Nuclear Data Center, Brookhaven National Laboratory, based on ENSDF[60]. Accepted centroids are the fit bin number.

	Nuclide	Accepted Energy(KeV)	Accepted Centroid(No.)
1	$^{210}\text{Pb}$	$46.5390 \pm 0.0023$	$205.4116 \pm 0.0101$
2	$^{234}\text{Th}$	$63.2900 \pm 0.0200$	$279.7169 \pm 0.0889$
3	$^{234}\text{Th}$	$92.6000 \pm 0.0200$	$409.6237 \pm 0.0889$
4	$^{208}\text{Tl}$	$583.1870 \pm 0.0091$	$2582.2496 \pm 0.0403$
5	$^{214}\text{Bi}$	$609.3200 \pm 0.0090$	$2697.5935 \pm 0.0400$
6	$^{137}\text{Cs}$	$661.6570 \pm 0.0073$	$2929.7250 \pm 0.0325$
7	$^{228}\text{Ac}$	$911.2040 \pm 0.0129$	$4034.3824 \pm 0.0575$
8	$^{228}\text{Ac}$	$968.9710 \pm 0.0206$	$4290.3542 \pm 0.0914$
9	$^{234m}\text{Pa}$	$1001.0300 \pm 0.1000$	$4433.2512 \pm 0.4444$
10	$^{214}\text{Bi}$	$1120.2940 \pm 0.0325$	$4960.8312 \pm 0.1445$
11	$^{40}\text{K}$	$1460.8220 \pm 0.0324$	$6469.5223 \pm 0.1438$
12	$^{214}\text{Bi}$	$1764.4910 \pm 0.0328$	$7815.7520 \pm 0.1460$
13	$^{208}\text{Tl}$	$2614.5110 \pm 0.0224$	$11582.8926 \pm 0.0995$

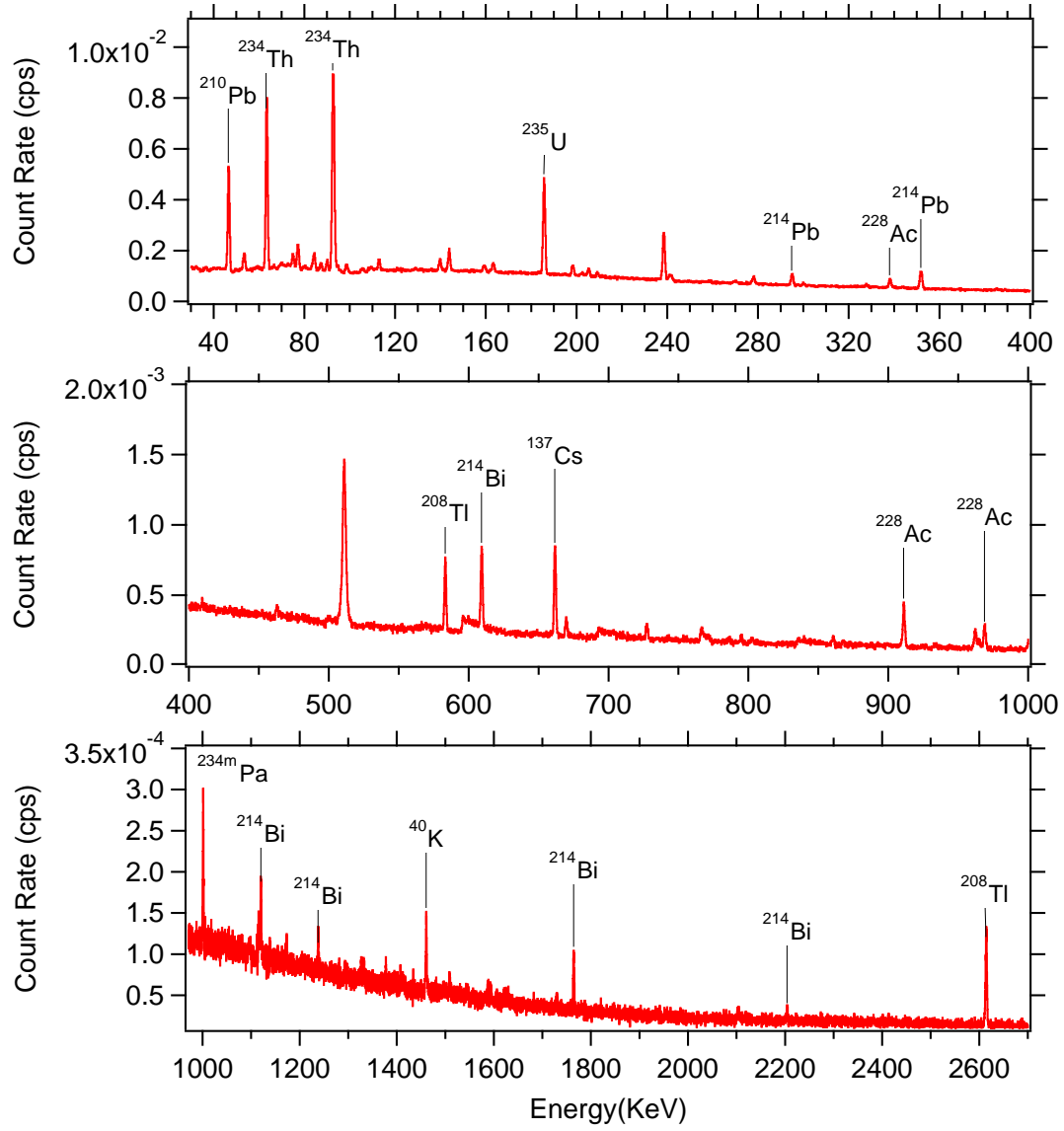


Figure 5.1. Background spectrum with 19 identified lines at HFIR. 13 spectral lines have been selected for the background spectrum energy calibration shown in Table 5.1.

with a continuous background,

$$f(x) = a + bx + cx^2 + \frac{A}{\sqrt{2\pi}\sigma} \exp\left(\frac{-(x - x_0)^2}{2\sigma^2}\right) \quad (5.1)$$

Table 5.2.

Calibration coefficients of background spectra with reactor-off for linear, and nonlinear calibration.  $\chi^2$  per degree of freedom significantly improves with the nonlinear calibration.

Background Spectral with Reactor Off Status				
Type of Calibration	$a_{back}$ (KeV)	$b_{back}$ (KeV/No.)	$c_{back}$ (KeV/No. <sup>2</sup> )	$\chi^2/DoF$
Linear	0.1824 $\pm$ 0.0032	0.2257 $\pm$ 1.7E-6	N/A	60.84
Non-linear	0.1466 $\pm$ 0.0024	0.2258 $\pm$ 2.4E-6	-1.1E-08 $\pm$ 4.0E-10	6.46
Background Spectral with Reactor On Status				
Linear	0.1578 $\pm$ 0.0094	0.2257 $\pm$ 6E-6	N/A	6.61
Non-linear	0.1222 $\pm$ 0.0072	0.2257 $\pm$ 8E-6	-1.2E-08 $\pm$ 1E-9	1.29

where  $a$ ,  $b$ , and  $c$  are the coefficients of the continuous background,  $A$  is the counts under the Gaussian distribution,  $x_0$  is the centroid, and  $\sigma$  is the energy resolution of the line shape. A  $\chi^2$  per degree of freedom minimization is performed using Poisson statistics weighting ( $\sqrt{N_i}$ ). The accepted line energies are from the National Nuclear Data Center(NNDC), Brookhaven National Laboratory, based on ENSDF[60]. However, the centroid resolution of the HPGe detector is not as well controlled as the uncertainty given by the standard values from the NNDC. The line shape in an HPGe detector is not well-known function if high accuracy is required. Because the measuring resolution is on the order of 1 keV, and the number of counts in each line varies considerably, it was decided to fix the error assigned to each reference line to the uncertainty listed by the NNDC or the measured error found from the fitting, whichever was larger. This method was selected so that no single line dominated the calibration fit, and the errors were dominated by the statistics, and the energy resolution of the measurements.

The Ge crystal in the HPGe detector is a gain-1 device, so it is standard practice



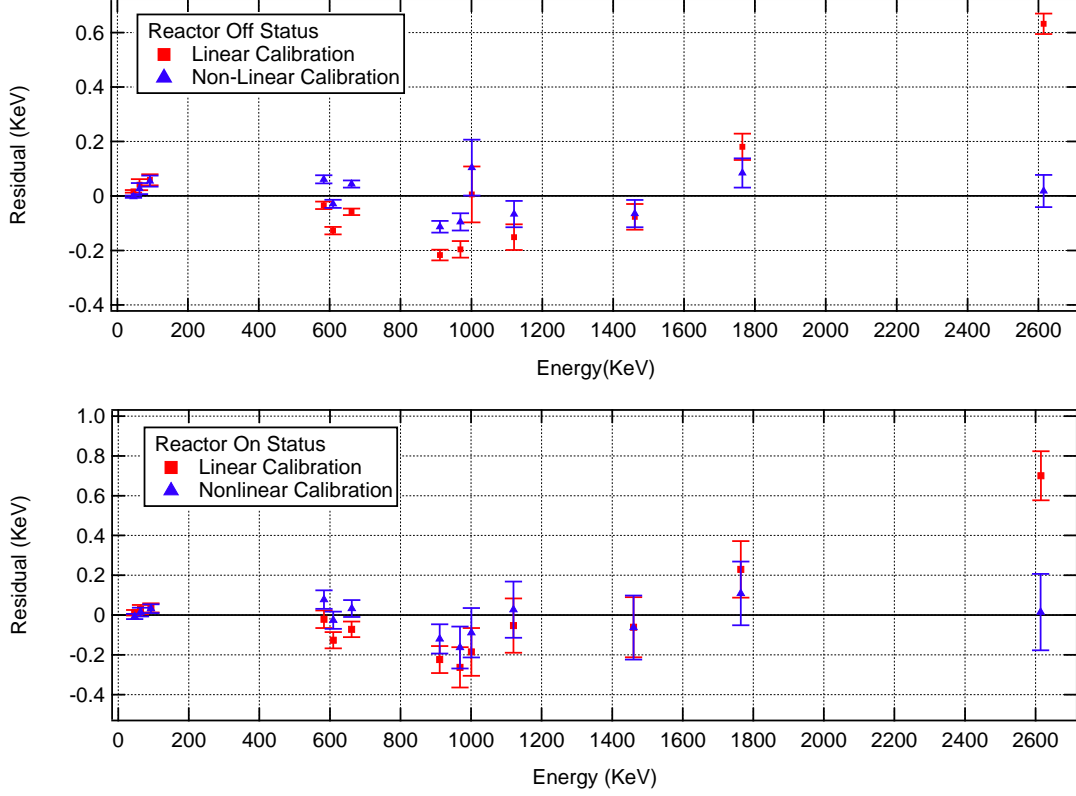


Figure 5.2. Background spectral line residuals for reactor-off, and reactor-on status. The nonlinear calibration for this experiment reduces standard deviation in the residuals of the background spectral lines.

to use a linear relationship between the channel scale, and the energy scale.

$$E_i = a_{back} + b_{back} \times i \quad (5.2)$$

The energy( $E_i$ ) is equated to the channel number ( $i$ ) using two constants  $a_{back}$ , and  $b_{back}$  for the background calibrations. To check the goodness of the background calibration, Figure 5.2 shows the residual at each spectral line for the reactor-off, and reactor-on calibration using the linear conversion. The total  $\chi^2$  per degree of freedom( $\chi^2_{DoF}$ ) for the linear calibration is 60.84 for the reactor-off data, and 6.61 for the reactor-on data. These results are not acceptable values. The residuals of the

background spectral lines with both reactor-on, and reactor-off are many standard deviations away from the fit. Because the experiment requires a high precision correction at the level of  $10^{-5}$ , further calibration of the background spectrum is necessary. While the HPGe detector response should be linear, the amplifier, and DSPEC-50 electronics are likely sources of the non-linear behavior. To improve the accuracy, a second-order nonlinear calibration is assumed,

$$E_i = a_{back} + b_{back} \times i + c_{back} \times i^2 \quad (5.3)$$

where  $a_{back}$ ,  $b_{back}$ , and  $c_{back}$  are the calibration coefficients. The  $\chi^2$  per degree of freedom significantly drops to 6.46 during the reactor-off period, and 1.29 during the reactor-on period. The nonlinear calibration significantly improves the standard deviation for spectral lines in the high energy range. Because the reactor-off background is a 74 days average spectrum, the  $\chi^2$  per degree of freedom for the reactor-off period is dominated by better statistical error without consideration to systematic errors. Temperature variations during this period, and the complex line shape for each spectral line causes systematic error, not taken into account in the  $\chi^2$ . It was desired to keep each lines importance related to its statistics, making the measured  $\chi^2$  acceptable. The nonlinear calibration coefficients,  $a_{back}$ ,  $b_{back}$ , and  $c_{back}$ , will be used for further background corrections to the spectral data.

## 5.2 Energy Calibration of $^{54}\text{Mn}$ $\gamma$ -Spectra

The  $^{54}\text{Mn}$  source spectra need to be converted from channel number to an energy scale so that the background energy scale can be matched to it, and subtracted. The high rate of the  $^{54}\text{Mn}$  source overwhelms all the background lines except for the high energy  $^{208}\text{Tl}$  line. For this reasons, a new set of calibration lines is required. The calibration lines are limited to 5-lines, the Indium atomic K-edge, the Backscattered Compton peak, the Compton edge peak, the  $^{54}\text{Mn}$  photopeak as well as the  $^{208}\text{Tl}$ , as shown in Figure 5.3. The pile-up lines above the photopeak cannot be used

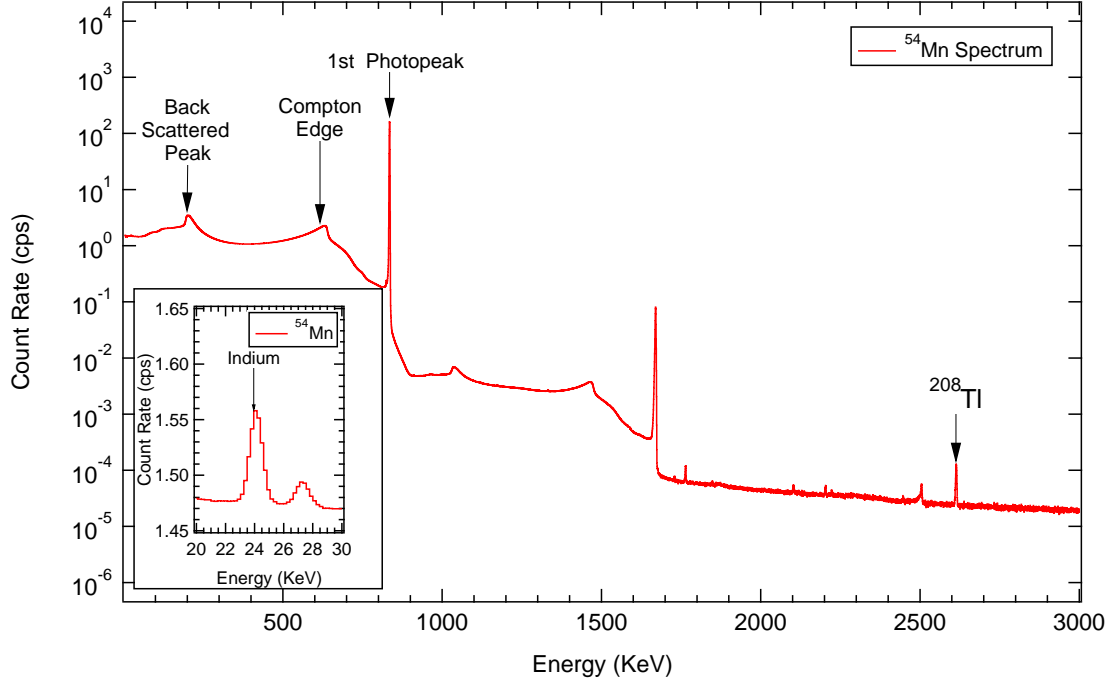


Figure 5.3. Logarithm scale of the  $^{54}\text{Mn}$   $\gamma$ -spectrum at HFIR. Indium atomic K-edge, Backscattered peak, Compton edge peak,  $^{54}\text{Mn}$  photopeak, and  $^{208}\text{Tl}$  have been used to calibrate the  $^{54}\text{Mn}$  spectra

because their precise energy is unknown. Each daily  $^{54}\text{Mn}$  spectrum is individually calibrated. The data is fit using a Gaussian distribution function which represents the complete energy deposition by the incident photon, and a second-order polynomial which represents the background spectrum,

$$f(x) = a + bx + cx^2 + \frac{A}{\sqrt{2\pi}\sigma} \exp\left(\frac{-(x - x_0)^2}{2\sigma^2}\right) \quad (5.4)$$

where  $a$ ,  $b$ , and  $c$  are the coefficients of the continuous background,  $A$  is the total count rate under the Gaussian distribution. The fit weighting of each channel is given by Poisson counting statistics. The centroid ( $x_0$ ), and energy resolution ( $\sigma$ ) are also obtained from this fitting. The energy for the  $^{54}\text{Mn}$  photopeak, and  $^{208}\text{Tl}$  are from the NNDC[60]. The energy of the Indium K-edge line is from X-ray Transition Energy

Database, Physical measurement, Laboratory, NIST[61].

The nonlinear energy calibration requires three parameters, and only three lines are usable in the  $^{54}\text{Mn}$  spectrum. This results in an unacceptable zero degree of freedom fit to the spectrum. For this reason, the Backscattered peak, and Compton edge peak were studied for this calibration. The Compton edge, and the Backscattered peak are due to incomplete absorption of the full energy of the incoming  $\gamma$ -ray. In Compton scattering, the gamma photon interacts with the electrons as if they were free or unbound. The Compton shift in energy at an angle  $\theta$  is given by

$$E_{\gamma'} = \frac{E_{\gamma}}{1 + \frac{E_{\gamma}}{m_0 c^2}(1 - \cos \theta)} \quad (5.5)$$

As the incident photons are scattered, the Compton scattered electrons have a continuous distribution of energy from zero in the forward direction to a maximum when the photon is Backscattered. The Backscattered peak is due to  $^{54}\text{Mn}$  photons which first interact by a single Compton scattering with the shielding material surrounding the detector. The energy of the Backscattered photon ( $\theta = 180^\circ$ ) is

$$E_b = \frac{E_{\gamma}}{1 + 2\frac{E_{\gamma}}{m_0 c^2}} \quad (5.6)$$

The Compton edge is the maximum energy of an electron from a single Compton scattering within the detector,

$$\begin{aligned} E_{edge} &= E_{\gamma} - E_b \\ &= E_{\gamma} \left( 1 - \frac{1}{1 + 2\frac{E_{\gamma}}{m_0 c^2}} \right) \end{aligned} \quad (5.7)$$

Based on the  $^{54}\text{Mn}$  photopeak energy 834.848 KeV, the predicted Backscattered energy is  $\sim 195.629$  KeV. The predicted Compton edge peak is  $\sim 639.220$  KeV. Table 5.3

Table 5.3.

Accepted energy, and uncertainty of the calibration lines for the  $^{54}\text{Mn}$  spectrum. The accepted energy, and uncertainty of Indium Atomic K-edge is from X-ray Transition Energy Database, NIST[61]. The accepted energy, and uncertainty of  $^{54}\text{Mn}$  photopeak, and  $^{208}\text{Tl}$   $\gamma$ -line are from NNDC[60]. The accepted energy of the Backscattered Peak, and Compton peaks are based on calculation in this Section. The estimated uncertainty of the Backscattered Peak, and Compton peaks are taken from the range of centroid values found by varying the fitting range.

Type of Spectral Lines	Accepted Energy (KeV)
Indium Atomic K-edge	$24.002 \pm 0.017$
Backscattered Peak	$195.628 \pm 0.112$
Compton Edge Peak	$639.221 \pm 0.225$
$^{54}\text{Mn}$ Photopeak	$834.848 \pm 0.003$
$^{208}\text{Tl}$ $\gamma$ -Line	$2614.511 \pm 0.115$

summarize the accepted energy, and uncertainty of each line in  $^{54}\text{Mn}$  spectrum.

The difficulty associated with these of Backscattered, and Compton edge peaks for energy calibration is to determine the centroid of those two peaks. To find the location of these peaks, a differential technique is used. The differential spectrum is give by

$$D_i = N_{i+1} - N_i \quad (5.8)$$

where  $N_i$  is the counts in the  $i$ th channel in the  $^{54}\text{Mn}$  spectra. Figure 5.4 shows the differential peaks of the Backscattered as well as Compton Edge Peak. After obtaining the centroids from the differential spectra for the Compton, and Backscattered peaks, a nonlinear function was used to calibrate the  $^{54}\text{Mn}$  daily spectrum

$$E_i^{Source} = a_r + b_r \times i + c_r \times i^2 \quad (5.9)$$

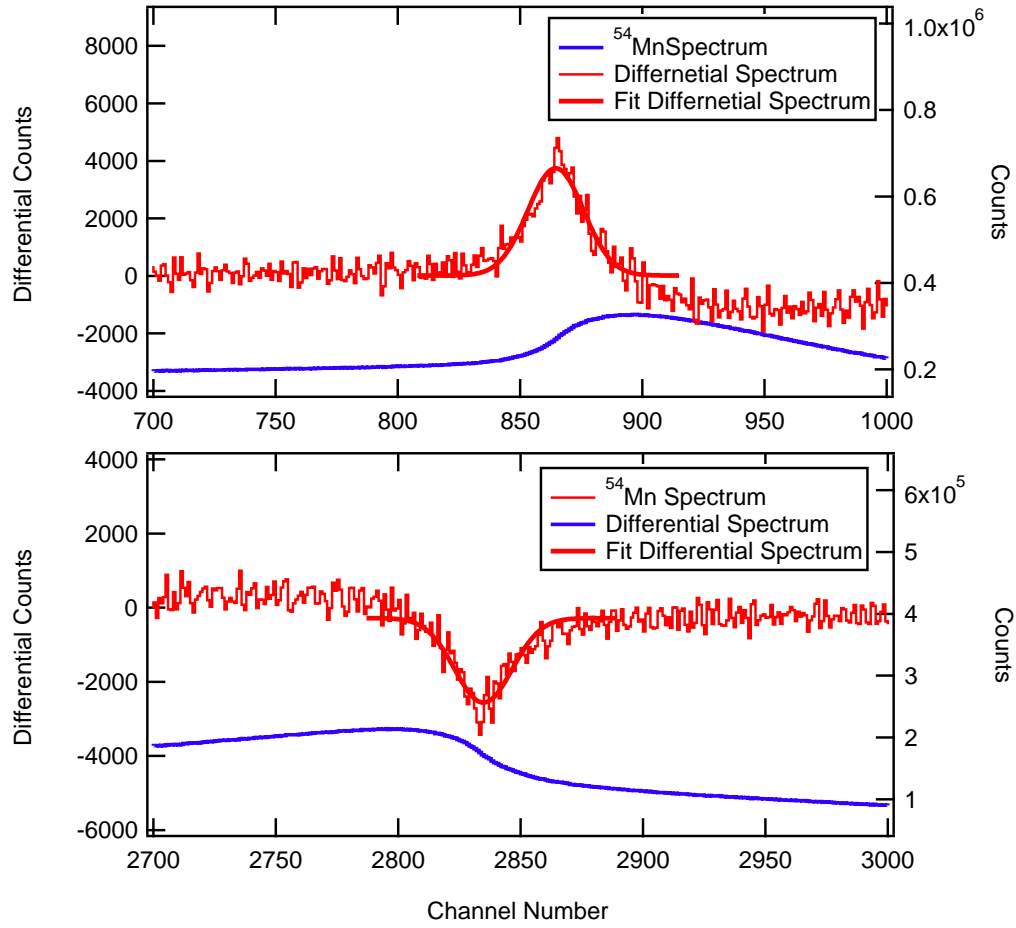


Figure 5.4. Differential Backscattered, and Compton Edges peaks from <sup>54</sup>Mn daily spectra at HFIR.

where  $a_r$ ,  $b_r$ , and  $c_r$  are the coefficient of the nonlinear calibration.  $r$  represents the <sup>54</sup>Mn spectrum of  $r$ th day. Unfortunately, the residuals for the Backscattered, and Compton Edge peaks were found to be unacceptable; causing unacceptable calibrations. The exact centroid value for the Backscattered, and the Compton Edge peaks depend on the source, detector, and shielding geometry. For this reason, the peak centroids of those peaks do not match the predicted energy of the Backscattered, and Compton edge peaks. In order to assign the correct centroid value of those peaks,

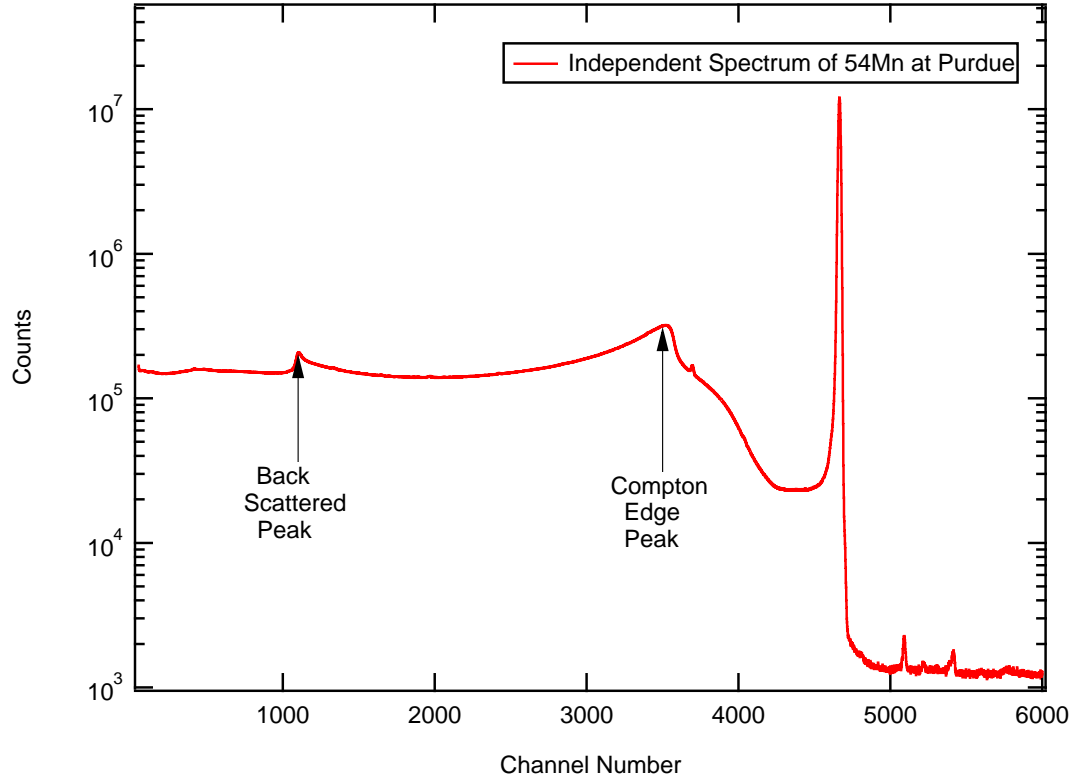


Figure 5.5. Independent  $^{54}\text{Mn}$  spectrum measured in the Physics Building at Purdue University used to study systematic shift.

the shift of the Backscattered ( $\delta E_{Back}$ ), and the Compton Edge ( $\delta E_{Compton}$ ) peaks are described as

$$E_{Back} + \delta E_{Back} + E_{Compton} + \delta E_{Compton} = E_{photopeak} \quad (5.10)$$

Because the sum of  $E_{Back}$ , and  $E_{Compton}$  is  $E_{photopeak}$ , based on the Eq.5.7, Eq. 5.10 can be simplified into

$$\delta E_{Back} = -\delta E_{Compton} \quad (5.11)$$

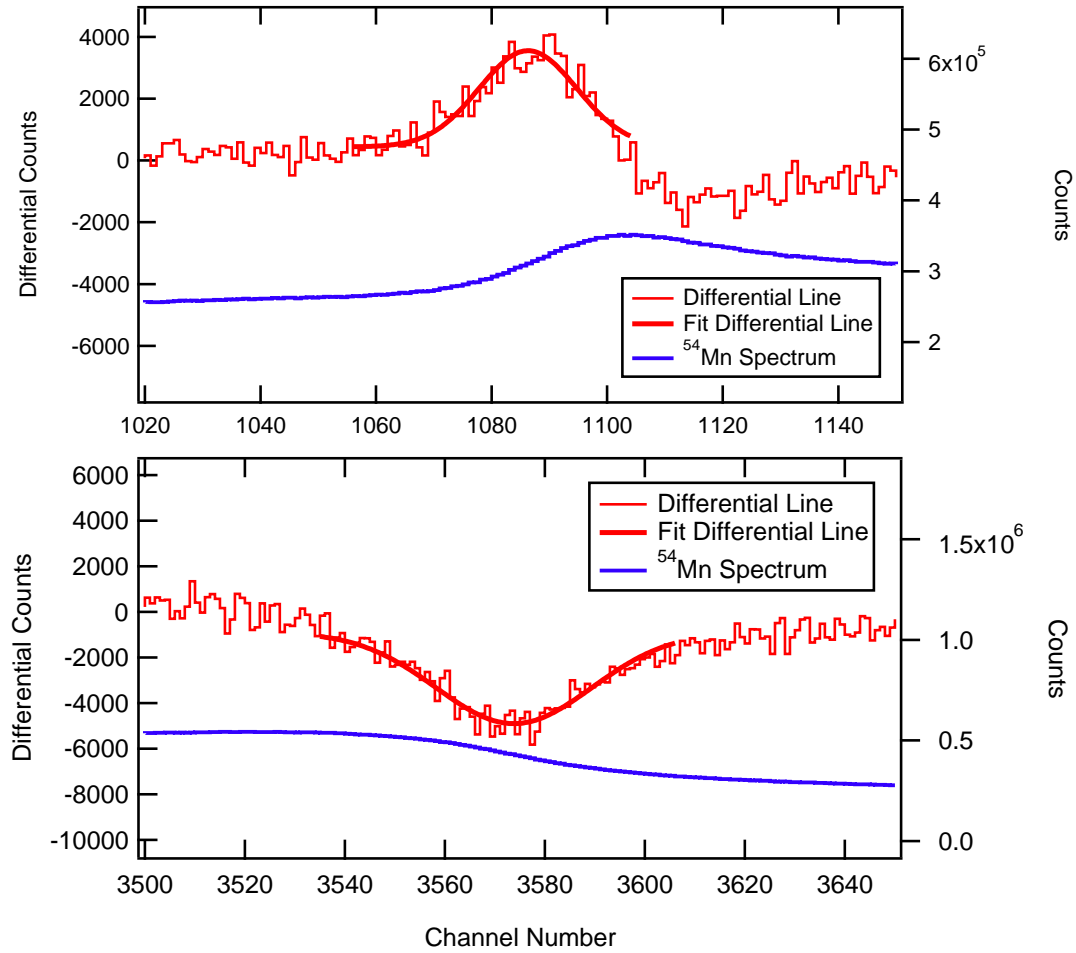


Figure 5.6. Differential Backscattered, and Compton Edges peaks from an independent measurement of the  $^{54}\text{Mn}$  daily spectrum made in the Physics Building at Purdue University to study the energy peak shift.

Eq. 5.11 shows the shift of the Backscattered Compton peak, and Compton edge peaks are equal, but of opposite sign.

$|\delta E|$  is found by taking the average shift from the nonlinear fit required to place the two differential peaks on to the fit. Only the residuals from the 1st day of the  $^{54}\text{Mn}$  data taking, the statistically most significant data, were used to calculate the



shift for all the experimental spectra. The shifted value of the Backscattered, and Compton edge peak for the HFIR data is measured to be  $\sim 0.2235$  KeV ( $\sim 1$  bin) with each peaks shifting in the opposite direction.

To verify this analysis, an independent  $^{54}\text{Mn}$  spectrum was taken using a different HPGe detector with similar geometry in the Physics Building at Purdue University. The results are shown in Figure 5.5. Figure 5.6 shows the Backscattered peak, Compton Edge peak, and their differential peaks from this measurement. Again, a nonlinear calibration was used, and the fit residuals of the Backscattered, and Compton Edge peaks from the independent spectrum were found to have the same value but with opposite sign, verifying Eq. 5.11. This method was used to optimize the calibration precision for every daily spectrum using only the first day's spectrum to find the centroid's shift value.

## Discussion of Calibration Coefficients

The results of the fitting are shown in Figure 5.7. Again, the calibration coefficient  $a_r$ ,  $b_r$ , and  $c_r$  are shown as a function of time found using the shifted centroids method.

### Constant Terms $a_r$

The constant terms  $a_r$  vary about zero with a variance of  $\sim 0.02$  KeV or less than 10% of a single bins width at 0.225 KeV. The  $a_r$  parameters measure offsets in the energy scales.  $a_r$  is expected to be nearly zero in a low noise environment which is the case in this experiment. The stability of  $a_r$  yields a stable Region of Interest continuing the  $^{54}\text{Mn}$  photopeak.

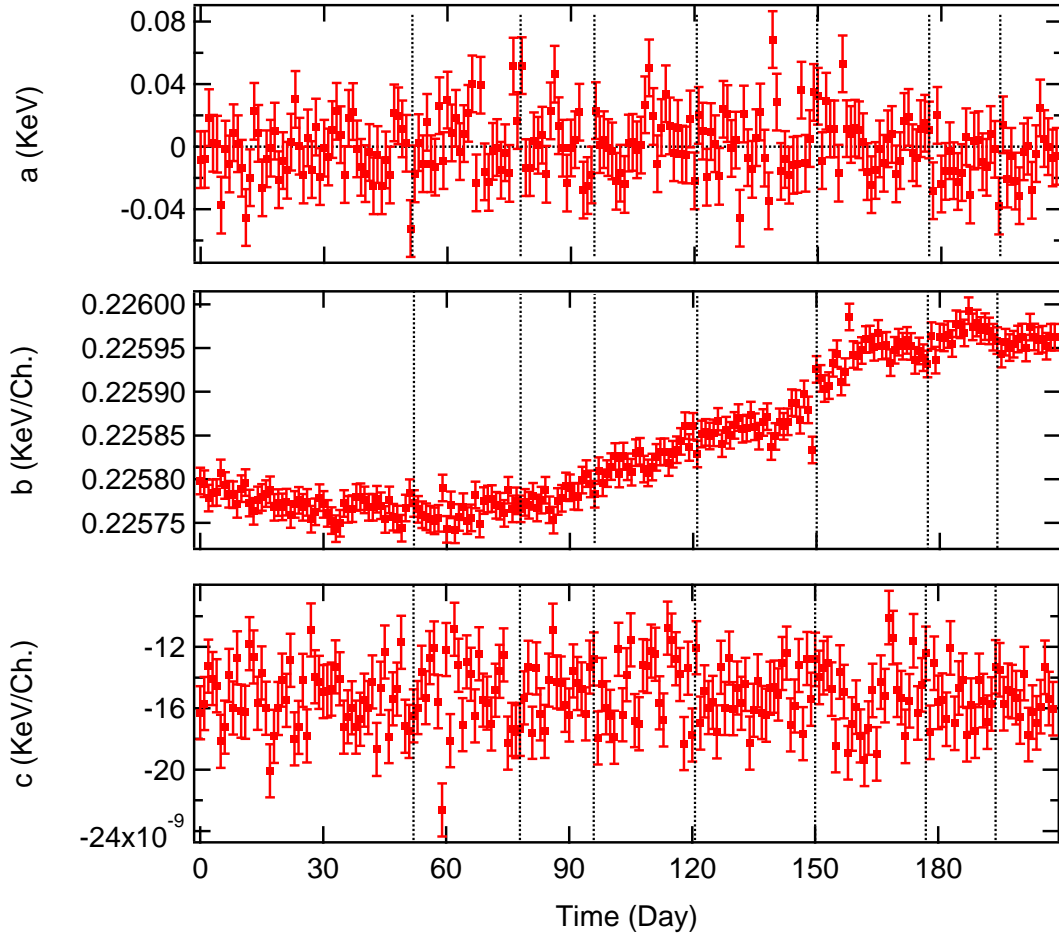


Figure 5.7. Nonlinear energy calibration parameters,  $a_r$ ,  $b_r$ , and  $c_r$ , determined for each of the daily  $^{54}\text{Mn}$  spectra.

### Linear Terms $b_r$

The linear parameter is well measured with an accuracy of  $\delta b/b \sim 7 \times 10^{-5}$ . Nonetheless, the  $b_r$  vary over the course of the experiment due to temperature variations driven by the X-cooler responding to variation in the humidity. To show this, the linear  $b_r$  parameters are fit to a periodic function,

$$b(t) = b_0 + A \sin(\omega t + \phi) \quad (5.12)$$

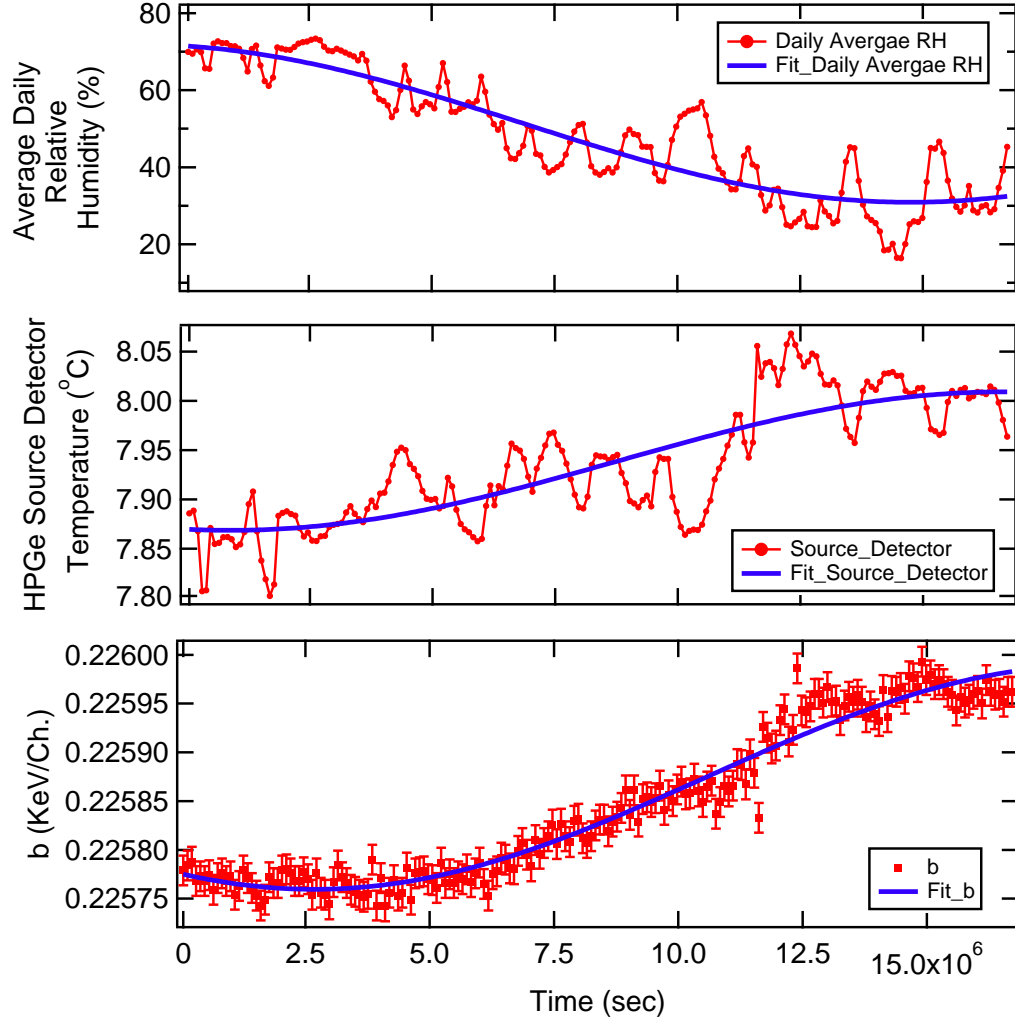


Figure 5.8. Daily averages for the humidity, temperature of the HPGe source detector, and the linear term  $b_r$ . Each is fitted with a periodic function fixed at 1 year, as a function of time.

in which  $\omega$  is fixed at 1-year. The resulting excellent fit,  $\chi^2/Dof = 1.14$ , is displayed in Figure 5.8, and the phase in Table 5.4.

Likewise, the detector temperature is fit as a function of time, with the fit shown in Figure 5.8, and Table 5.4. It should be noted that the magnetude of  $b_r$  is directly related to the detectors band gap which has a temperature dependence given

Table 5.4.

The yearly cycling of the humidity, temperature for the HPGe source detector, and linear term  $b$  values relative to the experiments starting date.

Fixed $\omega=1$ year	Negative phase ( $\phi$ )
Out of phase humidity	$103 \pm 1$ day
Source detector temperature	$101 \pm 6$ day
Linear term $b$	$122 \pm 2$ day

by Varshni's empirical form[62]. Varshni's form predicts that lower temperatures produce larger band gaps, and vice versa. Since lower  $b_r$  values represent larger band gaps,  $b$ , and the detector temperature should be in phase. As shown in Table 5.4, the phases are in reasonable agreement.

However, the temperature of the housing enclosure is held at a very stable temperature  $10.00 \pm 0.027^\circ\text{C}$ . Nonetheless, the detectors X-cooler is outside the housing. The X-cooler is affected by the humidity in the following manner, as the humidity increases the heat capacity of the air increases, allowing more efficiently cooling, lowering the temperature of the detector, and thus increasing the band gap. Likewise, as the humidity decreases, the heat capacity decreases, yielding less efficient cooling, and allowing the detector temperature to increase, narrowing the band gap. In this way, the humidity variation should be out of phase with the detector temperature, and  $b_r$  parameters as is the case shown in Figure 5.8, and Table 5.4, using the same fixed fit. While these effects are a small, they produce yearly oscillations in the data at the level of  $10^{-3}$ .

### Nonlinear Terms $c_r$

The  $c_r$  parameter is the nonlinear term, significant only for high energy spectral lines. It is due to temperature variations of the electronic outside the temperature

controlled housing specifically the DSPEC-50 spectrometer. While in the plot  $c_r$  appears stable, and small, at large channel number, for example,  $\sim 4000$  where the  $^{54}\text{Mn}$  photopeak is located, it accounts for a shifted of 1 full bin (0.225 KeV) in the spectrum. The  $c_r$  uncertainty is  $\delta c_r/c_r \sim 0.1$ , and requires further refinement. Higher accuracy in this parameter will be obtained using a "Side Band" analysis techniques as will be discussed later.

Finally, the result of the daily energy calibration shows, in Figure 5.9 the stability of the  $^{54}\text{Mn}$  photopeak using these calibration techniques. The average energy of the  $^{54}\text{Mn}$  photopeak is  $834.849 \pm 0.001$  KeV. The energy peak is exceptionally stable, and is within the uncertainty of the  $^{54}\text{Mn}$  standard error value  $\pm 0.003$  KeV[60]. The nonlinear calibration plays a critical role in the stability of the Region of Interest region, and the ability to make further accurate corrections to the spectrum.

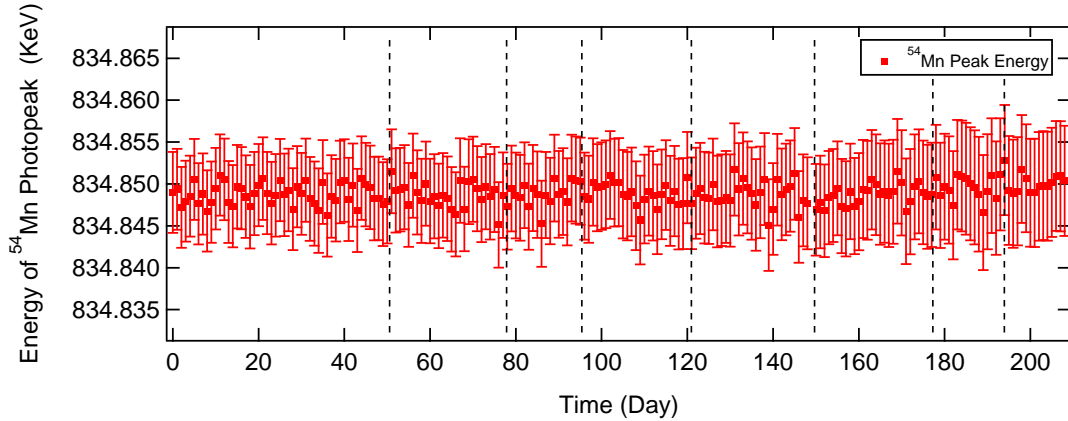


Figure 5.9. Energy of the  $^{54}\text{Mn}$  primary photopeak as a function of time. The average energy of  $^{54}\text{Mn}$  is  $834.849 \pm 0.001$  KeV which shows stability after the nonlinear calibration.



## 6. Corrections to the $^{54}\text{Mn}$ Source, and Background Spectra

The  $^{54}\text{Mn}$   $\gamma$  spectra were collected from August 14, 2015, at 23:58:22 to March 09, 2016 at 23:12:51 which includes four reactor-off, and four reactor-on periods. The total running period consisted of 95 reactor-on days, and 114 reactor-off days over 209 days of data collection. The data was collected using a 60% HPGe detector. The initial rate was 8.01 kcps with a dead time of  $\sim 13\%$ . The ending data rate was 5.05 kcps with a dead time of  $\sim 8\%$ .

Because the analysis of the HPGe spectrum requires mathematical manipulate on each channel, statistical, and systematic error must be considered channel by channel. Systematic error by definition is an error that causes a shift of the measurement away from its real value due to effects that are not entirely under the control of the experimenter. Thus, systematic error analysis requires a theory of its cause. There are three significant systematic errors associated with the measurement. (1) The Electronic Dead Time from the DSPEC-50 electronic spectrometer (2) Neutron, and natural background radiation cause an unwanted background spectrum (3) The Electronic pile-up due to the inability of the electronics spectrometer to distinguish two or more pulses occurring within a time window smaller than the electronics resolving time.

Correction procedures for obtaining the true count rate in the  $^{54}\text{Mn}$  *Region of Interest (ROI)* are summarized in Figure 6.1.

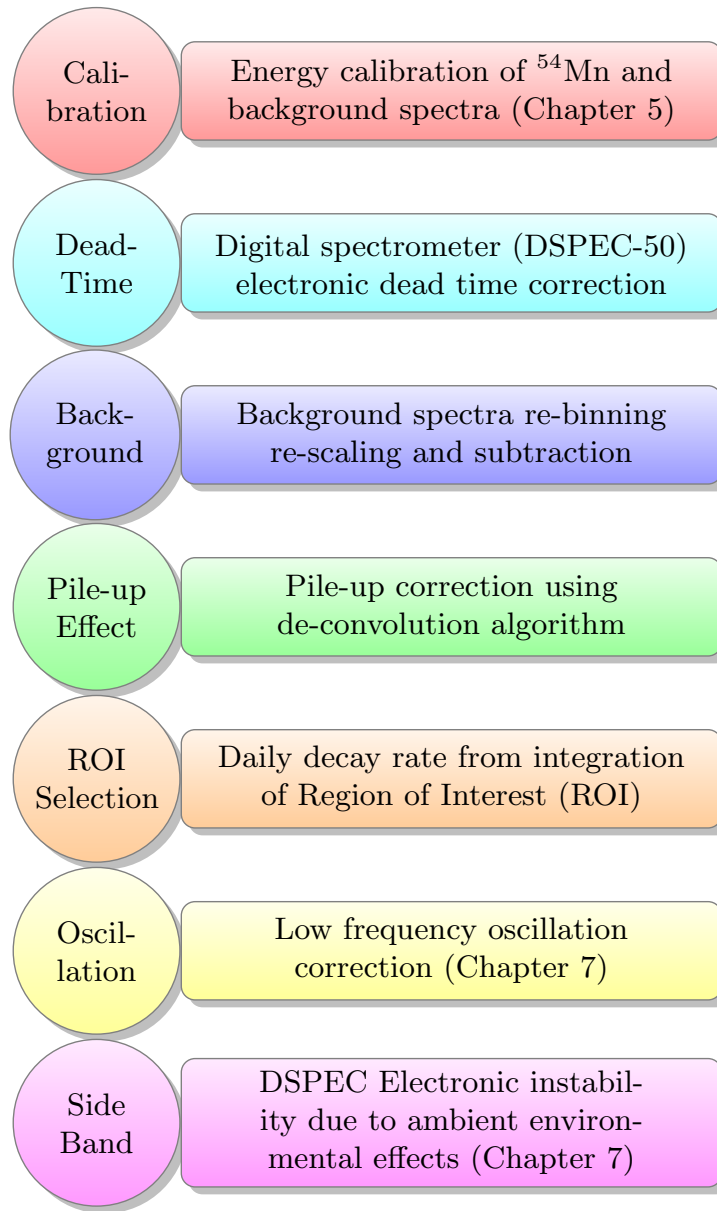


Figure 6.1. Correction procedure flow for obtaining the true  $^{54}\text{Mn}$  ROI count rate.

### 6.1 Electronic Dead Time Correction

Dead time is the integration of these periods in which the electronics do not give a response to detector pulses. The electronic spectrometer follows the non-paralyzable



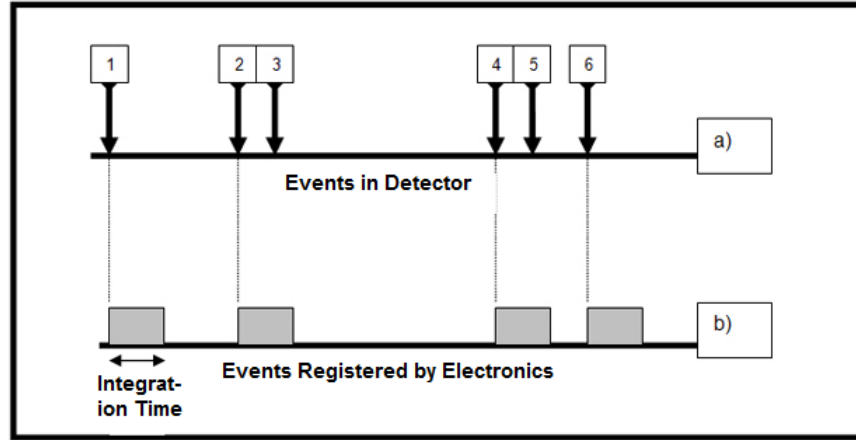


Figure 6.2. Illustration of electronic dead time from the DSPEC-50 spectrometer.

model as illustrated in Figure 6.2[63]. In this example, events 3, and 5 are not registered by the electronics because they come after the previous event before the pulse returns to the electronic baseline[64]. The ORTEC DSPEC-50 spectrometer is designed[64]

*"To optimally process an input pulse stream, and thereby obtain the best spectral resolution. (For this reason), the signal processing device..... (allows) the input signal to return to baseline before beginning to process the subsequent pulse.*

For this design approach[64],

*"The dead time for a conventionally processed pulse is the sum of the pulses rise time, flattop, and fall time."*

The DSPEC-50 has two different ways it processes the 2nd incoming pulse from the HPGe detector if the previous pulse has not returned to baseline. First, DSPEC-50 will reject the 2nd pulse if it is recognized. Second, if the 2nd pulse arrives unrecognized, that is within a shorter time than the electronic resolving time, the DSPEC-50 records the sum of two pulses which is called electronic pile-up. The dead time cor-

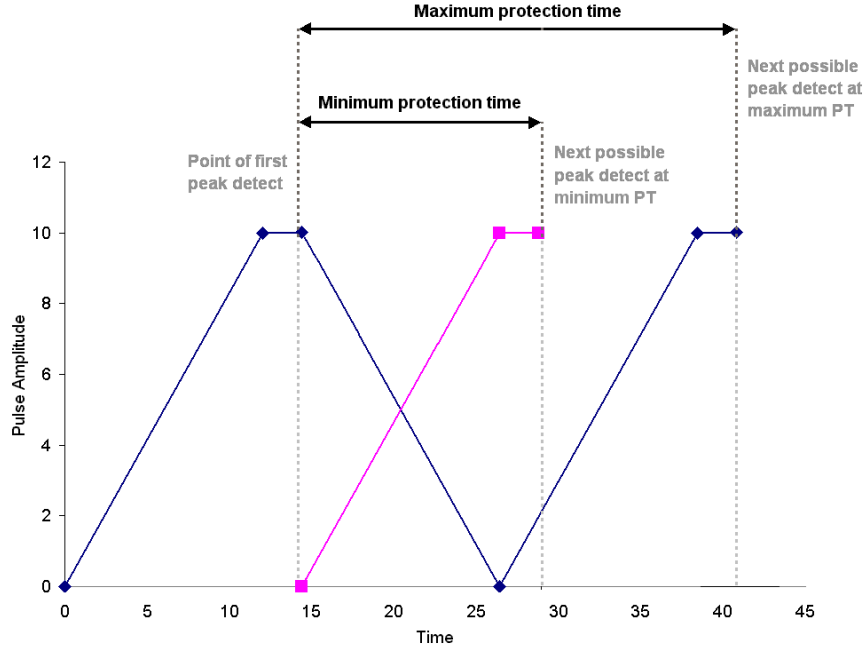


Figure 6.3. DSPEC-50's Minimum, and Maximum Protection Times[64]. At the maximum protection-time setting, the DSPEC-50 processes pulses in a conventional way. That is the dead time is the sum of the pulses rise time, flattop, and fall time. The dead time of an incoming pulse is nearly  $\sim 16 \mu\text{sec}$  for the HFIR experiment.

rection would be correct for the full spectrum if there were no electronic pile-up effect.

There are two types of pile-up effects, low energy, and high energy pile-up, defined with respect to the ROI region. The DSPEC-50 dead time correction is only correct when applied to the photopeak counts. However, the analysis uses an ROI not limited to the photopeak. The dead time correction does correctly account for the high energy pile-up, that is the loss of events out of the ROI region. However, the dead time correction does not take into account the lower energy pile-up effect. That is low energy events combining to an energy that places the combined event into the photopeak Region of Interest. Triple pile-up is also observed at the level of  $10^{-6}$  of

Table 6.1.

Properties of the full  $^{54}\text{Mn}$  spectrum. The 1st day spectrum is in a reactor-off period. The last day of the spectrum is in a reactor-on period.

Full Spectrum Daily Ratio	First Day (Reactor-off)	Last Day (Reactor-on)
Spectrum rate (cps)	8009.5	5054.5
Background rate (Fractional rate) (cps)	3.1(0.04%)	4.7 (0.09%)
Pile-up rate (cps)	33.5 (0.4%)	13.7 (0.04%)
Dead time for a day (sec)	11166.4	7235.9
Pulse generated dead time ( $\mu\text{sec}$ )	16	16
Double pulse time resolution ( $\mu\text{sec}$ )	0.5	0.5
Dead time rate for background rate (cps)	0.013	0.012

the photopeak rate, and is neglected in this analysis.

Table 6.1 gives the properties of the  $^{54}\text{Mn}$  spectrum using the corrections. While it may appear optimal to finalize the dead time corrections before moving on to other corrections, this is not possible. The pile-up correction is entangled with other corrections as will be shown later. The dead time correction is accurate to  $10^{-3}$  if pile-up is not taken into account. The pile-up correction can be untangled by first noting in Table 6.1 that the full spectrum background pile-up with the source is only 0.013 cps, calculated using the double pulse time resolution  $0.5 \mu\text{sec}$ . This, of course, is much smaller in the Region of Interest. For this reason, the background-source pile-up is negligible allowing the background to be first subtracted from the dead time corrected source spectrum.

## 6.2 Background Spectrum Correction

Before background subtraction can proceed, it must be noted the  $^{54}\text{Mn}$  source spectra, and background spectra have been calibrated using different nonlinear calibrations. As with this, and other corrections, the  $^{54}\text{Mn}$  spectrum is never energy

scale altered during correction. Corrections are always energy matched to the  $^{54}\text{Mn}$  calibration. In this way, the correction contributes to the minimum possible error to the analysis. For this reason, the background correction is a three-step process. (1) The dead time correction is made channel by channel. (2) The second step requires energy rescaling of the background data to match the difference in energy calibration parameters between the  $^{54}\text{Mn}$  data, and the background data. (3) The third step is to adjust for the difference in the background rate between the  $^{54}\text{Mn}$  data, and the collected background data. The collected background is normalized to the daily rate above the triple  $^{54}\text{Mn}$  pile-up of the photopeak, in the range  $E_{low} = 2515$  to  $E_{high} = 3680$  KeV, using a single scaling parameter. This region has no pile-up effects. The total number of counts must match in the  $^{54}\text{Mn}$  source, and background histograms in this comparison region. After completing all the correction to the background, the resulting background spectrum is subtracted from the  $^{54}\text{Mn}$  source spectrum.

### 6.2.1 Technical Process for Dead Time Correction

The dead time correction is made channel by channel each day, requiring the timing errors reported out by the DSPEC-50 to be included for each channel calculation. The channel by channel correction must be made as other corrections require channel by channel accounting. The  $^{54}\text{Mn}$  spectrum from the DSPEC-50 includes 16384 channels. The channel by channel correction is accomplished as follows. First, the rate in each channel of the spectrum is found

$$R_i = \frac{N_i}{\Delta t} \quad (6.1)$$

where  $N_i$  is the raw counts of  $i$ th channel, and  $\Delta t$  represents the live time of the spectrum. The live time is the period the detector electronics respond to the detector pulses. In another word, it is the real-time minus the dead time for each spectrum.

The variance associated with the  $i$ th channel of the spectrum is

$$\sigma_i^2 = \frac{N_i}{(\Delta t)^2} + \frac{(N_i)^2}{(\Delta t)^2} \times \frac{(\delta t)^2}{(\Delta t)^2} \quad (6.2)$$

The 1st term is from the statistical uncertainty of the Poisson distributed for the  $i$ th channel counts in the spectrum. The second term is the DSPEC-50 timing error which reports out the live times ( $\Delta t$ ) to an accuracy of 0.1 sec. The timing error is a uniform squared distribution, yielding a variance of  $\delta t = 0.1 \text{ sec}/\sqrt{12} = 0.029 \text{ secs}$ . The dominate error in the HPGe spectrum is the statistical error. The timing error from the DSPEC-50 is at the level of  $10^{-7}$ , and it is negligible but tracked in the total error estimation.

### 6.2.2 Background Spectrum Energy Rescaling

The 2nd step in the energy rescaling process is to assign the energy value associated with a background spectrum bin to a location within the  $^{54}\text{Mn}$  bin taking into account the different calibration values of the  $^{54}\text{Mn}$  source, and background spectra. During calibration, each gamma-ray line is fit using channel number which is an integer. The fitting program assigns an integer value channel number bin ( $i$ ) to an integer number of counts ( $N_i$ ) associated with that bin ( $i$ ). Thus, each pair  $[B(i), N(i)]$  is what the fitting programs operate on. The assumption is that  $N(i)$  is associated with the central value of the bin. That is  $B(i)$ , and  $N(i)$  are located at the center of the bin.

The energy calibration of each daily spectrum

$$E_r^{Source}(i) = a_r + b_r \times i + c_r \times i^2 \quad (6.3)$$

where  $r$  is the run number, and  $i$  represents the index for each bin for the  $^{54}\text{Mn}$  source spectrum.  $a_r$ ,  $b_r$ , and  $c_r$  is the daily calibration coefficient which is shown in

Figure 5.7. Likewise, the reactor-on, and reactor-off background data were calibrated using the spectral lines shown in Table 5.1. These yield two calibrations,

$$\begin{aligned} E_{off}^{back}(j) &= a_{off}^{back} + b_{off}^{back} \times j + c_{off}^{back} \times j^2 \\ E_{on}^{back}(j) &= a_{on}^{back} + b_{on}^{back} \times j + c_{on}^{back} \times j^2 \end{aligned} \quad (6.4)$$

where  $j$  represents the index for each bin for each background spectrum.  $a_{off}^{back}$ ,  $b_{off}^{back}$ , and  $c_{off}^{back}$  are the calibration coefficients of reactor-off background spectrum, and  $a_{on}^{back}$ ,  $b_{on}^{back}$ , and  $c_{on}^{back}$  are the calibration coefficients of reactor-on background spectrum, as shown in Table 5.2. Because both the  $^{54}\text{Mn}$ , and the background spectra have nonlinear calibrations, it is convenient to use the calculated energy scale directly in the energy rescaling process. The background spectra were re-scaled to match the energy scaling in each  $^{54}\text{Mn}$  spectrum. The new background value  $V_i^*$  is the estimated background associated with the  $i$ th bin in the  $^{54}\text{Mn}$  source data histogram, that is

$$\begin{aligned} V_{background}^*(i) &= \frac{E_r^{source}(i+1) - E^{back}(j)}{E^{back}(j+1) - E^{back}(j)} \times V^{back}(j) \\ &\quad + \frac{E^{back}(j+1) - E_r^{source}(i+1)}{E^{back}(j+2) - E^{back}(j+1)} \times V^{back}(j+1) \end{aligned} \quad (6.5)$$

where  $V^{back}(j)$ , and  $V^{back}(j+1)$  are the original background values in the  $j$ , and  $(j+1)$  background spectrum bins. If the  $^{54}\text{Mn}$  source spectrum was collected in the reactor-off period, the  $E^{back}(j)$ , and  $V^{back}(j)$  will be  $E_{off}^{back}(j)$ , and  $V_{off}^{back}(j)$  for the  $j$  index of the reactor-off background spectrum. Similarly, if the  $^{54}\text{Mn}$  source spectrum was collected in the reactor-on period, the  $E^{back}(j)$ , and  $V^{back}(j)$  will be  $E_{on}^{back}(j)$ , and  $V_{on}^{back}(j)$  for  $j$  index of the reactor-on background spectrum. The new uncertainty value  $\sigma^*(i)$  in the estimated background associated with the  $i$ th bin in the source data histogram

$$\begin{aligned} (\sigma_{background}^*(i))^2 &= \left( \frac{E_r^{source}(i+1) - E^{back}(j)}{E^{back}(j+1) - E^{back}(j)} \right)^2 \times (\sigma^{back}(j))^2 \\ &\quad + \left( \frac{E^{back}(j+1) - E_r^{source}(i+1)}{E^{back}(j+2) - E^{back}(j+1)} \right)^2 \times (\sigma^{back}(j+1))^2 \end{aligned} \quad (6.6)$$

where  $\sigma^{back}(j)$ , and  $\sigma^{back}(j+1)$  are the original background values in  $j$ , and  $(j+1)$  bins. After the energy rescaling process for the reactor-on, and the reactor-off background spectra, the background, and  $^{54}\text{Mn}$  source spectral histograms have been aligned. No additional error is assigned to the energy rescaling process as the number of counts is conserved. After the daily  $^{54}\text{Mn}$  source spectrum, and background spectrum are aligned, the background spectrum is ready for amplitude rescaling.

### 6.2.3 Background Spectrum Amplitude Rescaling

To re-scale the background amplitude, the  $^{54}\text{Mn}$  spectrum, and the reactor-on or reactor-off background spectrum is summed above the third photopeak for comparison. Because the comparison region is above the triple pile-up of the photopeak, the  $^{54}\text{Mn}$  source contributes negligibly to counts within this region. Thus, the summation of the rate in this region represents the background rate during the 24-hour measurement.

The  $^{54}\text{Mn}$  calibration parameters vary day to day for each spectrum. For this reason, the edge of the energy band of the comparison region can fall between the bin boundaries. The low, and high comparison band boundary have been set to  $E_{low} = 2515$  keV, and  $E_{high} = 3680$  keV above the 3rd photopeak which contains only background. The bin integration extends from

$$\begin{aligned} k_{low} &= \frac{-b_r + \sqrt{b_r^2 - 4c_r(a_r - E_{low})}}{2c_r} \\ k_{high} &= \frac{-b_r + \sqrt{b_r^2 - 4c_r(a_r - E_{high})}}{2c_r} \end{aligned} \tag{6.7}$$

where  $k$  is not an integer number in the above equations. It must be remembered that integer values of  $k$  represent the bin center. The fractional part of the first bin to be summed, and the sum start index is determined by

$$V_{\text{Fraction}}^{\text{Start}} = (1 - F[k_{\text{low}}]) \times V_{I[k_{\text{low}}]}^* \quad (6.8)$$

where  $F$  is a fraction that takes the fractional part of the number, and  $I$  is a fraction that takes the integer part of the number. The fractional part of the last bin, and the sum end index is determined from,

$$V_{\text{Fraction}}^{\text{End}} = F[k_{\text{high}}] \times V_{I[k_{\text{high}}]}^*. \quad (6.9)$$

From these evaluations the total rate sum,  $S$  is then found

$$S = V_{\text{Fraction}}^{\text{Start}} + \sum_{k=I[k_{\text{low}}]+1}^{I[k_{\text{high}}]} V(k) + V_{\text{Fraction}}^{\text{End}}. \quad (6.10)$$

Notice that the start, and end indices need to be calculated for every days run as the calibration coefficients vary each day. Because no counts have been lost during this process, the statistical error associated with the sum is  $\sim \sqrt{S}$ . The other contributions to the error, such as the dead time corrections have already been taken into account before this calculation. Because the error associated with this correction is so much smaller than the errors already calculated for each bin in the  $^{54}\text{Mn}$  spectrum, no error will be assigned to this correction.

The amplitude of the background spectra is shifted to match the estimated background found in the  $^{54}\text{Mn}$  spectrum by comparing the energy region above the 3-event pileup photopeak with the background data observed in that same region. Every bin of the background spectrum is scaled by

$$V(i)_{\text{background}}^{**} = \frac{S_{\text{source}}}{S_{\text{background}}} V^*(i)_{\text{background}}, \quad (6.11)$$



and the associated error is simply scaled

$$\sigma(i)_{background}^{**} = \frac{S_{source}}{S_{background}} \sigma^*(i)_{background} \quad (6.12)$$

As has been stated the parameters, and binning of the collected  $^{54}\text{Mn}$  source spectra are not altered in this process. All background spectra subtractions to the  $^{54}\text{Mn}$  source data sets are accomplished by altering the parameters, and binning of the near zero error of the background data set.

#### 6.2.4 Background Spectrum Subtraction

After completion of the energy rescaling, and amplitude rescaling for background spectrum, the resulting background spectrum can be subtracted from the  $^{54}\text{Mn}$  source spectrum. Figure 6.4 compares the 1st day of the  $^{54}\text{Mn}$  spectrum before background correction, and the background spectrum after the matching correction. The process is channel by channel (bin by bin) subtraction using either the reactor-on background or reactor-off background spectra. The corrected  $V(i)_{corrected}$  at the  $i$ th bin is

$$V(i)_{corrected} = V(i)_{source} - \frac{S_{source}}{S_{background}} V^*(i)_{background} \quad (6.13)$$

where  $V(i)_{source}$  is the value at the  $i$ th bin from the  $^{54}\text{Mn}$  source spectrum.

The corrected uncertainty  $\sigma(i)_{corrected}$  for the  $i$ th bin is

$$\sigma(i)_{corrected} = \sqrt{(\sigma(i)_{source})^2 + (\sigma(i)_{amplitude})^2 + (\sigma(i)_{background}^{**})^2} \quad (6.14)$$

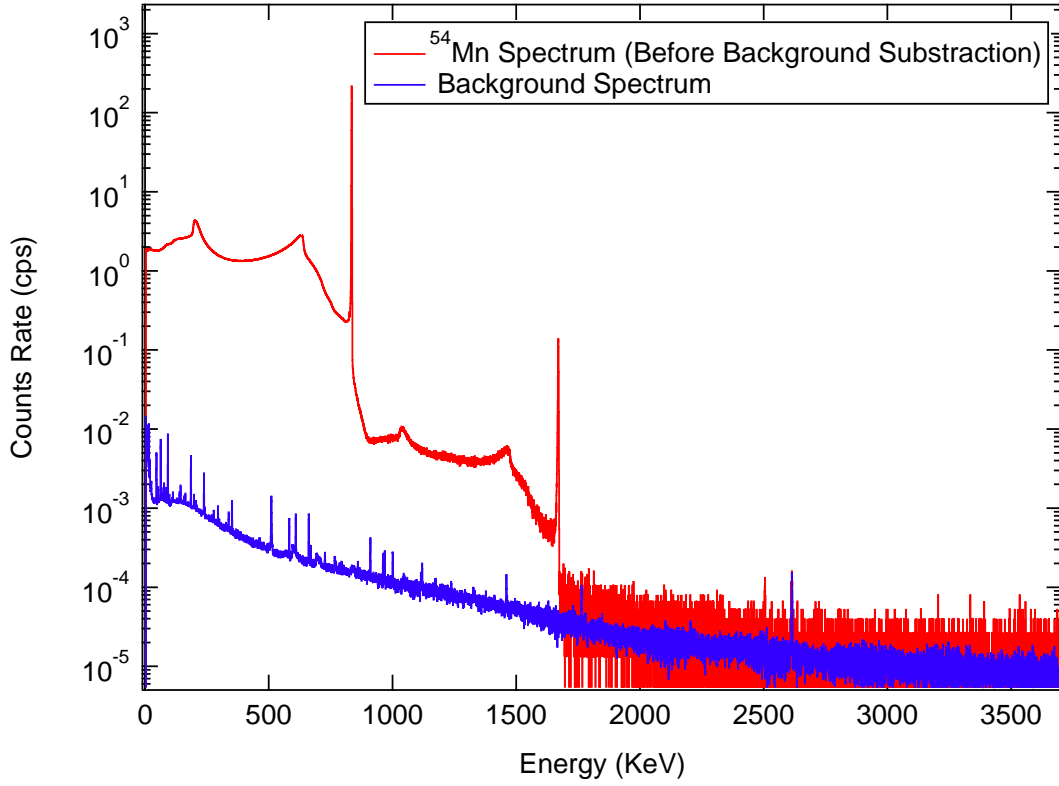


Figure 6.4. Logarithm scale of the  $^{54}\text{Mn}$   $\gamma$ -spectrum before background spectrum subtraction, and the background spectrum

where  $\sigma(i)_{\text{source}}$  is the uncertainty in the  $i$ th bin of the  $^{54}\text{Mn}$  source spectrum.  $\sigma(i)_{\text{amplitude}}$  considers the errors in  $S_{\text{background}}$ . The ratio of the  $^{54}\text{Mn}$  spectrum's error to the error caused by amplitude scaling of the background is

$$\frac{\sigma(i)_{\text{amplitude}}}{\sigma(i)_{\text{source}}} = \frac{\delta S_{\text{source}} \times V(i)_{\text{background}}^*}{S_{\text{background}} \times V(i)_{\text{source}}} \sim \left\{ \begin{array}{l} 2 \times 10^{-3} \text{ In the Compton Region} \\ 1 \times 10^{-4} \text{ In the ROI Region} \end{array} \right\} \quad (6.15)$$

where  $S_{\text{background}} \sim 0.06$  cps, and the values of  $\delta S_{\text{source}}$ ,  $V(i)_{\text{background}}^*$ , and  $V(i)_{\text{source}}$  are taken from Figure 6.4. The background  $\sigma(i)_{\text{background}}$ , and the amplitude scaling

error  $\sigma(i)_{amplitude}$  are extremely small compared to the statistical error in the  $^{54}\text{Mn}$  spectrum, and are dropped. The corrected  $\sigma(i)_{corrected}$  uncertainty in the  $i$ th bin is

$$\sigma(i)_{corrected} \sim \sigma(i)_{source} \quad (6.16)$$

Thus, the background subtraction contributes no error to the  $^{54}\text{Mn}$  spectrum.

### 6.3 Pile-up Correction by De-convolution Algorithm

With the background correction completed, the pile-up correction can be made. Figure 6.5 shows the full  $^{54}\text{Mn}$   $\gamma$ -ray spectrum after background subtraction. The  $^{54}\text{Mn}$  spectrum consists of a "Compton" region in which the full energy of the  $\gamma$ -ray was not completely absorbed. This region is labelled Region 1 in Figure 6.5. The full-energy peak or the photopeak is produced by the complete absorption of the  $\gamma$ -energy, as shown in Region 2. The ratio of events in Region 1 to Region 2 is nearly 3. One of the major systematic errors in  $^{54}\text{Mn}$  spectrum is the electronic pile-up. The pile-up, shown in Region 3, and 4, is caused by two independent nuclear decay photons which interact with the detector within a time period shorter than the resolving time of the detector. Because the primary photopeak can be treated as a  $\delta$ -function, the pile-up Region 3, and 4 appears as an integration of the "Compton" Region 1, with the photopeak, Region 2, yielding a mirror-like image of the lower energy single,  $\gamma$ -ray region, but at higher energy. Region 3, and 4 is called the first pile-up of the  $^{54}\text{Mn}$  spectrum that has the ratio of  $10^{-2}$  to the 1st photopeak. Region 5, and 6 are called the second pile-up of the  $^{54}\text{Mn}$  spectrum in which 3  $\gamma$ -rays interact with the detector in a time shorter than the resolving time. This region has a ratio to the primary photopeak of nearly  $10^{-5}$ . The expected measuring sensitivity in the experiment is to be 1 part in  $10^5$ , so the pile-up corrections play a key role to improve the measuring sensitivity.

To obtain a highly accurate single-events  $^{54}\text{Mn}$  spectrum, the piled-up events are removed through an iterative de-convolution algorithm. This procedure is per-

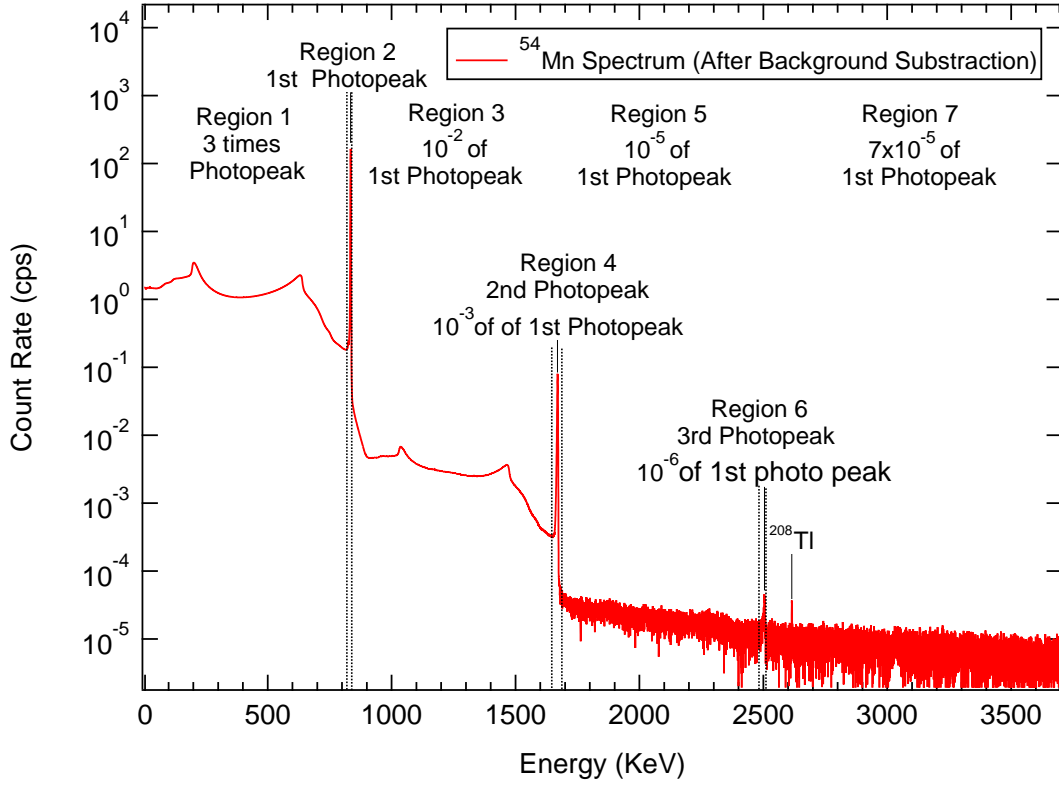


Figure 6.5. Logarithm scale of the  $^{54}\text{Mn}$   $\gamma$ -ray spectrum after background subtraction. The  $^{54}\text{Mn}$  photopeak is at 834.848 KeV. The second coincident photopeak shows at  $\sim 1665$  KeV, and the third coincident photopeak shows at  $\sim 2497$  KeV.

formed for the energy-calibrated spectra, and background subtracted spectra. Each de-convolution cycle starts with only the energy region containing the photopeak, and below. It proceeds by calculating destination bin of any two events residing in the single-events region, and as a metric computes the reduced S-value of the residuals between the input spectrum to the resulting de-convolution in the first-order pileup region[65]. The de-convolution spectrum is generated in the following way,

$$P_k(E_i + E_j) = \sum_{k=i+j} P_i(E_i) * P_j(E_j) \quad (6.17)$$

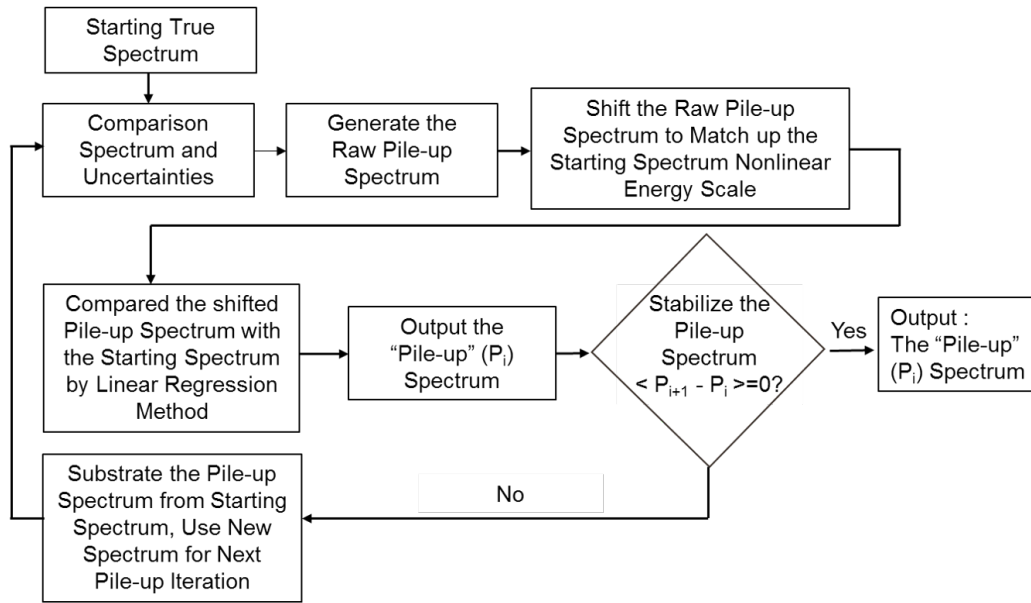


Figure 6.6. De-convolution algorithm used to determine pileup events to be removed from the  $^{54}\text{Mn}$  spectrum.

where it is assumed that the energy value refers to the bin center. Unfortunately, the energy associated with the convoluted bin  $k$  does not match the energy bins associated with the original energy spectrum because of the nonlinear calibration. The de-convolution spectrum must be appropriately energy scaled before it can be subtracted from the original energy spectrum. Thus, the energy scale of the pile-up spectrum must be corrected to match the original spectrum energy scale. Because the energy scale of the  $^{54}\text{Mn}$  spectra is non-linear, it is convenient to match up energy scales directly for this subtraction process. Again, only the pile-up spectrum is manipulated. This procedure is similar in the previous background correction process.

Once the pile-up spectrum is generated, and appropriately energy matched to the  $^{54}\text{Mn}$  spectrum, the pile-up spectrum is then compared with the 1st pile-up region input the spectrum for amplitude rescaling. The comparison region for the source, and the pileup spectrum is the energy region between the end of the primary photo-

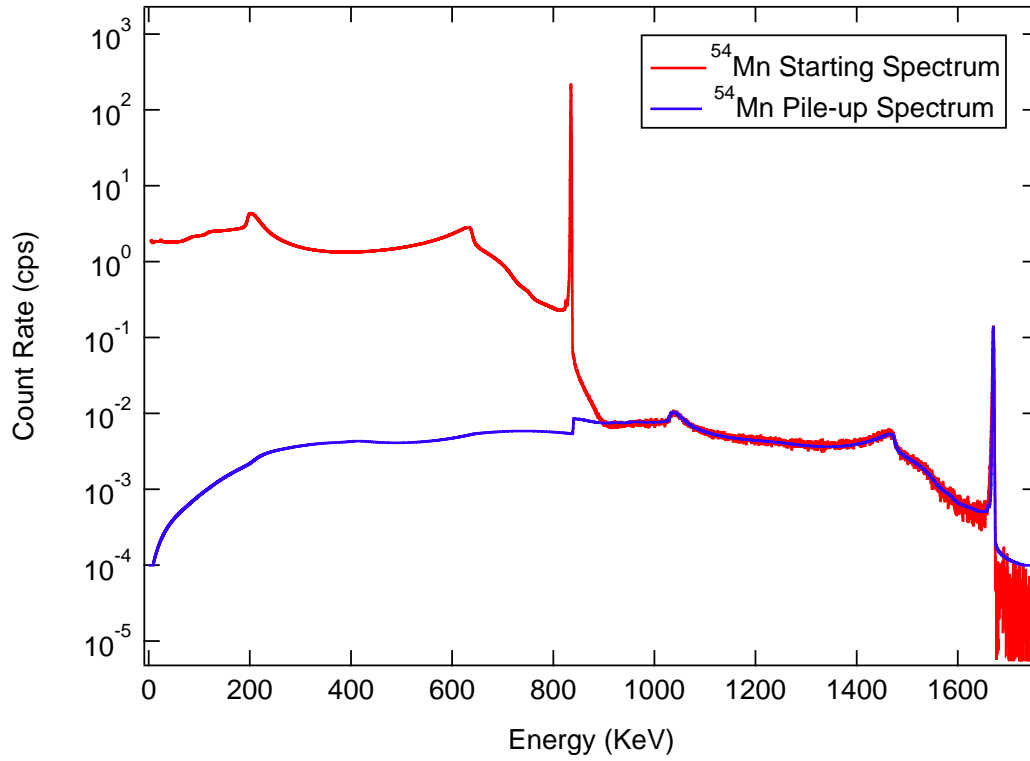


Figure 6.7. Calculated pileup spectrum (blue) with the starting spectrum (red) demonstrating the fit achieved by the de-convolution algorithm.

peak (1st), and the end of the pileup photopeak (2nd) which is within the boundaries of Region 2 to Region 4 in Figure 6.5. A linear regression method with uncertainties in 2-dimension is utilized to obtain the scaling factor[65]. After the pile-up spectrum amplitude scaling, the pileup spectrum is subtracted from the original starting energy spectrum that served as the first guess to generate the pileup spectrum. This process is then iterated until the starting spectrum, and the generated pileup spectrum stabilize. A reduced S-value test is used to stabilize the pile-up spectrum[65]. Each iteration requires reconstruction of the de-convolution or pileup spectrum to correctly compare it to, and subtract it from its generating spectrum. The de-convolution algorithm flowchart is shown in Figure 6.6. Figure 6.7 shows the starting spectrum, and

the results pile-up spectrum. As shown the method compares well in the comparison region, however, the pile-up photopeak's width is underestimated because the energy resolution is not a linear function of energy. Nonetheless, this effect does not alter the estimate of the pile-up within the region of the single event spectrum due to its smoothness in this region.

The  $\chi^2_{Dof}$  of the difference between the convolution, and the data in the match region is 1.26 indicating an acceptable convergence. Using the first day's data in which the pileup is largest, the rate difference between the convolution spectrum, and the  $^{54}\text{Mn}$  spectrum in the match region is  $\Delta R = 8 \times 10^{-6}$  cps. Again, showing an excellent match for the convolution, as the total rate in this region is  $15.176 \pm 0.014$  cps. Because the total rate difference is so much smaller than the regions total rate error, this indicates that the error generated by the convolution method is dominated by the statistics in the  $^{54}\text{Mn}$  spectrum.

The accuracy of the background match region rate is known to  $\sim 10^{-3}$ . Assuming a similar background pileup rate in the region including, and below the photopeak in the  $^{54}\text{Mn}$  spectrum means the pileup correction is at the level of  $2 \times 10^{-3}$ , given the rate in the same region of the  $^{54}\text{Mn}$  spectrum is  $\sim 8 \times 10^3$  cps. With these considerations, it is shown that the error generated by the convolution process is order  $2 \times 10^{-6}$  which can be neglected in this analysis.

After energy scaling, and convergence, the pileup spectrum is subtracted from the starting spectrum generating the true  $^{54}\text{Mn}$  pile-up corrected spectrum.

#### 6.4 Region of Interest (ROI) of $^{54}\text{Mn}$ Spectrum

The daily decay rate from the  $^{54}\text{Mn}$  corrected spectrum can be determined using two different techniques. One technique is to fit the photopeak shape. The drawback

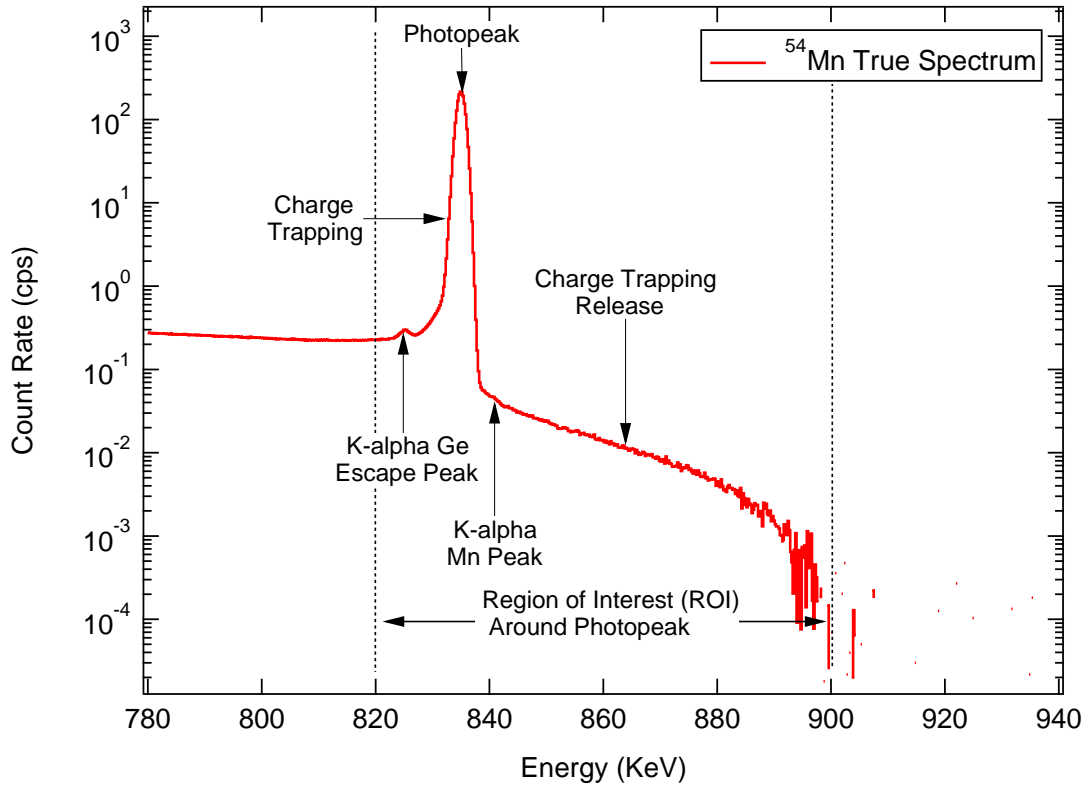


Figure 6.8. The Region of Interest, from 820 to 900 KeV, is selected from the corrected daily  $^{54}\text{Mn}$  spectrum.

of this method is the photopeak is too complicated to model to the level of accuracy required. For example, charge trapping, and charge trapping release occur in the HPGe detector during the  $\gamma$ -ray interaction process. These effects alter the HPGe line shape, as shown in Figure 6.8, and may cause reduced or excess energy to be measured in the HPGe detector that is deposited by the  $\gamma$ -ray. As is shown in Figure 6.8, the line shapes are far from having a Gaussian distribution, and no simple model can properly describe there trapping effects.

In this experiment source detector charge trapping release alters the measured  $\gamma$ -ray energy by up to 60 keV. This effect is due to the detectors previous exposure to neutrons causing defects in the crystal. Another effect due to radiation damage



is due to charge trapping on defects. In this case, the collected charge from the  $E_\gamma$  deposition is reduced. The trapping is typically 1 to 2 keV. While this detector had previously been exposed to a significant neutron flux, in evaluating the detector the only measure of merit used was a  $^{54}\text{Mn}$  Gaussian line width fit for  $\sigma_E$  measured to be very acceptable at  $\sim 1\text{keV}$ .

As it is known to degrade as a function of radiation damage,  $\sigma_E$  is the figure of merit for such damage. However, because of the very high precision required in this experiment,  $10^{-5}$ , the additional damage effects of charge trapping release were only observable after background, and pileup corrections were made to the spectra. This effect has not been reported in the literature. This effect has been studied[66], and its observation is due to the strength of the photopeak. This feature is understood as follows; Using the first days spectrum in which the effect is largest, the total rate of charge release events is 3.5 cps. This is a fractional rate of  $2 \times 10^{-3}$  when compared to the photopeak. The side band region of equal energy width below the ROI has a total rate of 0.1 cps yielding a charge release rate of  $2 \times 10^{-4}$  cps, which is not measurable in this experiment. Thus, the observation of the effect is due totally to the strength of the photopeak. For this reason, the ROI has been selected to fully include it as the upper end of the ROI energy band. Note that after the background, and pileup corrections, there are effectively zero events above the ROI energy band. In addition, the low energy band has been selected to include charge trapping as well as the k-alpha escape peak in the Ge crystal. These escape events occur when a surface Ge atom radiates a k-alpha photon away from the crystal. Thus, its energy is lost. Likewise, the k-alpha pileup from the  $^{54}\text{Mn}$  source, and the photopeak have not been removed, because these are photopeak events, while energy shifted, are not lost out of the ROI region as is shown in Figure 6.8.

By selection of the ROI band instead of what is an ill-defined, and elusive definition of photopeak, the effects of charge trapping, and charge trapping release, and

other effects do not impact the sensitivity of the measurement. Thus, the ROI in this measurement extends from 820 KeV to 900 KeV.

In addition, the ROI is a fixed energy region, instead of a fixed channel range. Selecting a fixed energy region eliminates the effects of calibration drift, and is accounted for by the time-dependent energy spectrum calibration coefficients.

### 6.5 Region of Interest(ROI) Measurement Limit Estimation

The goal of this experiment is to search for possible extensions to the weak interaction due to decay rate parameter variation caused by a flux of antineutrinos. The electronic dead time correction, the background spectrum subtraction, and pile-up spectrum correction have been used to correct each  $^{54}\text{Mn}$  daily spectrum. The error estimation of the measurement in the ROI per day includes statistical error from counting, and systematic error from instruments. Table 6.2 is the summary of the count rate, and error from each correction to the ROI per day. The total error estimation in the ROI per day for this measurement is 0.022 cps. Averaging the

Table 6.2.  
Error analysis, and estimation per day in Region of Interest (ROI) of  $^{54}\text{Mn}$  daily spectrum.

Type of Corrections per Day in ROI	Count Rate in ROI (cps)	Error Rate in ROI (cps)
Statistical (Average 20 days) with 8 periods	1431.43	1.0E-02
Dead time Poisson (0.029 sec/day)	1431.43	9.7E-03
Average ROI uncertainty (2.2E-2 KeV)	0.18	1.8E-02
Background with reactor-off	0.056	1.4E-05
Background with reactor-on	0.086	2.4E-05
Pile-up Effect from HPGe	1.70	3.4E-05
Total error <b>per day</b> estimation in rate (cps)		2.2E-02
Total error <b>per day</b> estimation in the level of		1.5E-05

daily measured decay rate in the ROI over the full length of the experiment yields on average count rate using this average a **per day** sensitive in  $\delta\lambda/\lambda \sim 1.5 \times 10^{-5}$ .



## 7. Data Analysis of Corrected $^{54}\text{Mn}$ spectral

### 7.1 Single Parameter Fitting to the Region of Interest

The  $^{54}\text{Mn}$  daily decay rate as a function of time, which is taken as the Region of Interest (ROI), is shown in Figure 7.1. The rate was calculated for each daily spectrum starting August 30, 2015, at 23:58:22, and ending March 09, 2016 at 23:12:51. The time period includes four reactor-off, and four reactor-on periods. Those daily runs which cover the transition time of the reactor-on or reactor-off period have been removed to reduce possible error. The data collection consists of a continuous period including 87 reactor-on days, and 105 reactor-off days over 192 days of data collection.

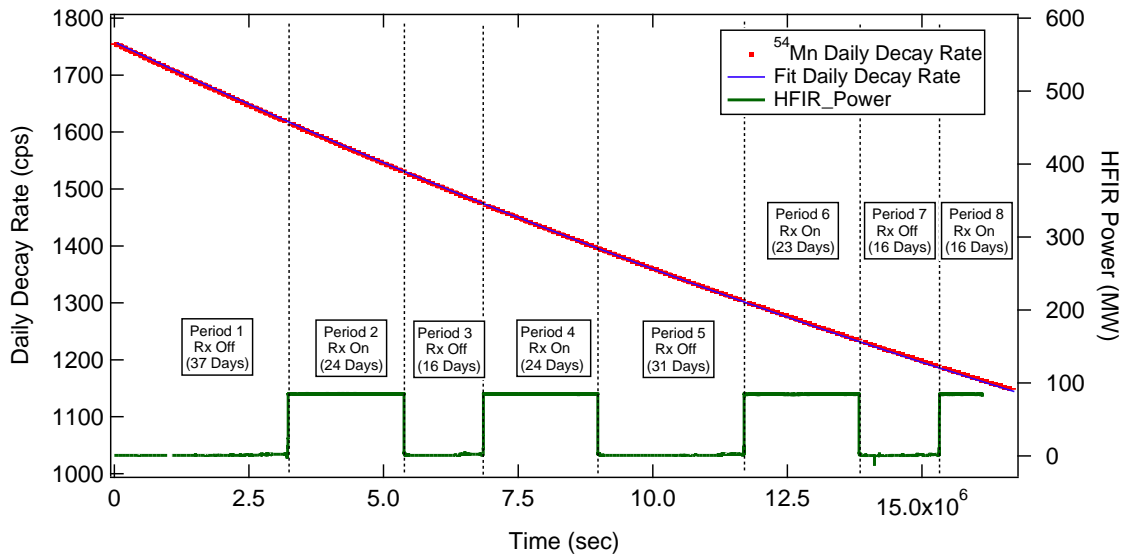


Figure 7.1. Daily decay rate from the integration between 820 to 900 KeV of the  $^{54}\text{Mn}$  spectra. Error bars are too small to be shown. The HFIR reactor power is also shown in this Figure. The Periods 1, 3, 5, and 7 are the reactor-off periods. The Periods 2, 4, 6, and 8 are reactor-on periods.

The count rate of the ROI continuing the  $^{54}\text{Mn}$  photopeak was initially  $1754.31 \pm 0.15$  cps but decayed to approximately  $1146.37 \pm 0.12$  cps at the end of the experiment. The data point for each day is plotted at the average time weighed by an exponential function calculated using the standard  $^{54}\text{Mn}$  mean lifetime  $\tau$  ( $450.41 \pm 0.29$  days)[60]. The average time is then calculated as

$$t_{ave} = \frac{\int t \exp(t/\tau) dt}{\int \exp(t/\tau) dt}, \quad (7.1)$$

integrated over the days real time period of 86,400 seconds.

Once the average time is found, and the daily rate in the ROI is obtained, the daily decay rate is then fit to an exponential decay function,

$$R(t) = ae^{-t/\tau} \quad (7.2)$$

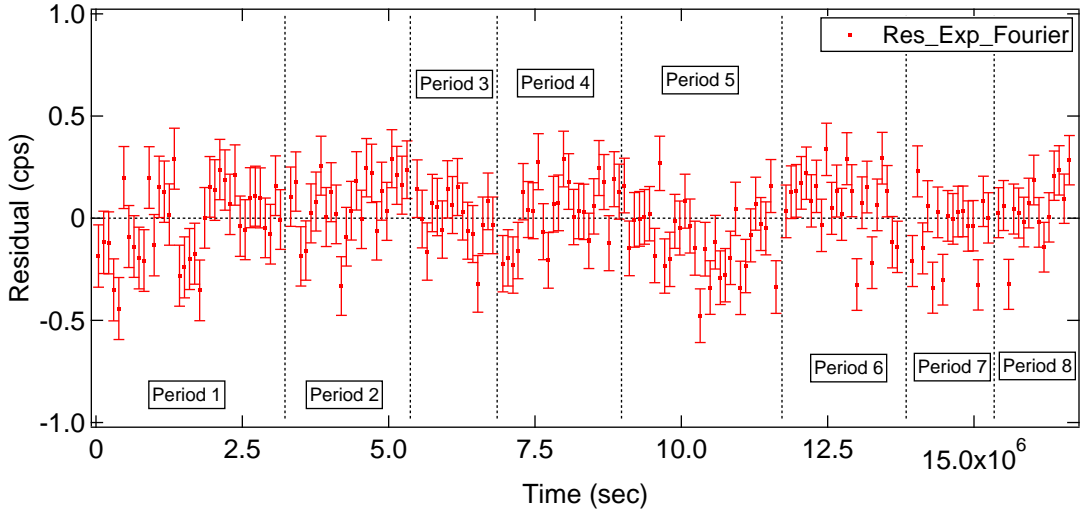


Figure 7.2. Daily residual fitted with a revised exponential decay function (Eq 7.3) which includes a single periodic function. The residuals show the oscillation significantly reduced the fit  $\chi^2$  per degree of freedom.

where  $a$  is the amplitude variable, and again  $\tau$  is fixed at the standard mean lifetime of  $^{54}\text{Mn}$ [60]. The  $\chi^2$  per degree of freedom is  $\sim 100$  which is unacceptable. The correct approach is to fit for the decay simultaneously with a revised decay function including a single periodic function with a phase to take into account the known yearly environmental oscillations already observed in the data,

$$R(t) = ae^{-t/\tau} + A\sin(\omega t + \phi). \quad (7.3)$$

Figure 7.2 shows the residuals of the revised fit(Eq. 7.3). Again,  $\tau$  is fixed at the mean lifetime of  $^{54}\text{Mn}$ [60],  $\omega$  is the periodicity fixed at one year, and  $\phi$  is the phase relative to the start of the experiment. Including the yearly environmental effects in the fit reduces the  $\chi^2$  per degree of freedom to an acceptable 1.54. As expected the oscillation has a good match to the  $b_r$  parameters oscillation, and has a good out of phase match to the humidity considering the complexity of there interactions. These are shown in Table 7.1. This is as expected if the oscillation is driven by the yearly variations in the humidity acting on the X-cooler. The amplitude of the oscillation is  $1.55 \pm 0.01$  cps. When compared to the average rate in the ROI,  $1431.43 \pm 0.18$  cps the fractional effect is at the level of  $1.1 \times 10^{-3}$ .

The revised fitting function successfully removes the oscillation behavior. The minimum value occurs on Sep/20/2015 which is nearly 21 days from the starting date Aug/30/2015. This date is not associated with the Earth's perihelion or the aphe-  
 lion which occurred Jan/02/2016 17:49 (EST), and Jul/06/2015 14:40 (EST)[67], as

Table 7.1.  
Comparison of in-phase, and out-of-phase ROI oscillation.

ROI Oscillation	Phase ( $\phi$ )	In phase factors	Phase ( $\phi$ )
In phase	$-111 \pm 0.5$ day	Linear terms $b_r$	$-122 \pm 2$ day
Out of phase	$71 \pm 0.5$ day	Humidity	$79 \pm 1$ day

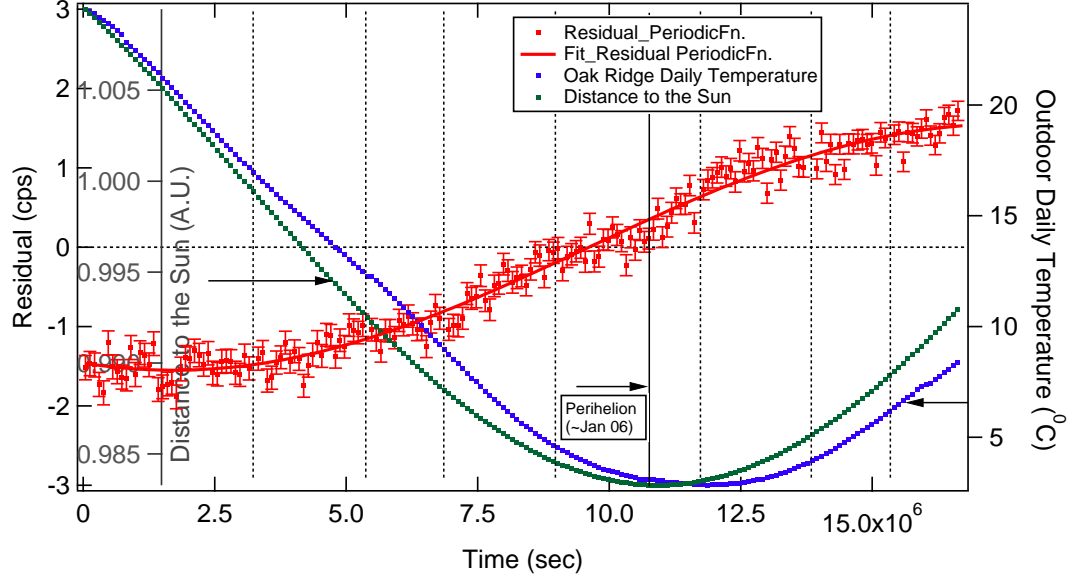


Figure 7.3. The oscillation term found by subtraction of the exponential term from the data (Eq. 7.3), and its fit shown in Red data points. For comparison, the daily outdoor temperature, and the Earth’s distance from the Sun are not in phase with the environmental oscillations in HFIR.

shown in Figure 7.3. If the periodicity is allowed to vary, the  $\chi^2/DoF$  is unchanged, and yields an oscillation of 363.6 days, in agreement within error, with the 1-year fixed value. Therefore, the oscillation of the decay rate does not correlate to the solar neutrino flux variation due to the Earth’s motion.

As an aside, The subtraction of this low-frequency term in no way affects the sensitivity of the search for decay rate parameter variations in this experiment, but instead demonstrates the ability to reject environmental effects, as the HFIR characteristic on-time period is 30 days a much higher frequency than the 1-year environmental frequency being filtered-out in this search.



## 7.2 Side Band Ambient Temperature Corrections

The DEPEC-50 spectrometer electronics are located outside the controlled environmental housing. For this reason, it is influenced by environmental factors such as temperature, pressure, and humidity. These variations are the cause of the nonlinear energy scale calibrations. The use of nonlinear calibrations has been presented in Chapter 5 for both the source, and background spectra. The nonlinear energy scale correction is given by,

$$E = a_r + b_r x + c_r x^2 \quad (7.4)$$

where  $a_r$ ,  $b_r$ , and  $c_r$  are the calibration coefficient of  $r$ th daily spectrum, and  $x$  is the channel number of the spectrum. The data is analyzed using the counts per second (cps) in a fixed energy band  $\Delta E$  which includes the photopeak. For illustration using fixed bins, this band is given by

$$\begin{aligned} \Delta E &= b_r(x_{i+n} - x_i) + c_r(x_{i+n}^2 - x_i^2) \\ &= [b_r + c_r(x_{i+n} + x_i)] \times (x_{i+n} - x_i) \end{aligned} \quad (7.5)$$

The error in the bands energy width generates an error in the counts associated with that band. The error in the width is

$$\delta(\Delta E) = [\delta b_r + \delta c_r(x_{i+n} + x_i)] \times (x_{i+n} - x_i) \quad (7.6)$$

$b_r$  is well measured to a fractional accuracy of  $7 \times 10^{-5}$ , as shown in Figure 5.7.  $c_r$  is measured only to a fractional accuracy of order  $10^{-1}$ , and requires more accurate evaluation. At low bin number the non-linear term has no effect on the energy band width. However, as the bin number increases, and in the ROI band where  $x_i \sim 4000$ , the error in the band width is dominated by the non-linear term

$$(\delta c_r \cdot 2x_i)^2 \geq (\delta b_r)^2 \quad (7.7)$$

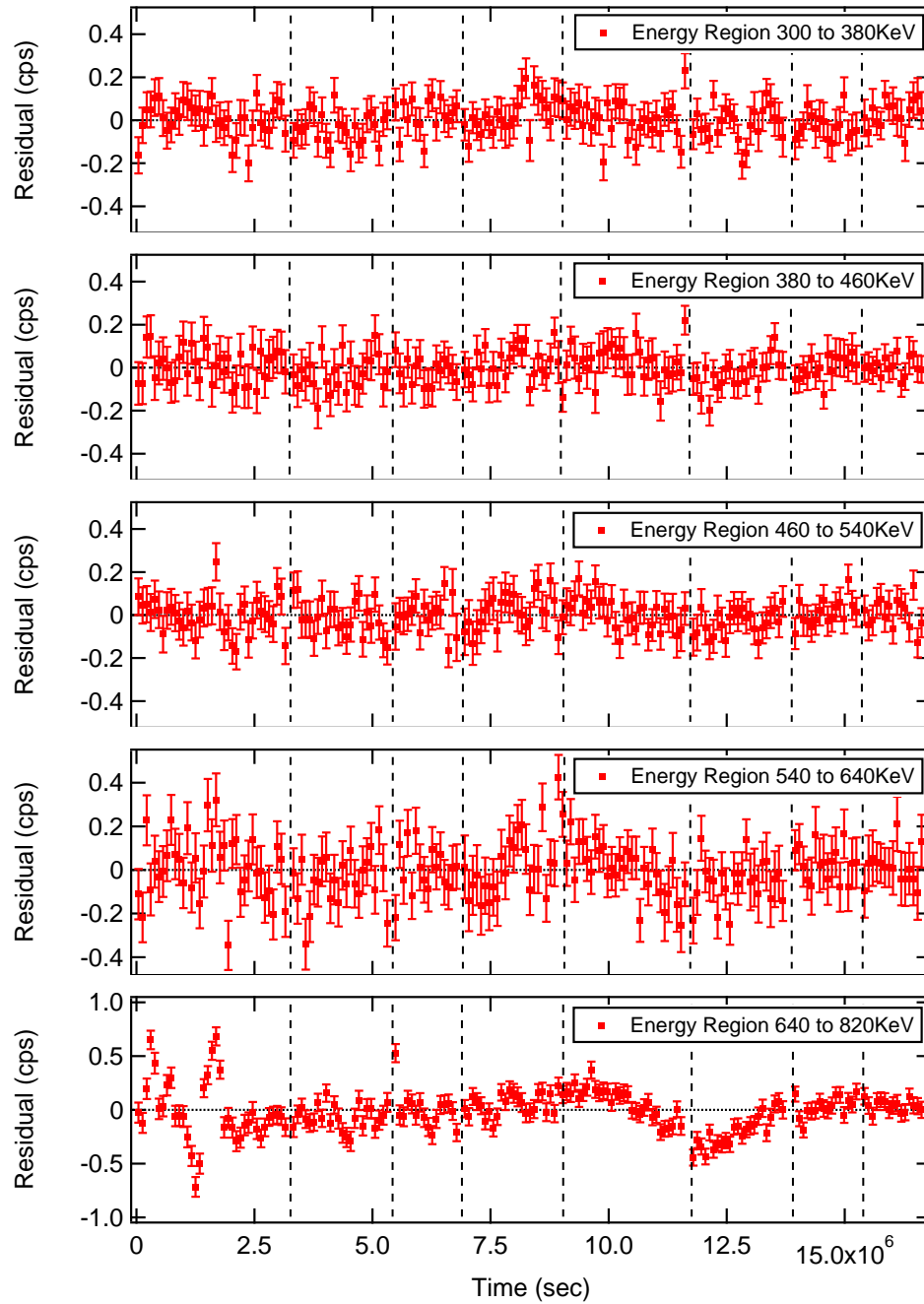


Figure 7.4. Residuals of equal width energy regions from the corrected  $^{54}\text{Mn}$  spectrum. The residuals show the environmental effects strongly correlate with the strength of the nonlinear term  $c_r x^2$ .

so that the error on the width is given approximately by

$$\delta(\Delta E) \sim \delta c_r (x_{i+n}^2 - x_i^2) \quad (7.8)$$

The knowledge of  $c_r$ -term motion as a function of the environmental parameters can be improved by study of the side band residuals. In addition, the motion of the error in the  $b_r$ -term is expected to be random as  $b_r$ 's dominant source of motion is due to the inherent linearity of the HPGe detectors temperature dependence where as the motion of the  $c_r$  term error is coming from the DSPEC-50 located outside the controlled environmental housing.

These expectations concerning  $\delta c_r$  are verified in the spectral data by study of the energy regions below the ROI. Regions of equal energy width were selected starting from 300 to 380 KeV, 380 to 460 KeV, 460 to 540 KeV, 540 to 640 KeV as well as 640 to 820 KeV all below the ROI. The daily decay rate for each of these energy regions is fit to the same function as the ROI, that is

$$R(t) = ae^{-t/\tau} + A\sin(\omega t + \phi) \quad (7.9)$$

where only  $a$ , and  $A$  are variable in this fitting.  $\omega$ ,  $\tau$ , and  $\phi$  are the same fitted coefficients found for the ROI; the fitting function from Eq. 7.3. Figure 7.4 shows the residual of these energy regions, and Table 7.2 gives the  $\chi^2$  per degree of freedom for each energy region.

As expected the  $\chi^2$  per degree of freedom for the lower energy bands is  $\sim 1$ . However, because the uncertainty in  $c_r$  has a significant effect at high bin numbers, this error is clearly observed in the side band region just below the photopeak. The  $\chi^2$  per degree of freedom is  $\sim 12$ , demonstrating a lack of knowledge in the parameter  $c_r$ .

Table 7.2.

The  $\chi^2$  per degree of freedom from fitting equal width energy regions in Figure 7.4.

Energy Region (KeV)	$\chi^2$ per degree of freedom
300 to 380	0.98
380 to 460	0.86
460 to 540	0.87
540 to 640	1.24
640 to 820	12.02

The error in  $c_r$  contributes a significant effect that increases with the channel number (energy scale). An incorrect assignment of the energy width of the ROI, as will be shown is a function in time of the environmental parameters. This correction causes events to be lost or gained as a function of the environmental changes measured through the motion of the non-linear term. The gain or loss of events due to this error is measured by the difference in the error in the energy width of the edge bins. These effects can be calculated from

$$R_L(f(E_L)) - R_U(f(E_U)) = \delta R \quad (7.10)$$

where  $f(E_L)$ , and  $f(E_U)$  are the fractional variation in the edge bins of the side band at the lower, and upper edge.  $R_L$ , and  $R_U$  are the rates in the side band edge channels of the  $^{54}\text{Mn}$  spectrum.  $\delta R$  is the residual in that energy band. The side band rate variation is caused by the poor measurement of  $c_r$ . This causes residual motion away from the fit. Because events enter or leave the band only through the edges, the knowledge of  $c_r$  can be improved by relating the correction in  $c_r$  to the residuals. Eq. 7.10 can be rewritten into

$$R_L \frac{\delta c_r(x_L^2)}{\Delta E_L} - R_U \frac{\delta c_r(x_U^2)}{\Delta E_U} = \delta R \quad (7.11)$$

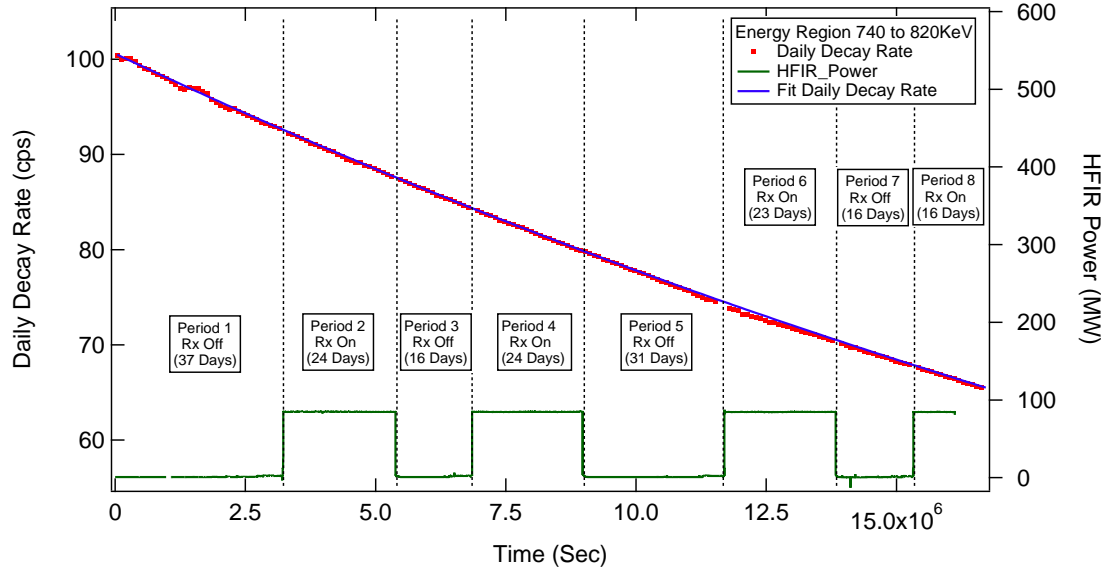


Figure 7.5. Daily Decay rate of Region 740 KeV to 820 KeV of  $^{54}\text{Mn}$  spectra

where  $\delta c_r$  is the correction to the  $c_r$  found using the side band residuals where the residuals are dominated by  $\delta c_r$ , the error in  $c_r$ . This correction provides a unique way to correct effects due to the electronic instability from the DSPEC-50.

Once the corrections are found to the non-linear calibration term using the side band, this improved knowledge is used to correct the ROI band. In order to find the correction in the ROI, the same energy width band has been selected starting from 740 KeV to 820 KeV which is the lower side band of the ROI. The upper edge of this energy region connects to the lower edge of the ROI.

Before the  $\delta c_r$  corrections can be found, an additional correction must be made to the side band. The residuals for the side band are shown in Figure 7.6. The  $\chi^2$  per degree of freedom is unacceptable  $\sim 12$ . Ambient environmental factors will be shown to correlate to these variations. These same environmental variations in the photopeak lower side band caused the fit given in Section 7.1 to fail. To correct for

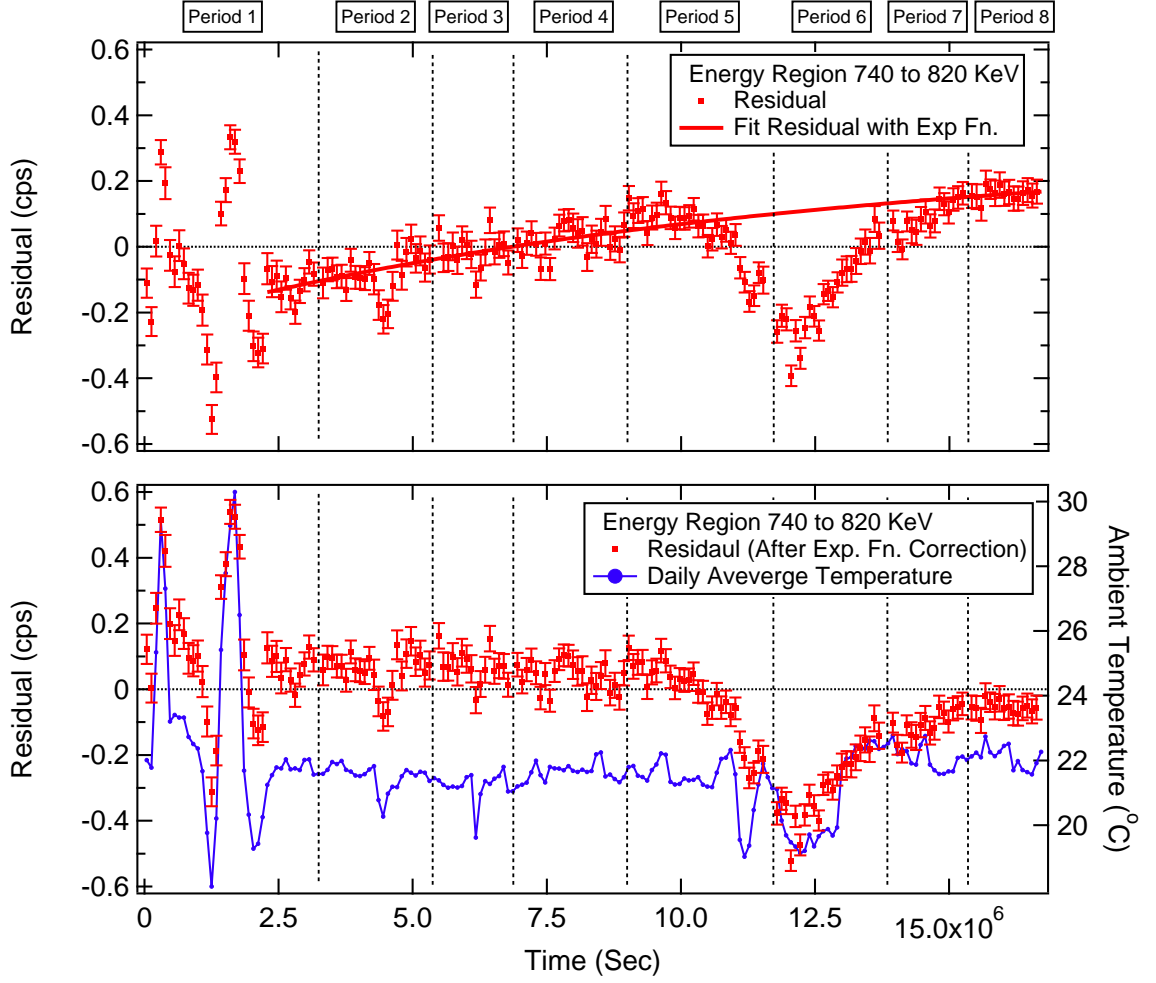


Figure 7.6. (Upper) Daily residual of the side band energy region in the  $^{54}\text{Mn}$  spectra. (Lower) Daily residual of the side band energy region of  $^{54}\text{Mn}$  spectra after the exponential function correction. A significant fluctuations appear in Period, 1, 5, and 6.

this, an additional exponential decay function, used only on this side band region, has been used to optimize the  $\chi^2$  per degree of freedom of these side band residuals found using the fit in Eq.7.9

$$\delta R(t) = C + D \times \exp(-t/\tau_1) \quad (7.12)$$

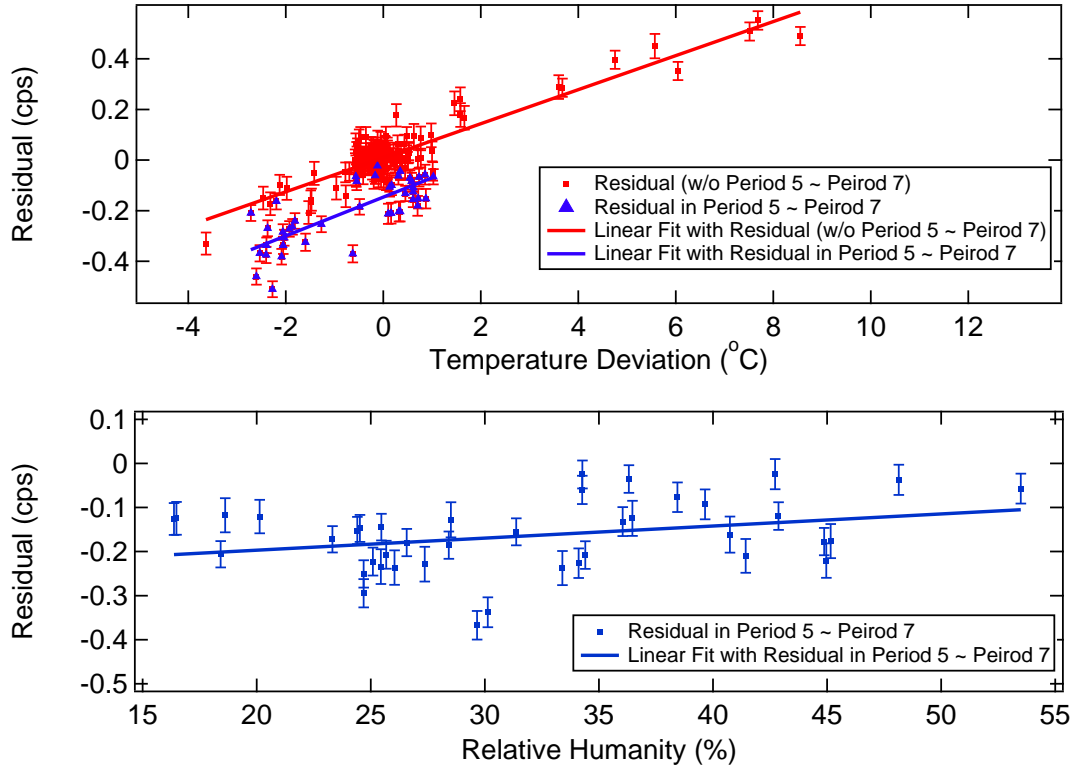


Figure 7.7. (Upper) Daily residuals of the side band energy region as a function daily average Temperature. (Lower) Daily residual in Period 5, 6, and 7 during periods with stable temperature, of the side band energy region as a function of daily relative humidity.

where  $C$ ,  $D$ , and  $\tau_1$  are the fitting coefficients of this function. Once fit the residuals in the energy region 740 to 820 KeV successfully drop the  $\chi^2$  per degree of freedom from 12 to 1.49, which is acceptable.  $\tau$  is found to be the low frequency at 139 days showing this correction is not related to reactor operations.

After correcting the lower side band residuals by Eq. 7.12, the correlation between the residuals, and the ambient temperature is clear. Figure 7.7(Upper) displays the daily residuals after exponential correction as a function of daily average temperature. The red squares in Figure 7.7 include all side band residual data points. The blue triangles only include the end of Period 5 to 7 which is related to a significant drop in

temperature. It is clear there are  $\pm 0.6$  cps variations with temperature deviations of -4 to 8 °C. Two linear fittings have been applied to the data set independently. The fitting coefficients from the red data point are different compared with the blue data points. The residual variations with temperature prove that environmental effects are causing the motion. However, the length of the time-dependent temperature variations also plays a role causing the difference between the red, and blue data points. Because the variations of blue data points include both reactor-off, and reactor-on periods, they are not caused by the reactor status. That is, antineutrino exposure is not the reason for this effect.

Likewise, the residuals motion is correlated with humidity as shown in Figure 7.7 (Lower) during a period with unstable temperature. It should be noted that the residual shifts displayed in Figure 7.6 do not coincide with reactor-on, and reactor-off cycles. Because of the strong correlation of the side band residuals with environmental factors, these residual shifts are taken as environmental, to be used to correct for environmental factors in the ROI. That is, the residuals from the lower side band, with energy width equal to the ROI region, are set to zero as a measure of the environmental factors. This pre-assumes that not measurable antineutrino effects are measurable in the side band. This is reasonable as the data rate ratios between the side band  $\sim 0.1$ cps compared to the photopeak ROI of 1800cps is  $5.6 \times 10^{-5}$ . It is assumed that any effect due to antineutrino interactions is proportional to the number of decays or this ratio.

It is noted the lower edge of the Region of Interest is the same as the upper edge of the side band edge. The upper edge of the Region of Interest is zero after the pile-up correction. After using Eq.7.11 to find  $\delta c$  from the side band, the resulting effect on the residuals in the ROI is given by

$$\delta R_{ROI} = R_U \frac{\delta c r x_{U(Side Band)}^2}{\Delta E_{U(Side Band)}} \quad (7.13)$$



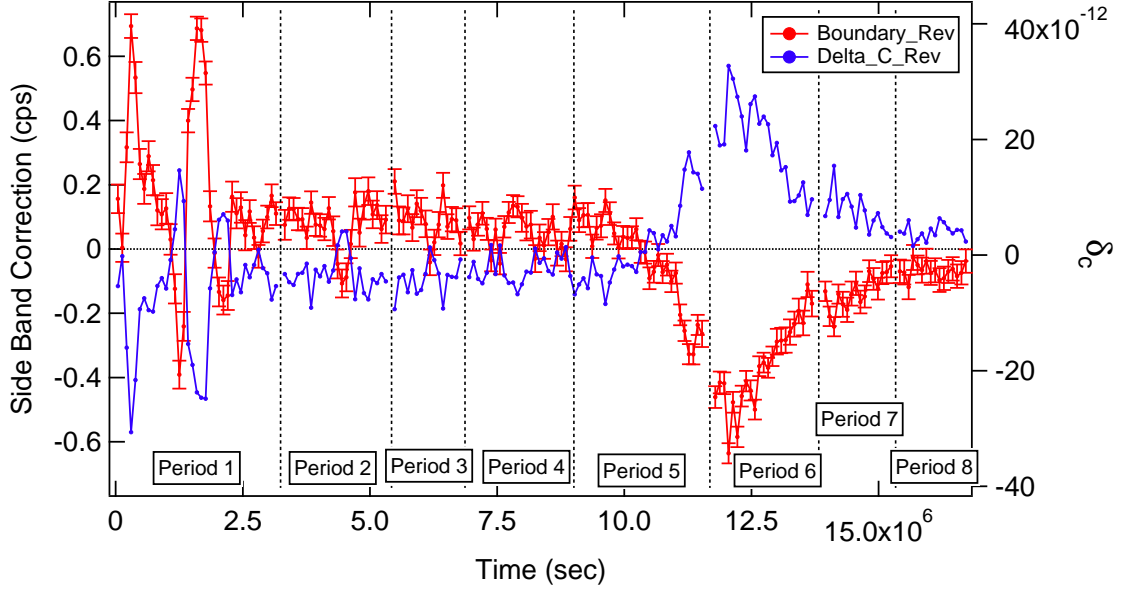


Figure 7.8. Daily  $\delta c_r$ , and corrected residual of Region 740 KeV to 820 KeV of  $^{54}\text{Mn}$  spectra, and daily average Temperature.

where  $R_{U(\text{Side Band})} = R_{L(\text{ROI})}$ , and  $x_{\text{Side band}}^2 = x_{\text{ROI}}^2$ . Note the sign changes for the correction. The rate from the upper side band edge is the lower edge of the ROI. This occurs because events lost from one band edge is a gain to the other band. The corrected daily decay rate for the ROI is then,

$$R_{\text{Corrected ROI}}(t) = R_{\text{ROI}}(t) + R_U \frac{\delta c_r(x_U^2)}{\Delta E_U} \quad (7.14)$$

### 7.3 Results After All Corrections (ROI)

The corrected daily decay rate from the  $^{54}\text{Mn}$  ROI was used to search for antineutrino interactions through decay parameter variations. The corrections made to the ROI are (1) Background Correction. (2) Pile-up Correction. (3) The exponential fit (Eq. 7.2) (4) A periodic fit with periodicity of one-year. (Eq. 7.3) (5) Side band environmental correction. Figure 7.9 shows the final residuals for the ROI as

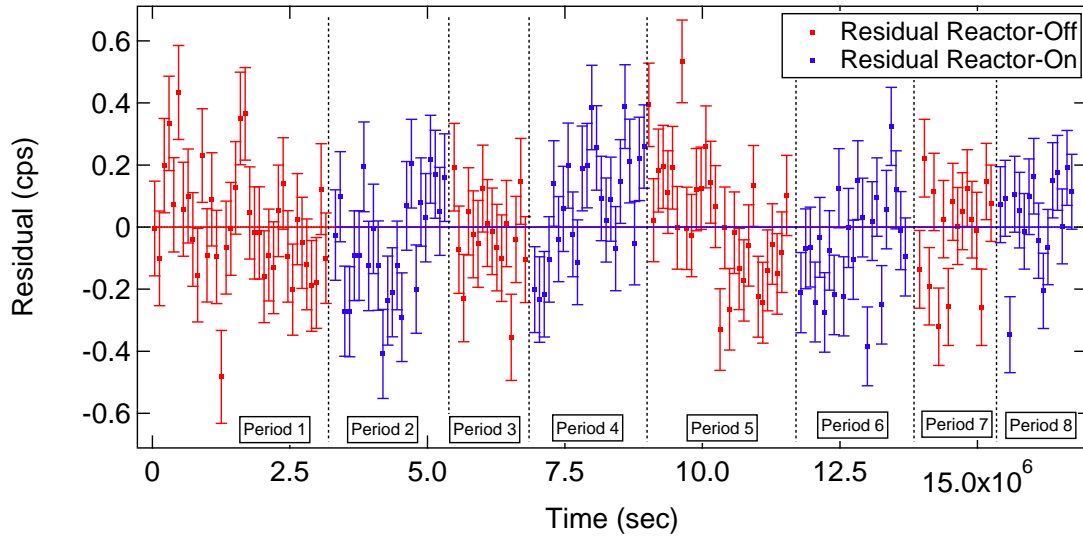


Figure 7.9. Corrected ROI Residuals as a function of time. The red data points indicate the residuals in reactor-off periods, and blue data points indicate the residuals in reactor-on periods.

a function of time, and reactor status. The red data points indicate the residuals in reactor-off periods, and blue data points indicate the residuals in reactor-on periods. Three different methods were used to search for an effect, and estimate sensitivity, including (1) A simple average of the residual form each period without regard to reactor status. (2) Segment analysis by checking 3 consecutive reactor cycles (3) Step search, by comparing all reactor-on residuals to all reactor-off residuals.

### Average Residual Analysis

The first method is to calculate the average residuals in each reactor-on period, and reactor-off period. This average analysis is to test consistency with the flatness of the residuals. Table 7.3 shows the average residual of each period yielding the size of its motion away from zero,  $\delta R(\text{cps})$ . Averaging all the periods without regard to reactor status yields  $\delta R = (0.52 \pm 1.08) \times 10^{-2} \text{cps}$ , and  $\delta R/R = (3.62 \pm 7.53) \times 10^{-6}$  where  $R$  is taken as the experimental average rate. This test shows the residuals are

Table 7.3.

Average residuals, and uncertainty of each reactor-on, and reactor-off period. The averaged results without regards to reactor status. The mean of all the data is less than 1-standard deviation. This is one test showing the data's consistency indicating no effect during the antineutrino exposure.  $R$  is taken as the experimental average rate in ROI.

Average Residual Analysis			
Period	Reactor Status	Residual (cps)	Uncertainty (cps)
1	Off	9.35E-03	3.02E-02
2	On	-5.01E-02	3.07E-02
3	Off	-3.24E-02	3.57E-02
4	On	7.52E-02	2.92E-02
5	Off	2.24E-03	2.48E-02
6	On	-5.81E-02	2.73E-02
7	Off	-1.90E-02	3.28E-02
8	On	3.41E-02	3.22E-02
Average Size of Effect in $\delta R$ (cps)		5.18E-03	1.08E-02
Average Size of Effect in $\delta R/R$		3.62E-06	7.53E-06

consistent with an origin having a single value, zero, indicating no effect during the antineutrino exposure.

### Segment Analysis

The second method is called the segment analysis. The approach to this data analysis is to use a walking window technique, taking advantage of the alternating reactor cycle pattern for the antineutrino flux. The two like reactor status periods are averaged into a single data point, and compared to the average of the opposite reactor status they guard.

Table 7.4.

Residual, and uncertainty of each reactor-on, and reactor-off period for segment analysis. The sign of the residuals in on-off-on test are flipped relative to the off-on-off test. The average size of effect is within one standard deviation.  $R$  is taken as the experimental average rate in ROI.

Segment Analysis			
Period	Reactor Status	Residual (cps)	Uncertainty (cps)
1-2-3	off-on-off	-3.86E-02	3.31E-02
2-3-4	on-off-on	4.49E-02	3.00E-02
3-4-5	off-on-off	8.02E-02	3.07E-02
4-5-6	on-off-on	-1.38E-02	2.83E-02
5-6-7	off-on-off	5.98E-02	2.91E-02
6-7-8	on-off-on	6.98E-03	2.99E-02
Average Size of Effect in $\delta R$ (cps)		2.11E-2	2.13E-2
Average Size of Effect in $\delta R/R$		1.48E-5	1.49E-5

The Periods 1-2-3 off-on-off, Periods 2-3-4 on-off-on, Periods 3-4-5 off-on-off, Periods 4-5-6 on-off-on, Periods 5-6-7 off-on-off, and Periods 6-7-8 on-off-on have been used to search for an effect. This comparison is highly correlated as each measurement is used 3 times. For this reason, the calculated residual is increased by  $\sqrt{3}$  accounting for the correlation. Table 7.4 shows the segment analysis average residual of each group of periods as well as the final size of the effect. That is  $\delta R = (2.11 \pm 2.13) \times 10^{-2}$  cps, and  $\delta R/R = (1.48 \pm 1.49) \times 10^{-5}$ . The results are within one standard deviation, and again consistent with no effect during the antineutrino exposure.

### Linear Fitting Analysis

The strongest test of the data is to combine all the reactor-on data, and compare to all the reactor-off data in search of a step. This is the method

Table 7.5.  
Size of effect, and uncertainty from a single constant term.

Linear Fitting Analysis				
Fitting Period	Reactor Status	Residual (cps)	Uncertainty (cps)	$\chi^2/DoF$
All	N/A	1.49E-05	9.89E-03	1.68
1,3,5,7	Off	2.49E-04	1.38E-02	1.63
2,4,6,8	On	-2.33E-04	1.42E-02	1.79
Size of Effect in $\delta R$ (cps)		4.83E-04	1.98E-02	
Size of Effect in $\delta R/R$		3.37E-07	1.38E-05	

## Summary

For this analysis, the nuclear decay rate parameter of  $^{54}\text{Mn}$  is found not to be effected when exposed to an antineutrino flux. These results are consistent with no measurable decay rate parameter variation due to an antineutrino flux yielding a 68% confidence level upper limit sensitivity, as shown in Table 7.6.

Table 7.6.  
68% confidence upper limit on antineutrino interaction on  $^{54}\text{Mn}$

Measured Variation	$\frac{\delta\lambda}{\lambda} \leq 1.43 \times 10^{-5}$
Cross Section Sensitivity	$\sigma \leq 1.34 \times 10^{-25} \text{ (cm}^2\text{)}$



## 8. Conclusion

The original goal of the experiment is to measure decay rate parameter variation with sensitivity at 1 part of  $10^5$  by measuring the  $\gamma$  spectra from the  $^{54}\text{Mn}$  electron capture decay. The experiment has achieved its sensitivity goal at the level of  $\delta\lambda/\lambda \sim 10^{-5}$ . Table 8.1 gives the result of the  $^{54}\text{Mn}$  decay rate variation as measured at HFIR. The result is consistent with no observed effect at the level of the measuring sensitivity of  $1.38 \times 10^{-5}$ . The 68% confidence level upper limit on the cross section is 0.13 barns, on the order of a nuclear or strong interaction cross-section.

Figure 8.1 compares the full data available in the literature as discussed in Chapter 3, and these final results. The logarithm cross-section or sensitivity as a function of logarithm mean lifetime of the decay parameter, is display for all experiments reporting both observed effects, and null observations. The reported decay modes include (1) the negative  $\beta$ -decay with time-dependent variation results (Red

Table 8.1.  
Summary of measurements at HFIR of  $^{54}\text{Mn}$  decay rate variations measurement.

Antineutrino Flux	$F_{\bar{\nu}} = 2.86 \times 10^{12} \text{ (sec}^{-1}\text{cm}^{-2}\text{)}$
Measured Variation	$\frac{\delta\lambda}{\lambda} = (0.034 \pm 1.38) \times 10^{-5}$
68% Upper Limit Confidence Level	$\frac{\delta\lambda}{\lambda} \leq 1.43 \times 10^{-5}$
Measured Cross Section Sensitivity	$\sigma = (0.097 \pm 1.24) \times 10^{-25} \text{ (cm}^2\text{)}$
68% Upper Limit Confidence Level	$\sigma \leq 1.34 \times 10^{-25} \text{ (cm}^2\text{)}$

Triangles)[1, 3, 6, 16, 18, 25–28], (2)the negative  $\beta$ -decay with "Null" variation results (Red Squares)[8, 12, 19, 29–32] (3) the positive  $\beta$ -decay with time-dependent variation results (Orange Triangles)[7] (4)the positive  $\beta$ -decay with "Null" variation results (Orange Squares)[33] (5) the electron capture  $\beta$ -decay with time-dependent variation results (Green Triangles)[21] (6) the electron capture  $\beta$ -decay with "Null" variation results (Green Squares)[8, 12, 19] (7) the  $\alpha$ -decay with time-dependent variation results (Purple Triangles)[5] (8) the  $\alpha$ -decay with "Null" variation results (Purple Squares)[12, 30, 34], are by exposing the solar neutrino. (9) The reactor antineutrino "Null" variation results [35]. (10) The HFIR  $^{54}\text{Mn}$  experiment result.

It is expected that the cross section sensitivities for neutrino, and antineutrino interactions at a fixed measuring sensitivity should follow the curve.

$$\sigma = A\tau^P \quad (8.1)$$

where  $A$ , and  $P$  are the fitting coefficients. In this comparison Figure 8.1, curve (a) is the temporal cross-section fit  $\sigma = A\tau^P$  to those experiments reporting decay rate parameter variations. Curve (b) compares experiments by cross-section only. This experiment is more sensitive than all previous experiments reporting positive decay rate parameter variations, and thus it is in disagreement with all positive result experiments on this basis. Curve (c) connects this experiment, and a solar neutrino experiment using  $^{40}\text{K}$ [19]. The connection between these two experiments maps out an exclusion zone in the temporal cross-section space excluding decay rate parameter variations at a level  $10^4$  times more sensitive than any previously reported positive result. Curve (d) displays the temporal cross exclusion zone  $\sigma \sim \sigma_{limit}\tau^{-1}$  if extrapolated using only this experiment, and again is in disagreement with all positive result experiments.

The properties of these curve are displayed in Table 8.2. From these data, a



Table 8.2.  
Coefficients from four type of curve fitting with previous experiments.

Curve	$A$	$P$
(a) Observed variation	-12.31	-1
(b) Cross section only comparison	-24.87	0
(c) Exclusion Region	-19.54	-0.71
(d) This experiment temporal exclusion	-17.28	-1

convincing case is made that those measurements reporting decay rate parameter variations are not consistent with the source of the variations being caused by neutrino or antineutrino interactions.

As displayed in Figure 8.1, isotopes with longer mean lifetime can obtain better cross-section sensitivity. Data in the same experimental configuration at HFIR using  $^{137}\text{Cs}$  a  $\beta^-$ -decay process, and  $^{108}\text{Ag}$  an electron capture decay process, having nearly 30, and 400 years mean lifetime, has been collected, and are under analysis for decay rate parameter variations.

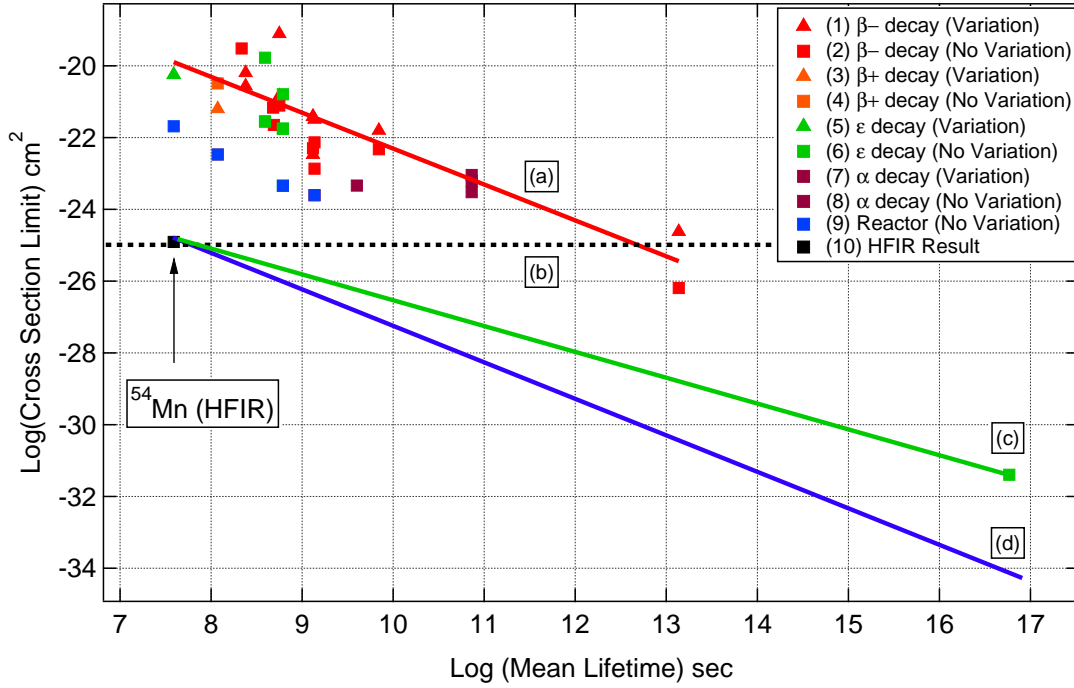


Figure 8.1. The logarithm cross section sensitivity of time-dependent variation results, no evidence results, and this HFIR result as a function of the logarithm mean lifetime. The data are based on Table 3.7, and 3.8. The data includes (1)  $\beta^-$  decay with variation results[1, 3, 6, 16, 18, 25–28], (2)  $\beta^-$  decay with no effect results[8, 12, 19, 29–32], (3)  $\beta^+$  decay with variation results[7], (4)  $\beta^+$  decay with no effect results[33], (5) Electron Capture decay with variation results[21], (6) Electron Capture decay with no effect results[8, 12, 19], (7)  $\alpha$  decay with with variation results[5], (8)  $\alpha$  decay with no effect results[12, 30, 34], and (9) reactor antineutrino as a test source with no effect results[35]. (10) The HFIR  $^{54}\text{Mn}$  experiment result. See the text for explanation of the curves (a), (b), (c), and (d).

## Bibliography

- [1] D. Alburger, G. Harbottle, and E. Norton, *Earth and Planetary Science Letters* **78**, 168 (1986).
- [2] E. Falkenberg, *Apeiron* **8**, 32 (2001), 12.
- [3] E. Falkenberg, *Apeiron* **9**, 41 (2002), 3.
- [4] J. Jenkins, E. Fischbach, D. J. II, R. Lee, and P. Sturrock, *Applied Radiation and Isotopes* **74**, 50 (2013).
- [5] J. H. Jenkins et al., *Astroparticle Physics* **32**, 42 (2009).
- [6] J. H. Jenkins et al., *Astroparticle Physics* **37**, 81 (2012).
- [7] D. O’Keefe et al., *Astrophysics and Space Science* **344**, 297 (2013).
- [8] H. Schrader, *Applied Radiation and Isotopes* **68**, 1583 (2010), *Proceedings of the 17th International Conference on Radionuclide Metrology and its Applications (ICRM 2009)*.
- [9] H. Schrader, *Applied Radiation and Isotopes* **114**, 202 (2016).
- [10] S. E. Shnoll et al., *Physics-Uspekhi* **41**, 1025 (1998).
- [11] S. E. Shnoll et al., *Physics-Uspekhi* **43**, 205 (2000).
- [12] H. Siegert, H. Schrader, and U. Schtzig, *Applied Radiation and Isotopes* **49**, 1397 (1998).
- [13] P. A. Sturrock, E. Fischbach, and J. H. Jenkins, *Solar Physics* **272**, 1 (2011).
- [14] P. Sturrock et al., *Astroparticle Physics* **42**, 62 (2013).

- [15] P. Sturrock et al., *Astroparticle Physics* **59**, 47 (2014).
- [16] P. Sturrock, A. Parkhomov, E. Fischbach, and J. Jenkins, *Astroparticle Physics* **35**, 755 (2012).
- [17] P. Sturrock, G. Steinitz, E. Fischbach, D. J. II, and J. Jenkins, *Astroparticle Physics* **36**, 18 (2012).
- [18] P. Sturrock, G. Steinitz, E. Fischbach, A. Parkhomov, and J. Scargle, *Astroparticle Physics* **84**, 8 (2016).
- [19] E. Bellotti, C. Brogini, G. D. Carlo, M. Laubenstein, and R. Menegazzo, *Physics Letters B* **720**, 116 (2013).
- [20] E. Fischbach et al., *Space Science Reviews* **145**, 285 (2009).
- [21] J. H. Jenkins and E. Fischbach, *Astroparticle Physics* **31**, 407 (2009).
- [22] D. Krause et al., *Astroparticle Physics* **36**, 51 (2012).
- [23] J. A. Formaggio and G. P. Zeller, *Rev. Mod. Phys.* **84**, 1307 (2012).
- [24] K. S. Krane, *Introductory Nuclear Physics*, John Wiley & Sons, Inc., 1988.
- [25] D. Veprev and V. Muromtsev, *Astroparticle Physics* **36**, 26 (2012).
- [26] A. G. Parkhomov, *International Journal of Pure and Applied Physics* **1**, 119 (2005).
- [27] Y. A. Baurov, Y. G. Sobolev, Y. V. Ryabov, and V. F. Kushniruk, *Physics of Atomic Nuclei* **70**, 1825 (2007).
- [28] A. Parkhomov, *Journal of Modern Physics* **2**, 1310 (2011).
- [29] G. Bruhn, *Apeiron* **9**, 28 (2002), 2.
- [30] T. Semkow et al., *Physics Letters B* **675**, 415 (2009).

- [31] K. Kossert and O. J. Nhle, *Astroparticle Physics* **55**, 33 (2014).
- [32] K. Kossert and O. J. Nhle, *Astroparticle Physics* **69**, 18 (2015).
- [33] E. B. Norman, E. Browne, H. A. Shugart, T. H. Joshi, and R. B. Firestone, *Astroparticle Physics* **31**, 135 (2009).
- [34] P. S. Cooper, *Astroparticle Physics* **31**, 267 (2009).
- [35] R. de Meijer, M. Blaauw, and F. Smit, *Applied Radiation and Isotopes* **69**, 320 (2011).
- [36] C. L. Cowan, F. Reines, F. B. Harrison, H. W. Kruse, and A. D. McGuire, *Science* **124**, 103 (1956).
- [37] F. REINES and C. L. C. JUN., *Nature* **178**, 446 (1956).
- [38] G. Danby et al., *Phys. Rev. Lett.* **9**, 36 (1962).
- [39] K. Kodama et al., *Physics Letters B* **504**, 218 (2001).
- [40] B. Pontecorvo, *Journal of Experimental and Theoretical Physics* **33**, 549 (1958).
- [41] R. Davis, D. S. Harmer, and K. C. Hoffman, *Phys. Rev. Lett.* **20**, 1205 (1968).
- [42] Y. Fukuda et al., *Phys. Rev. Lett.* **81**, 1562 (1998).
- [43] F. P. An et al., *Phys. Rev. Lett.* **108**, 171803 (2012).
- [44] J. K. Ahn et al., *Phys. Rev. Lett.* **108**, 191802 (2012).
- [45] N. Agafonova et al., *Physics Letters B* **691**, 138 (2010).
- [46] K. Abe et al., *Phys. Rev. D* **88**, 032002 (2013).
- [47] A. BELLERIVE, *International Journal of Modern Physics A* **19**, 1167 (2004).
- [48] T. D. Lee and C. N. Yang, *Phys. Rev.* **104**, 254 (1956).

- [49] C. S. Wu, E. Ambler, R. W. Hayward, D. D. Hoppes, and R. P. Hudson, *Phys. Rev.* **105**, 1413 (1957).
- [50] M. Goldhaber, L. Grodzins, and A. W. Sunyar, *Phys. Rev.* **109**, 1015 (1958).
- [51] R. N. Mohapatra and G. Senjanović, *Phys. Rev. Lett.* **44**, 912 (1980).
- [52] G. Mention et al., *Phys. Rev. D* **83**, 073006 (2011).
- [53] Y. Declais et al., *Physics Letters B* **338**, 383 (1994).
- [54] C. Athanassopoulos et al., *Phys. Rev. Lett.* **75**, 2650 (1995).
- [55] A. Aguilar et al., *Phys. Rev. D* **64**, 112007 (2001).
- [56] S. S. R.J. de Meijer, *arXiv* (2014).
- [57] High Flux Isotope Reactor, Oak Ridge National Laboratory (ORNL), <https://neutrons.ornl.gov/hfir>.
- [58] G. J. Dilorio, *Direct Physical Measurement of Mass Yields in Thermal Fission of Uranium 235*, New York: Garland, 1979.
- [59] G. Kessler, *Proliferation-Proof Uranium / Plutonium Fuel Cycles Safeguards and Non-Proliferation*, KIT Scientific Publishing, 2011.
- [60] National Nuclear Data Center (NNDC), Brookhaven National Laboratory, <http://www.nndc.bnl.gov/chart/>.
- [61] X-ray Transition Energy Database, Physical Measurement Laboratory, National Institute of Standards and Technology, <https://www.nist.gov/pml/x-ray-transition-energies-database>.
- [62] Y. Varshni, *Physica* **34**, 149 (1967).
- [63] G. E. Knoll, *Radiation Detection and Measurement*, John Wiley & Sons, Inc., 2000.

- [64] *DSPEC 50 /50A DSPEC 502/502A Standard / Advanced Digital Gamma-Ray Spectrometer Hardware Users Manual.*
- [65] D. York, N. M. Evensen, M. L. Martnez, and J. De Basabe Delgado, *American Journal of Physics* **72**, 367 (2004).
- [66] Energy calibration of hpge detector using neutrons, neutron induced ambient background and natural background, in *24th International Conference on the Application of Accelerators in Research and Industry (CAARI 2016)*, 2016.
- [67] Astronomical Applications Department, The United States Naval Observatory (USNO), <http://aa.usno.navy.mil/data/docs/EarthSeasons.php>.

VITA



## VITA

Shih-Chieh Liu was born in Taipei, Taiwan. He attended National Chung Cheng University from 2003 to 2007, graduated in 2007 with a Bachelor of Science in Physics. He then attended National Tsing Hua University from 2007 to 2009 and graduated in 2009 with a Master of Science in Physics. He pursued his research in condensed matter and X-ray physics under the direction of Professor Di-Jing Huang. He received a 2-year Advanced Light Source Scholarship from National Synchrotron Radiation Research Center from 2007 to 2009.

He came to Purdue University in the Fall of 2012 and began graduate studies in Physics. He received fully financial support, Research and Teaching Assistantships, from 2012 to 2018 as well as a summer research grant in 2017. He pursued his research in nuclear physics under the direction of Professor David S. Koltick and received the Doctor of Philosophy from Purdue University in 2018. He is now working at Intel as a PTD Module and Integration Yield Engineer in Oregon.